

Thermal Rydberg Spectroscopy and Plasma

Von der Fakultät Mathematik und Physik der
Universität Stuttgart zur Erlangung der Würde eines
Doktors der Naturwissenschaften (Dr. rer. nat.)
genehmigte Abhandlung

vorgelegt von

Daniel Tobias Weller

aus Tübingen

Hauptberichter:	Prof. Dr. Tilman Pfau
Mitberichterin:	Prof. Dr. Stefanie Barz
Prüfungsvorsitzender:	Prof. Dr. Hans Peter Büchler
Tag der mündlichen Prüfung:	29. Juli 2019

5. Physikalisches Institut der Universität Stuttgart

2019

Danksagungen

Zuerst gilt mein Dank Tilman Pfau, der mit seinem Physik-Enthusiasmus eine Denkweise vorlebt, die ansteckend ist. Am 5. Physikalisches Institut der Uni Stuttgart forschen zu dürfen ist ein Privileg, für das ich sehr dankbar bin.

Frau Prof. Stefanie Barz danke ich für die freundliche Übernahme des Mitberichts und Herrn Prof. Hans Peter Büchler für den Prüfungsvorsitz.

Danke an Robert Löw, der mit seiner Leidenschaft für das schier unermüdliche Potenzial verschiedenster Ideen begeistert und mich so spielerisch für sein Projekt gewonnen hat.

Mein ganz besonderer Dank gilt Harald Kübler, der immer pfiffige Ideen und die richtigen Lösungsansätze parat hat. Deine Unterstützung ist sehr viel wert, vielen Dank dafür!

Danke, Alban Urvoy und Jim Shaffer, für Eure wichtigen Beiträge zu unseren gemeinsamen Publikationen. Für das Korrekturlesen meiner Arbeit danke ich Ralf Ritter, Alban Urvoy, Mark Zentile und Harald Kübler.

Von meinen Kolleginnen und Kollegen am Institut ging stets ein freundschaftliches Miteinander aus, das ich sehr genossen habe. Besonders hervorheben möchte ich an dieser Stelle Ralf Ritter, Fabian Ripka und Georg Epple. Vielen Dank für die gemeinsame Zeit inner- und ausserhalb des Instituts.

Vielen Dank an Frank Schreiber, der mit viel Sachkunde die Glaszellen für die hier vorgestellten Experimente hergestellt hat.

Danke an das Verwaltungs-Team aus Astrid Buck, Karin Otter und Anne-Katrin Kriesch, für Euere Unterstützung in allerlei Bürokratie.

Besonders dankbar bin ich Katharina Frey, die mich durch alle Höhen und Tiefen meiner Promotion begleitet hat.

Den wichtigsten Anteil an allem aber haben meine Eltern. Danke, dass Ihr mich immer und überall unterstützt und für mich da seid! Danke, dass Ihr mir ermöglicht und mich anspricht, meinen Weg zu finden und zu gehen.

Contents

Zusammenfassung	1
Introduction	5
I Theoretical Concepts	9
1 Atom-light interaction	11
1.1 Quantum mechanical description	11
1.2 Density matrix formalism	12
1.3 Dissipation and inhomogeneous effects	13
1.3.1 Lindblad operator	13
1.3.2 Ensemble average	14
1.4 Rotating wave approximation	15
1.5 Transition dipole moments	16
1.6 Absorption	17
1.6.1 Beer-Lambert law	18
1.7 Excitation schemes	20
1.7.1 Two-level system	20
1.7.2 Three-level ladder system	22
1.8 Motional effects	25
1.8.1 Doppler broadening	25
1.8.2 Transit time broadening	26
1.8.3 Collisional broadening	27
2 Rydberg atoms	29
2.1 General properties	29
2.2 Stark effect	31
2.2.1 Quadratic Stark effect	31
2.2.2 Stark maps	32
2.3 Rydberg-Rydberg interactions	33
2.3.1 Dipole-dipole interaction	35
2.4 Ionization processes	37
2.4.1 Collisional ionization	37
2.4.2 Photoionization	39
2.5 Recombination	40
3 Plasmas and electric fields	41
3.1 Properties of a plasma	41
3.1.1 Debye shielding	42
3.1.2 Plasma parameter and quasi neutrality	43

3.1.3	Plasma oscillations	44
3.2	Electric field distribution	46
3.2.1	DC-Stark broadening	47
4	Optical bistability	49
4.1	Introduction	49
4.2	Mean-field formalism	50
II	Distinction between Rydberg-Rydberg Interactions and Charge Induced Bistability	53
5	Part II: Introduction	55
6	Setup and methods	57
6.1	Two-species rubidium spectroscopy	57
6.2	Cesium spectroscopy	60
7	Results and discussion	63
7.1	Two-species rubidium spectroscopy	63
7.1.1	Optical bistability	63
7.1.2	Interspecies interaction	64
7.1.3	Exclusion of Rydberg-Rydberg interactions	66
7.1.4	Ionization-induced electric fields	68
7.1.5	Quantitative analysis	69
7.1.6	Experimental cross-talk	71
7.2	Cesium spectroscopy	72
7.2.1	Manipulating the sign of the interaction	72
7.2.2	Electric field modulation	72
8	Part II: Conclusion	75
III	Characterization of the Plasma and the Bistability	77
9	Part III: Introduction	79
10	Setup and methods	81
10.1	Experimental setup	81
10.2	Fluorescence measurements	83
10.3	RF-injection and transmission measurements	84
11	Results and discussion	87
11.1	Bistability mechanism	87
11.2	Microwave-transmission and fluorescence measurements	91
11.3	Plasma properties	93

11.4	Scaling behavior of the bistability edges	95
11.4.1	Plasma transition and edge frequency	95
11.4.2	Adjusted Rabi frequency	97
11.4.3	Scaling behavior	98
11.4.4	Assessment of the scaling behavior via rate equations	100
12	Part III: Conclusion	103
IV	Numerical Modeling of the Interplay between Rydberg Atoms and the Plasma	105
13	Part IV: Introduction	107
14	Concept and methods	109
14.1	Fundamental procedure	109
14.1.1	Density matrix formalism	111
14.2	Ionization mechanisms	113
14.2.1	Fluorescence signal	114
14.2.2	Linearization of the recombination rate	114
14.3	Plasma broadening	114
14.4	Converting electric fields into Stark shifts	115
14.5	Iterative algorithm	118
14.5.1	Damping overshoots and oscillations	118
14.5.2	Numerical parameter	119
15	Results and discussion	121
15.1	Convergence and hysteresis	121
15.2	Retardation of the convergence	122
15.3	Comparison to the measured spectra	123
15.3.1	Parameter estimation by least-square optimization	124
15.3.2	Plausibility of the obtained values	126
15.4	Further discussion	128
15.4.1	Scaling behavior	128
15.4.2	Hysteresis on both sides	129
15.4.3	Quantitative assessment of the simulated system	129
16	Part IV: Conclusion	133
	Summary	135
	Conclusion and Outlook	137
	Bibliography	139

Zusammenfassung

Hoch angeregte Atome, sogenannte Rydberg-Atome, besitzen außergewöhnlich ausgeprägte Eigenschaften, wie zum Beispiel eine extreme Sensitivität gegenüber elektrischen Feldern. Aber auch die interatomare Beeinflussung, bei denen der Abstand der wechselwirkenden Rydberg-Atome sogar bis in die Größenordnung von einigen Mikrometern reichen kann, machen sie zu einem interessanten Gegenstand aktueller Forschung. Auch aus technischer Sicht bieten Rydberg-Atome eine Vielzahl von Vorzügen, da, je nach Anwendung, gewünschte Eigenschaften ganz einfach durch die Auswahl des jeweiligen Rydberg-Zustands oder durch externe Magnet- oder elektrische Felder erzielt werden können. Eine ganze Reihe kollektiver Phänomene wurde durch starke, weit reichende Wechselwirkungen zwischen Rydberg-Atomen motiviert. Ebenso existieren Vorschläge für technische Anwendungen, die auf starken Korrelationen im atomaren Dampf basieren. Wegweisende Publikationen aus dem Forschungsgebiet der Rydberg-Atome sind Quanten-Gates [1, 2], Quanten-Phasenübergänge [3, 4], optische Nichtlinearitäten mit Einzelphotonen [5–9], Mehrkörperwechselwirkungen [10], Förster-Resonanzenergietransfer [11, 12], Clusterbildung [13–15] und ultralangreichweitige Moleküle [16, 17].

In jüngerer Zeit haben Wissenschaftlerinnen und Wissenschaftler das Potenzial von Dampfzellen für sich wiederentdeckt. Es zeigte sich, dass auch die Forschung an Rydberg-Atomen in thermischen Gasen das Themenspektrum der Atomphysik bereichert. Im Vergleich zu den “Kalten Experimenten” können im thermischen Gas höhere Dichten und Systeme mit einer deutlich größeren Gesamtzahl an Atomen realisiert werden. Ganz nebenbei ist auch der technische Aufwand für die experimentelle Umsetzung entscheidend geringer, da vorbereitende Schritte wie zum Beispiel das Laserkühlen oder Verdampfungskühlen entfallen. Mit der Möglichkeit, breitbandige Anregungsschema und schnelle Zeitskalen anzuwenden, ist die heutige Forschung einen Schritt näher an der Umsetzung von neuer Technologie. Beispiele aus dem Gebiet der Rydberg-Atome sind hierfür Sensoren für elektrische Feldstärken [18, 19], oder deterministische Einzelphotonenquellen [20]. Es existieren aber auch ausgereifte Anwendungen, die auf thermischen Dampfzellen basieren, wie zum Beispiel für die Magnetometrie [21] oder mikroelektromechanisch produzierte (MEMS) Miniatur-Atomuhren [22].

Einem besonderes Thema in der Atomphysik, das hier hervorgehoben werden soll, ist der Effekt der Superradianz [23]. Hierbei handelt es sich um ein Phänomen kollektiver spontaner Emission. Die Wellenlänge bei Übergängen zwischen verschiedenen Rydberg-Zuständen übertrifft leicht die räumlichen Abstände zwischen den Atomen in einem Gas. Daher wird sich hier die Zerfalldynamik eines Ensembles von Atomen von der eines isolierten Atoms unterscheiden.

Den Effekt von Superradianz auszunutzen, könnte die Grundlage für eine Quelle für kohärente Mikrowellen-Strahlung sein. Dabei würden Frequenzbereiche abgedeckt, die bisher noch unerschlossen sind [24, 25]. Denkbar wäre auch, dass solche Quellen dabei helfen, die Vision eines auf Rydberg-Atomen basierenden *Quanten-Netzwerks* [26, 27] umzusetzen: Die Knoten des Netzwerks kommunizieren dann über Mikrowellen-Strahlung, beispielsweise über Wellenleiterstrukturen. Diese Art der Strahlung nutzbar zu machen ist daher ein erstrebenswertes Ziel in der Forschung. Die theoretischen Überlegungen hierzu begannen bereits in den Siebzigerjahren [28]. Kontrollierte Mikrowellen-Übergänge wurden aber auch experimentell bereits demonstriert [29, 30]. Mit Einzug der Ultrakalten Experimente konnte Superradianz auch in diesen Systemen nachgewiesen werden [31]. Eine kürzlich veröffentlichte Publikation, die von dem Effekt in thermischen Dampfzellen berichtet [32], kündigte den nächsten Schritt zu einer tatsächlichen Umsetzung an.

Superradianz und optische Bistabilität

Der eigentliche Schwerpunkt des eben genannten Manuskripts [32] ist jedoch ein anderes Phänomen, und zwar *intrinsische optische Bistabilität in thermischen Rydberg-Gasen*. Hierbei handelt es sich um einen Phasenübergang zwischen hoher und niedriger Dichte an Rydberg-Anregungen, die laut den Autoren des Papers durch dipolare Wechselwirkungen zwischen den Rydberg-Atomen induziert werden. Der Phasenübergang äußert sich durch das Öffnen einer Hysteresekurve im Transmissionsspektrum des Anregungsschemas mit drei Lasern. Es zeigt sich, dass das Fluoreszenzspektrum signifikant unterschiedlich ist, je nachdem, in welchem der beiden Zustände das System gerade ist: Für den Zustand mit niedriger Dichte an Rydberg-Atomen fallen die Anregungszustände unter Aussendung eines Photons – wie erwartet – hauptsächlich direkt in den niedrigsten erreichbaren Zustand zurück. Bei hoher Dichte taucht jedoch eine Vielzahl an Linien im Spektrum auf. Es scheint so, als zerfielen die Rydberg-Atome wie in einer *Kaskade* [33] über die jeweils benachbarten Zustände nach unten, wobei eine Vielzahl von Zuständen bevölkert würde. Wenn diese Zustände dann wiederum anschließend in den Grundzustand zerfallen, würde dies die Vielzahl an sichtbaren Linien im Spektrum erklären können. Das Emissionsspektrum in der Phase mit hoher Rydberg-Dichte ist also ein Hinweis auf eine superradiante Kaskade. Dies ist ein zentraler Grund, weshalb wir am 5. Physikalischen Instituts der Universität Stuttgart uns dazu entschieden haben, weiter in diese Richtung zu forschen. Der charakteristische sprunghafte Übergang zwischen den beiden Phasen, über den die Superradianz thematisch mit der optischen Bistabilität verknüpft sind, konnte zwar experimentell auch bestätigt werden, spiegelte sich jedoch nicht in den bisherigen Simulationen wieder [34].

Ionisation von Rydberg-Atomen

Die außergewöhnlichen Eigenschaften, die Rydberg-Atome so einzigartig machen, umfassen auch eine ausgeprägt hohe Wahrscheinlichkeit, das Elektron auf dem angeregten Orbital

vollständig zu verlieren [35], da die Bindungsenergie nur sehr klein ist. Besonders in thermischen Gasen passieren häufig Kollisionen mit anderen Partikeln, und dies führt zu Ionisation der Atome. Hinweise auf einen Einfluss der dadurch auftretenden elektrischen Störfelder waren bereits bekannt [36]. Später machte man sich die Ionisation zu Nutze: anstelle von den üblichen optischen Methoden [37] werden die auftretenden Ströme gemessen [38], um somit Rydberg-Anregungen indirekt nachzuweisen. Daraus entwickelte sich ein vielversprechendes Konzept zur Detektion kleinster Konzentrationen eines spezifischen Elements oder Moleküls [39, 40]. Es ist somit naheliegend zu vermuten, dass hohe Dichten an Rydberg-Anregungen zu signifikanten Dichten an geladenen Teilchen, also Ionen und Elektronen, führen könnten. Die physikalischen Grundlage, auf der die im vorherigen Abschnitt angesprochenen Phänomene der Superradianz und optischen Bistabilität basieren ist somit nicht eindeutig geklärt: zum einen könnten die weitreichenden Wechselwirkungen zwischen Rydberg-Atomen zu den beobachteten Effekten führen, zum anderen könnten aber auch geladene Teilchen und Ionisation für die Phänomene verantwortlich sein.

Diese Dissertation

Das Ziel dieser Dissertation ist es zu klären, welche der beiden konkurrierenden Hypothesen die tatsächliche Erklärung für das Auftreten der optischen Bistabilität in thermischen Rydberg-Gasen liefert. Dazu haben wir eine experimentelle Studie durchgeführt, die empfindlich für den zugrunde liegenden Mechanismus ist. Im ersten Experiment dieser Studie messen wir die elektrischen Felder, die gemeinsam mit der Bistabilität in der Dampfzelle auftreten, durch eine zweite Spektroskopie. Dafür nutzen wir aus, dass Rubidium typischerweise in zwei natürlich vorkommenden Isotopen vorliegt: in ^{85}Rb -Atomen erzeugen wir durch die Anregungslaser eine bistabile Situation, mit den ^{87}Rb -Atomen messen wir unabhängig, gleichzeitig und in demselben Volumen der Zelle die auftretenden Wechselwirkungen. Im zweiten Experiment adressieren wir verschiedene Rydberg-Zustände, die mit unterschiedlichen Vorzeichen auf elektrische Felder reagieren. Wir schließen aus den Messungen, dass in der Tat elektrische Felder, und somit Ionisation von Rydberg-Atomen, und nicht Rydberg-Rydberg-Wechselwirkungen für das Auftreten der Bistabilität verantwortlich sind.

In einer auf den Ergebnissen der ersten Studie aufbauenden Untersuchung zeigen wir anschließend, dass die ionisierten Atome und freien Elektronen ein Plasma bilden. Die Fluoreszenz, die bei der Rekombination zu neutralen Atomen emittiert wird, bietet ausserdem ein interessantes Werkzeug zur weiteren Charakterisierung des bistabilen Systems. Die gewonnenen Erkenntnisse lassen wir in ein umfassendes Simulations-Modell einfließen, welches uns erlaubt, die gemessenen Fluoreszenzspektren mit erbaulicher Übereinstimmung zu reproduzieren.

Die Ionisation von Rydberg-Atomen könnte in einer Vielzahl von Experimenten mit thermischen Dampfzellen eine wichtige Rolle spielen. Mit dieser Dissertation zeigen wir auf, dass bei der Konzeption und Umsetzung derartiger Experimente verstärkt darauf geachtet werden muss, in einem Parameter-Regime zu arbeiten, bei dem unerwünschte Ionisation zweifelsfrei ausgeschlossen werden kann. Dies gilt insbesondere für Messmethoden für Mikrowellen- und Terahertzstrahlung, die auf eine Rückführbarkeit auf SI-Basiseinheiten abzielen. Andernfalls könnten durch die auftretenden Felder die Messungen verfälscht, oder falsche physikalische Rückschlüsse gezogen werden. Mit einer wachsenden Zahl von Experimenten mit Rydberg-Atomen in thermischen Dampfzellen weltweit ist dies weiterhin ein aktuelles Thema in der Forschung.

Introduction

Rydberg atoms are highly excited atoms and well-known due to their extraordinary properties, such as a remarkable sensitivity to electric fields and strong Rydberg-Rydberg interactions which are effective up to distances in the micrometer range. What makes these atoms interesting for potential applications is the possibility to fine-tune their properties, simply by choosing different Rydberg states, or applying electric or magnetic fields. A variety of studies of collective phenomena was motivated by the strong long-range interactions between Rydberg atoms, and applications with strongly correlated atomic clouds are being proposed. Among some of the most prominent milestones in the field of Rydberg atoms ultracold systems are quantum gates [1, 2], quantum phase transitions [3, 4], optical non-linearities on the single photon level [5–9], beyond two-body interactions [10], excitation transfer [11, 12], aggregation of excitations [13–15] and ultralong-range molecules [16, 17].

More recently, when scientists have realized the potential that vapor cells can provide, the study of Rydberg atoms in thermal vapors was understood to enrich the spectrum of research topics in atomic physics. In these vapors, much larger atom numbers and higher densities compared to ultracold gases can be achieved. Besides this, hot vapor spectroscopy requires far less technical overhead, as it does not require inconvenient preparation steps such as laser and evaporative cooling. Thermal vapors also allows to work at high bandwidths and fast timescales, which brings this technology a step closer to real world applications. Examples of highly promising areas of research in the field of Rydberg physics are electric field and terahertz sensing [18, 19], and deterministic single photon sources [20]. Other applications that are already mature are magnetometry [21] or microelectromechanically engineered atomic clocks [22].

One peculiar topic in atomic physics we want to highlight here is the effect of superradiance [23], a phenomenon of collective spontaneous emission. Particularly with Rydberg states, the transition wavelength between energetically closely lying energy levels can easily exceed the inter-particle distance in an ensemble of excited atoms. As a consequence, the decay dynamics of each single atoms is altered by stimulated emission due to decay processes anywhere in the ensemble.

Exploiting superradiance is thought of as a candidate for the design of coherent microwave sources in frequency regimes which are still inaccessible for commercially available microwave radiation sources [24, 25]. It is also conceivable that in a future vision of *Rydberg based quantum networks* [26, 27], nodes of such a system *communicate* via microwave radiation, where the wavelength matches the transitions between different Rydberg states.

Being able to control and manipulate these radiation modes is therefore a desirable goal. Research in this field has been very active since the seventies [28], and first successful demonstrations of controlled microwave transitions followed soon after [29, 30]. Superradiance was also observed in systems of ultracold atoms [31], but just with the recent discovery in thermal vapor [32] another important step towards applicability has been indicated.

Superradiance and optical bistability

The main subject of reference [32] is the phenomenon of *intrinsic optical bistability in thermal Rydberg vapor*. In the often-cited manuscript, the authors describe a non-equilibrium phase transition “between states of low and high Rydberg occupancy”, which is “induced by resonant dipole-dipole interactions between Rydberg atoms”. In context with the emergence of a hysteresis in the transmission spectrum in a three-photon excitation scheme, the authors show that the fluorescence spectra from the vapor significantly differ for the bistable phases of low and high Rydberg occupancy. For low occupancy, only the direct decays of the addressed Rydberg level and its neighboring states to the lowest possible states show up in the spectrum. For high occupancy, the picture is completely different: here, a broad range of lines is visible, that can be identified as the manifold of the lower lying transitions. It appears as if the addressed Rydberg state has decayed downwards in a *cascade* [33], and thus populated the lower lying energy levels which then subsequently fluoresce. The authors of [32] conclude: “The atomic emission spectrum of the phase with high Rydberg occupancy provides evidence for a superradiant cascade”. In light of these interesting results, further research was also commenced at our institute [34]. The characteristic threshold behavior that connects the phenomenon of optical bistability to the emergence of superradiance was indeed experimentally observed, however, it could not be reproduced in simulations.

Rydberg ionization

Along with the extraordinary properties that distinguish Rydberg atoms, the probability to separate the excited electron from its ionic core is non-negligible. Especially in thermal vapors, collision events lead to ionization of Rydberg atoms [35]. Indications for the influence of electric fields in a vapor cell Rydberg experiment can already be found in reference [36]. Later on, an electrical readout measurement of the ionization current [38] has been developed into a promising method to detect very low concentrations of specific atoms or molecules [39, 40]. It is standing to reason that high densities of Rydberg atoms contribute to significant densities of charged particles, i.e., ions and electrons. The mechanism that is responsible for the emergence of bistability and superradiance as discussed in the previous paragraph has therefore been controversial: charged particles and long-range Rydberg atom interactions can, in principle, both lead to the observed behavior.

This thesis

With the research conducted in this thesis, we aim to resolve the controversy of the physics behind the observed optical bistability in thermal Rydberg vapor. We present an experimental study that is directly sensitive to the underlying mechanism that allows us to discriminate between charged particles on the one hand and dipolar Rydberg interactions on the other hand. In our first experiment, we directly measure the electric field in a bistable situation with a two-species spectroscopy, thereby exploiting the availability of the two natural abundant isotopes of rubidium. In a second experiment, we make use of the different signs of the polarizability for different angular momentum states. Both these experiments allow us to rule out Rydberg-Rydberg interactions and support our hypothesis of a charge-induced bistability.

In a second experimental study, we demonstrate that the vapor of charged particles related to the bistability shows the characteristics of a plasma. With several measurements of the fluorescence, which apparently stems from the recombination of ions and electrons, we further characterize the threshold behavior of the system. We presume that the mechanism which contributes to this plasma formation is that inelastic, ionizing collisions between Rydberg atoms and ground-state atoms create an initial concentration of charged particles in the vapor. As a secondary step, the electrons produced by the ionization of the Rydberg atoms then become an additional source for collisions with Rydberg atoms, and so the plasma is formed.

Our experiments are completed by a numerical model of the *atom-plasma-laser* system, which produces simulated fluorescence spectra that match the measured data remarkably.

Structure of the thesis

This thesis is organized as follows. The first part is dedicated to lay out the fundamental framework, on which the description and insight on physical coherencies is based. Chapter 1 covers the interaction between atoms and light, then chap. 2 discusses the specifics of Rydberg atoms. Since Rydberg atoms are easily ionized, chap. 3 details properties of a plasma. A formalized description of the bistability in the context of the thesis is given in chap. 4.

In the second part, we show that intrinsic optical bistability can also be observed in a two-photon excitation scheme and with both rubidium or cesium atoms. We demonstrate that the sign of the interaction coincides with the sign of the polarizability. Two complementary experimental setups, aimed at discerning between Rydberg-Rydberg interactions and a charge-induced optical bistability, are laid out in chap. 6, followed by a discussion of the results in chap. 7.

The third part takes up upon the new insight: Charges being present suggests that the vapor could reveal plasma properties. Chapter 10 explains the experiment that was drafted to measure the plasma frequency, and to gain further insights into the interplay between thermal Rydberg gases and plasmas. In the discussing chapter, chap. 11, our picture of the optical bistability mechanism is explained.

Based on our understanding of the bistability in thermal Rydberg vapor, we developed a numerical model that simulates the atom-light interaction in conjunction with the appearing of a plasma. The building blocks of the simulation reflect the microscopic picture of the underlying mechanisms. The algorithm is described in part IV, chap. 14, followed by the discussion of results and a comparison to the experimental measurements in chap. 15.

Finally, the thesis concludes with a summarizing discussion and implications on past and future experiments that are based on Rydberg atoms in thermal vapor cells.

Part I

Theoretical Concepts

1 Atom-light interaction

The interaction between atoms and light has been intensively studied for several decades and different ways to mathematically describe the mutual influence have emerged [41–44]. A suitable formalism is essential in order to develop a fundamental understanding of the physical processes in an atomic physics experiment. It also provides a basis for numerical studies that complement measurement data and analysis with a quantitative evaluation.

In this chapter, we present the underlying framework that is necessary to comprehend the research and numerical modeling conducted in this thesis. We rely on a semi-classical picture, in which the atom is treated quantum-mechanically, while the light field is described by classical plane waves.

1.1 Quantum mechanical description

In general, the total Hamiltonian of an interacting atom-light system consists of the atomic Hamiltonian H_a , the operator for the electromagnetic field H_l , and a term H_{int} , which encapsulates the interaction between the two. When semi-classical treatment of the atom-light interaction is sufficient, i.e., the quantum-nature of the light-field can be neglected, the Hamiltonian of the interacting system simplifies to

$$H = H_a + H_{\text{int}}. \quad (1.1)$$

The complicated electronic structure of an atom can often be represented by only a subset of its energy levels, which then are coupled by near-resonant light fields. The atomic state of an n -level system¹ in this picture is given by

$$|\Psi(t)\rangle = \sum_{i=1}^n c_i(t) |i\rangle. \quad (1.2)$$

The coefficients $c_i(t)$ determine the contribution of each energy eigenstate $|i\rangle$ to the overall state of the system for each time t . The bare atomic Hamiltonian is hence given by

$$H_a = \sum_i \hbar\omega_i |i\rangle\langle i|, \quad (1.3)$$

¹For the rest of the chapter, we omit the summation limits, implying that summation is carried out over the subset of n energy levels, with restrictions as indicated.

where the energy of the state $|i\rangle$ is given by $\hbar\omega_i$. For the interaction Hamiltonian H_{int} , we assume that within the system, each pair of states $|i\rangle \rightarrow |j\rangle$ are coupled by a plane-wave, monochromatic, near resonant light field, given by

$$\mathcal{E}_{ij} = \frac{1}{2}\mathcal{E}_{0,ij}\hat{\epsilon}_{ij}\left(e^{i\omega_{ij}t} + e^{-i\omega_{ij}t}\right). \quad (1.4)$$

Here, $\mathcal{E}_{0,ij}$ is the electric field amplitude of the electromagnetic wave, polarized in the direction of the normalized vector $\hat{\epsilon}_{ij}$. Due to the large wavelength compared to the size of the atoms, we neglect the spatial dependence of the light-field, and apply the dipole-approximation. The interaction Hamiltonian thus reads

$$H_{\text{int}} = -\mathbf{d} \cdot \mathcal{E}, \quad (1.5)$$

where \mathbf{d} is the atomic dipole operator, and \mathcal{E} is the total electric field. We can write

$$H_{\text{int}} = \sum_{i \neq j} \frac{\hbar\Omega_{ij}}{2} \left(e^{i\omega_{ij}t} + e^{-i\omega_{ij}t}\right) |i\rangle\langle j|, \quad (1.6)$$

by introducing the Rabi frequency

$$\Omega_{ij} = -\frac{\mathcal{E}_{0,ij}}{\hbar} \langle i|\mathbf{d} \cdot \hat{\epsilon}_{ij}|j\rangle \quad (1.7)$$

for the coupling between the levels $|i\rangle$ and $|j\rangle$. The strength of the coupling (cf. sec. 1.5) is determined by the electromagnetic field amplitude and the dipole matrix element

$$\mathbf{d}_{ij} = \langle i|\mathbf{d} \cdot \hat{\epsilon}_{ij}|j\rangle, \quad (1.8)$$

specific to the transition.

1.2 Density matrix formalism

A convenient way to implement the actual calculation of such atomic systems is the *density matrix* approach: The atomic state of the system is expressed in terms of a matrix

$$\rho = |\Psi\rangle\langle\Psi|, \quad (1.9)$$

with the following properties. The population of the states, $|i\rangle$, are given by the diagonal elements ρ_{ii} , while the off-diagonal entries, ρ_{ij} , represent the coherences between states $|i\rangle$ and $|j\rangle$. The density matrix is Hermitian, $\rho^\dagger = \rho$, and since the overall population is conserved and normalized, $\text{Tr}\rho = 1$. Overall, an n -level system is represented by

$n(n+1)/2 - 1$ independent components: $n(n-1)$ complex coherence values and $n-1$ real valued populations.

In comparison to the state representation, eq. (1.2), using the density matrix formalism allows us to include dissipative processes, such as spontaneous decay and dephasing. Also, ensembles of atoms can be properly described, e.g., when modeling the thermal distribution of atoms with different velocities, as an ensemble average of several density matrices.

The time evolution of the density matrix (this can be directly derived from Schrödinger's equation [45]) is given by the master equation

$$\frac{\partial \rho}{\partial t} = -\frac{i}{\hbar}[H, \rho] + L(\rho), \quad (1.10)$$

known as Liouville-von Neumann equation. The details of the additional Lindblad operator $L(\rho)$ that accounts for dissipation in the system are discussed in the next section.

1.3 Dissipation and inhomogeneous effects

In an actual experimental scenario effects that perturb the coherent evolution of an atom can never be fully avoided. At the very least, coupling to vacuum fluctuations contributes significantly to the decoherence, in terms of the natural life time of an excited state. Thus, the oscillatory motion of the atomic system gets damped and the resonance linewidth is broadened.

We distinguish between homogeneous and inhomogeneous effects. Homogeneous effects act equally on all atoms of an ensemble, and can be described by a Lindblad operator as follows in this section. In the inhomogeneous case, different atoms of an ensemble are affected differently, e.g., the Doppler effect leads to different detunings within a velocity distribution. In sec. 1.8, we introduce homogeneous and inhomogeneous broadening mechanisms that originate from the atomic motion in the vapor.

1.3.1 Lindblad operator

Homogeneous dissipative processes can be classified as one of two groups. On the one hand, in *decay* processes, population is being transferred from one state to another in a non-energy-conserving manner; the energy is *lost* from the atomic system, e.g., due to radiated photons or transformed into kinetic energy in a collision. On the other hand, *dephasing* mechanisms are energy conserving, but de-synchronize the atomic phase with the driving light field.

We can write the Lindblad operator as the sum of decay and dephasing processes,

$$L(\rho) = L_{\text{decay}}(\rho) + L_{\text{deph}}(\rho). \quad (1.11)$$

The decay hereby contributes as

$$L_{\text{decay}}(\rho) = \sum_{i,j} \Gamma_{ij} \left(C_{ij} \rho C_{ij}^\dagger - \frac{1}{2} (C_{ij}^\dagger C_{ij} \rho + \rho C_{ij}^\dagger C_{ij}) \right), \quad (1.12)$$

where $C_{ij} = |j\rangle\langle i|$ is the transition operator. The decay from state $|i\rangle$ to $|j\rangle$ is given by the rate Γ_{ij} . Alternatively, we can rewrite eq. (1.12) into

$$L_{\text{decay}}(\rho) = \sum_{i,j} (\Gamma_{ji} \rho_{jj} - \Gamma_{ij} \rho_{ii}) |i\rangle\langle i| \quad (1.13)$$

$$- \frac{1}{2} \sum_{i \neq j} \left(\sum_k \Gamma_{ik} + \Gamma_{jk} \right) \rho_{ij} |i\rangle\langle j|. \quad (1.14)$$

In this form, the first sum describes the change of diagonal entries in the density matrix, while the second term accounts for the loss of coherences due to that change (increase as well as decrease) of population.

The dephasing operator is given by

$$L_{\text{deph}}(\rho) = -\frac{1}{2} \sum_{i \neq j} \gamma_{ij} C_{ii} \rho C_{jj} \quad (1.15)$$

$$= -\frac{1}{2} \sum_{i \neq j} \gamma_{ij} \rho_{ij} |i\rangle\langle j|, \quad (1.16)$$

with dephasing rates $\gamma_{ij} = \gamma_{ji}$ of the coherence between the states $|i\rangle$ and $|j\rangle$.

1.3.2 Ensemble average

Inhomogeneous effects are processes that make the interaction with light distinguishable for different atoms in an ensemble. In contrast to the homogeneous case, the underlying processes here depend on the individual atomic characteristics (e.g., position, velocity, distance to neighboring atoms) but do not cause intrinsic decoherence on the single atom level. The observable properties of the whole atomic ensemble is determined by the joined contribution of each individual atom. Due to the probabilistic distribution of the corresponding parameter, this can cause an effective decoherence in the ensemble average.

Let X be the parameter of interest, following the normalized probability distribution $p(X)$. The density matrix $\rho(t, X)$ is determined by solving the master equation, eq. (1.10), independently for each value of X . The ensemble average is then calculated from

$$\rho(t) = \int dX \rho(t, X) p(X). \quad (1.17)$$

1.4 Rotating wave approximation

The connection between the Hamiltonian and the laser field, eq. (1.6), leads to fast oscillating terms in the master equation, eq. (1.10). Typically, the time scales of these oscillations are much shorter than the actual relevant time evolution of the atomic system. It is convenient to eliminate the fast rotating terms in the master equation, by transforming the system to an alternative reference frame, that oscillates with a frequency depending on the light fields. We define the unitary transformation operator

$$U = \sum_i e^{i\eta_i t} |i\rangle\langle i|, \quad (1.18)$$

which transforms each energy level individually. We assume that each energy level of the atomic system is reached by a specific excitation path, starting from the ground state. The reference frames then oscillates with a combined frequency η_i of the photons involved to reach each level $|i\rangle$. For ladder schemes, as relevant to this thesis, we can simplify the general expression for η_i to

$$\eta_i = \sum_{j < i} \omega_{ij}. \quad (1.19)$$

Under these definitions, the density matrix is transformed according to

$$\tilde{\rho} = U^\dagger \rho U, \quad (1.20)$$

and the new Hamiltonian becomes

$$\tilde{H}' = U^\dagger H U - i\hbar U^\dagger \frac{\partial U}{\partial t}. \quad (1.21)$$

The components of the interaction Hamiltonian in the rotating frame are thus given by

$$\left(U^\dagger H_{\text{int}} U \right)_{ij} = -\frac{\mathbf{d} \cdot \hat{\epsilon}_{ij}}{2} \mathcal{E}_{0,ij} \left(1 + e^{-2i\omega_{ij}t} \right), \quad (1.22)$$

The terms oscillating at twice the frequency of the light fields can now be neglected, as they average to zero on the timescale relevant to the coherent dynamics. In this *rotating wave approximation*, the Hamiltonian is finally given by

$$\tilde{H}_{\text{int}} = \sum_{i \neq j} \frac{\hbar \Omega_{ij}}{2} |i\rangle\langle j|. \quad (1.23)$$

The Liouville-von Neumann equation is also valid in the rotating frame approximation; the Lindblad operator $L(\rho)$ simply needs to be replaced by $L(\tilde{\rho})$. Typically, the energy scale is offset to the ground state energy. The atomic Hamiltonian, eq. (1.3), becomes

$$\tilde{H}_{\text{a}} = \sum_{i>1} \Delta_{1i} |i\rangle\langle i|. \quad (1.24)$$

1.5 Transition dipole moments

The Rabi frequency Ω , as introduced in eq. (1.7), quantifies the laser induced coupling between two specific states of an n -level system. In reality, the atomic levels are degenerate, and comprise, at least, of the magnetic sub-levels, m_{F} . In case of the Rydberg energy levels, already the hyperfine structure due to the total angular momentum F is not resolved anymore. Depending on the polarization q of the light field, the coupling to the different sub-levels is different, which reflects in

$$\Omega_{ij} = -\frac{\mathcal{E}_{0,ij}}{\hbar} \langle F, m_{\text{F}} | \mathbf{d} \cdot \hat{\mathbf{e}}_{ij} | F', m'_{\text{F}} \rangle. \quad (1.25)$$

Usually, the middle term $\mathbf{d} \cdot \hat{\mathbf{e}}_{ij}$ is expressed in the components r_q of \mathbf{r} in the spherical basis. This results in $\mathbf{d} \cdot \hat{\mathbf{e}}_{ij} = er_q \equiv d_q$, where $q = 0, \pm 1$ for π and σ^{\mp} polarized light, respectively. The Wigner-Eckart theorem allows Ω_{ij} to be factored into an angular part containing a Wigner 3-j symbol, and an angular independent term, which is the reduced dipole matrix element [46]

$$\langle F, m_{\text{F}} | d_q | F', m'_{\text{F}} \rangle = \langle F | e\mathbf{r} | F' \rangle (-1)^{F'-1+m_{\text{F}}} \sqrt{2F+1} \begin{pmatrix} F' & 1 & F \\ m'_{\text{F}} & q & -m_{\text{F}} \end{pmatrix}. \quad (1.26)$$

The matrix element in this equation further reduces according to

$$\langle F | e\mathbf{r} | F' \rangle = \langle J | e\mathbf{r} | J' \rangle (-1)^{F'+J+1+I} \sqrt{(2F'+1)(2J+1)} \begin{Bmatrix} J & J' & 1 \\ F' & F & I \end{Bmatrix}, \quad (1.27)$$

with the Wigner 6-j symbol and the nuclear spin I .

Modeling multi-level atomic structures in a simplified two-level or three-level picture makes compromises at some points inevitable. Although the hyperfine splitting of the cesium and rubidium ground states would, in principle, be large enough to lift the F degeneracy, we strictly calculate Rabi frequencies for all transitions in the $|J, m_J\rangle$ -basis. Because all beams are linearly polarized and propagate parallel to each other, we define the quantization axis such that $q = 0$. As a consequence, only transitions with $\Delta_m = 0$ are dipole-allowed. Since the ground-state is an S-state with $m_J = \pm 1/2$, this implies that only the Rydberg states with $m'_J = \pm 1/2$ are directly addressed—except when electric fields are present, and dipole selection rules are suspended due to admixture of different states.

The electric field amplitude \mathcal{E}_{\max} is determined by converting the total power P of a laser with a waist w into the maximum intensity

$$I_{\max} = \frac{2P}{\pi w^2} \quad (1.28)$$

at the center of the beam. The Rabi frequency is then calculated with

$$\mathcal{E}_{\max} = \sqrt{\frac{2I_{\max}}{c\epsilon_0}}. \quad (1.29)$$

Following this convention, the Rabi frequencies can conveniently be calculated using the software provided in [47]. The input parameters for the command `getRabiFrequency` are the states in question, beam diameter, and laser power; the return value is the peak Rabi frequency in the $|J, m_J\rangle$ -basis, for the transition from $|J_1, m_{J1}\rangle$ to $|J_2, m_{J2}\rangle$:

$$\Omega = \frac{|\mathcal{E}|}{\hbar} \cdot d_0 (-1)^{J_1 - m_{J1}} \begin{pmatrix} J_1 & 1 & J_2 \\ m_{J1} & -q & m_{J2} \end{pmatrix}, \quad (1.30)$$

with the reduced dipole matrix element

$$d_0 = \langle J_1 | \mathbf{r} \cdot \hat{\mathbf{e}} | J_2 \rangle. \quad (1.31)$$

1.6 Absorption

The propagation of light through a medium is described by Maxwell's equations. For atomic vapors, the Liouville-von Neumann equation supplements the set of equations describing the propagation of electromagnetic waves with the atomic response. The link between the classical wave equation [44],

$$\left(\frac{\partial^2}{\partial z^2} - \frac{1}{c^2} \frac{\partial^2}{\partial t^2} \right) \mathcal{E}_{ij}(z, t) = \frac{1}{\epsilon_0 c^2} \frac{\partial^2}{\partial t^2} \mathbf{P}_{ij}(z, t), \quad (1.32)$$

and the quantized description of the atomic medium through which it propagates, proceeds via the polarization:

$$\mathbf{P} = \mathcal{N} \langle d \rangle = \mathcal{N} \text{Tr} \rho (\mathbf{d} \cdot \hat{\epsilon}_{ij}). \quad (1.33)$$

The dipole, as a quantity used in both classical and quantum mechanics allows us to calculate the response of the atoms in both cases. On the one hand, the polarization P is given by the mean dipole density $\langle d \rangle$, in a medium of (atomic) density \mathcal{N} . On the other hand, in the operator based formalism, the corresponding value is obtained by tracing the density matrix times the dipole matrix element. Evaluating the latter, again in the rotating frame, yields

$$\begin{aligned} \text{Tr} \rho (\mathbf{d} \cdot \hat{\epsilon}_{ij}) &= \rho_{ij} d_{ji} + \rho_{ji} d_{ij} \\ &= \tilde{\rho}_{ij} d_{ji} e^{i(\omega_{ij} t - k_{ij} z)} + \tilde{\rho}_{ji} d_{ij} e^{-i(\omega_{ij} t - k_{ij} z)}. \end{aligned} \quad (1.34)$$

The oscillating nature of the polarization justifies the ansatz of a plane wave,

$$\mathbf{P}_{ij}(z, t) = \frac{1}{2} \left(\mathbf{P}_{0,ij}(z, t) e^{i(\omega_{ij} t - k_{ij} z)} + \mathbf{P}_{0,ij}^*(z, t) e^{-i(\omega_{ij} t - k_{ij} z)} \right). \quad (1.35)$$

which is substituted into eq. (1.33). It appears beneficial to recast into a co-moving reference frame (ζ, τ) , defined as $\zeta = z$ and $\tau = t - z/c$. Applying the *slowly varying envelope approximation* (i.e., the envelopes of the electric field, $\mathcal{E}_{0,ij}(\zeta, \tau)$, and the polarization, $\mathbf{P}_{0,ij}(\zeta, \tau)$, vary slowly with respect to the oscillating terms) reduces the second order differential equation, eq. (1.33), to a first order equation:

$$\frac{\partial}{\partial \zeta} \mathcal{E}_{0,ij}(\zeta, \tau) = -\frac{i\omega_{ij}}{2\epsilon_0 c} \mathbf{P}_{0,ij}(\zeta, \tau). \quad (1.36)$$

Summarizing eqs. (1.34), (1.35) and (1.36) yields the relation between electric field and density matrix

$$\frac{\partial}{\partial \zeta} \mathcal{E}_{0,ij}(\zeta, \tau) = i \frac{\omega_{ij} \mathcal{N} d_{ij}}{\epsilon_0 c} \tilde{\rho}_{ij}(\zeta, \tau). \quad (1.37)$$

The interplay between Rabi frequency and density matrix therefore follows

$$\frac{\partial}{\partial \zeta} \Omega_{ij}(\zeta, \tau) = i \frac{\omega_{ij} \mathcal{N} |d_{ij}|^2}{\epsilon_0 \hbar c} \tilde{\rho}_{ij}(\zeta, \tau). \quad (1.38)$$

1.6.1 Beer-Lambert law

The experimentally accessible quantity of a laser beam traveling through an ensemble of atoms is the intensity,

$$I_{ij} = \frac{\epsilon_0 c}{2} \mathcal{E}_{ij} \mathcal{E}_{ij}^*, \quad (1.39)$$

for which according to eq. (1.38) holds

$$\frac{\partial}{\partial \zeta} I_{ij}(\zeta, \tau) = -\mathcal{N} \hbar \omega_{ij} \operatorname{Im}(\Omega_{ij}(\zeta, \tau)^* \tilde{\rho}_{ij}(\zeta, \tau)). \quad (1.40)$$

For the special case of a weak light field and steady state conditions (i.e., $\Omega_{ij} \ll \Gamma_{ij}$, $\Omega_{ij}(\zeta, \tau) = \Omega_{ij}(\zeta) \in \mathbb{R}$), we can derive an analytic solution for the absorption. The coherence in this case is proportional to the Rabi frequency [48],

$$\tilde{\rho}_{ij} \propto \Omega_{ij}, \quad (1.41)$$

and therefore eq. (1.40) becomes

$$\begin{aligned} \frac{\partial}{\partial \zeta} I_{ij}(\zeta) &\propto -|\Omega_{ij}(\zeta)|^2 \operatorname{Im} \left(\frac{\tilde{\rho}_{ij}(\zeta)}{\Omega_{ij}(\zeta)} \right), \\ &= -\alpha I_{ij}(\zeta) \end{aligned} \quad (1.42)$$

introducing the absorption coefficient, α , which is characteristic of the atomic system with respect to the addressed transition. It is noteworthy that $\alpha \propto \operatorname{Im}(\rho_{ij}(t))$, meaning that the change in intensity, the *amount of absorption* is reflected in the (imaginary part) of the coherence $\tilde{\rho}_{ij}$. The integration of eq. (1.42) along the path of length l gives the well-known Beer-Lambert formula

$$I(l) = I(0)e^{-\alpha l}. \quad (1.43)$$

1.7 Excitation schemes

1.7.1 Two-level system

As an illustration of the rotating wave approximation, and as a basis for further concepts discussed in this thesis, we want to consider the simplified case of a two-level system which is exposed to a single, near resonant laser field. The ground state, $|1\rangle$, and the excited state, $|2\rangle$, are separated in energy by $\hbar\omega_2$. Given the laser frequency, ω_{12} , we can write the Hamiltonian of the system as

$$H = H_a + H_{\text{int}} = \hbar\omega_2 |2\rangle\langle 2| + \frac{\hbar\Omega_{12}}{2} (e^{i\omega_{12}t} + e^{-i\omega_{12}t}) (|2\rangle\langle 1| + |1\rangle\langle 2|). \quad (1.44)$$

Here, the Rabi frequency is assumed to be real, and the energy of the ground state is offset to zero. By transforming into the rotating frame according to eq. (1.22), we obtain

$$\tilde{H}' = \hbar(\omega_2 - \omega_{12}) |2\rangle\langle 2| + \frac{\hbar\Omega_{12}}{2} [(1 + e^{-2i\omega_{12}t}) |1\rangle\langle 2| + (1 + e^{+2i\omega_{12}t}) |2\rangle\langle 1|]. \quad (1.45)$$

The terms oscillating with $\pm 2\omega_{21}$ are now neglected according to the rotating wave approximation. For convenience, we define the laser detuning with respect to the atomic level(s) as

$$\Delta_{ij} = \omega_{ij} - \omega_j. \quad (1.46)$$

We obtain the two-level Hamiltonian

$$\tilde{H} = -\hbar\Delta_{12} |2\rangle\langle 2| + \frac{\hbar\Omega_{21}}{2} (|2\rangle\langle 1| + |1\rangle\langle 2|). \quad (1.47)$$

The Lindblad operator is given accordingly by

$$L(\tilde{\rho}) = \Gamma_{21}\tilde{\rho}_{22} (|1\rangle\langle 1| - |2\rangle\langle 2|) - \frac{\Gamma_{21} + \gamma_{21}}{2} (|2\rangle\langle 1| + |1\rangle\langle 2|), \quad (1.48)$$

for a decay rate of the excited state $|2\rangle$ of Γ_{21} and a dephasing rate γ_{21} .

Steady state solution

The time evolution of the two-level system—as well as in principle any arbitrary level configuration—can be calculated by integrating the set of coupled equations that originate

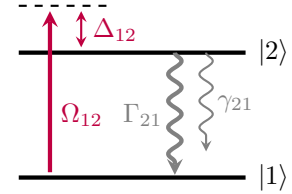


Figure 1.1: Diagram of the two-level system.

from the Liouville-von Neumann equation, eq. (1.10). For the two-level system, we require only two defining equations,

$$\frac{\partial}{\partial t} \tilde{\rho}_{12} = \left(-\frac{\Gamma_{21} + \gamma_{21}}{2} - i\Delta_{12} \right) \tilde{\rho}_{12} - \frac{i}{2} (\tilde{\rho}_{22} - \tilde{\rho}_{11}) \Omega_{12}, \quad (1.49)$$

$$\frac{\partial}{\partial t} \tilde{\rho}_{22} = \text{Im}(\tilde{\rho}_{12} \Omega_{12}^*) - \Gamma_{21} \tilde{\rho}_{22}. \quad (1.50)$$

The evolution of this system is well known from introductory textbooks. In the context of this thesis, it is noteworthy that, due to the dissipation, the oscillations between state $|1\rangle$ and $|2\rangle$ are damped out, and the system eventually reaches an equilibrium state. In many continuous-wave laser experiments, the actual atomic dynamics are of less interest, but only the steady state solution to the Liouville-von Neumann equation,

$$0 \stackrel{!}{=} \frac{\partial \tilde{\rho}}{\partial t} = -\frac{i}{\hbar} [H, \tilde{\rho}] + L(\tilde{\rho}), \quad (1.51)$$

is of practical relevance. The resulting system of equations with boundary condition $\text{Tr} \rho \stackrel{!}{=} 1$ can be solved analytically. Under the assumption of negligible dephasing ($\gamma_{21} \ll \Gamma_{21}$) we obtain

$$\tilde{\rho}_{12} = \frac{(i\Gamma_{21} + 2\Delta_{12})\Omega_{21}/4}{\Delta_{12}^2 + \Omega_{12}^2/2 + \Gamma_{21}^2/4}, \quad (1.52)$$

and

$$\tilde{\rho}_{22} = \frac{\Omega_{12}^2/4}{\Delta_{12}^2 + \Omega_{12}^2/2 + \Gamma_{21}^2/4}. \quad (1.53)$$

Absorption

The absorption coefficient of a two-level system is given by the expression [49]

$$\alpha_{n=2} = \frac{2\mathcal{N}\omega_{12}}{\epsilon_0 \mathcal{E}_{0,12} c} d_{12} \text{Im} \tilde{\rho}_{21}. \quad (1.54)$$

With the steady state solution for $\tilde{\rho}_{12}$, this yields

$$\alpha_{n=2} = \frac{2\mathcal{N}\omega_{12}}{\epsilon_0 \mathcal{E}_{0,12} c} d_{12} \frac{\Omega_{12}\Gamma_{21}}{2\Omega_{12}^2 + 4\Delta_{12}^2 + \Gamma_{21}^2}. \quad (1.55)$$

The absorptive profile as a function of the detuning Δ_{12} is hence given by a Lorentzian lineshape.

Saturation

The width of the Lorentzian absorption profile, eq. (1.55), is determined by

$$\Gamma' = \Gamma_{21} \sqrt{1 + \frac{2\Omega_{12}^2}{\Gamma_{21}^2}}. \quad (1.56)$$

This motivates to define the saturation intensity for the transition such that

$$\frac{I}{I_{\text{sat}}} = \frac{2\Omega_{12}^2}{\Gamma_{21}^2} \Rightarrow I_{\text{sat}} = \frac{\hbar c \epsilon_0 \Gamma_{21}^2}{4|d_{12}|^2}. \quad (1.57)$$

It is apparent that for intensities much lower than the saturation intensity, $I \ll I_{\text{sat}}$, the width Γ' of the absorption profile is determined only by Γ_{21} , and the absorption coefficient, α , is independent of the intensity. For higher intensities, the profile is power-broadened, and the linewidth is increased. Further, α depends on the intensity, and therefore the Beer-Lambert law is not valid. The effective absorption decreases in comparison to the non-saturated case.

1.7.2 Three-level ladder system

Rydberg states in alkali vapors (cf. chap. 2) can in principle be addressed in a single excitation step. The required ultraviolet wavelengths are accessible nowadays, even in commercially available laser systems. Using a two-photon ladder scheme, however, bears several experimental and conceptual advantages: Due to the intermediate step, the necessary wavelengths are in the visible or near-infrared, and a coupling with high Rabi frequencies can be achieved. Also, the two independent lasers allow for monitoring the transmission of one laser, while changing the properties of the second. Lastly, dipole-selection rules require the additional excitation step if addressing a (Rydberg) S state is desirable [15, 20]. It is for these reasons that the three-level ladder scheme was chosen for the work in this thesis. The theoretical description and notations of the excitation dynamics for a three-level system are provided in this subsection. Afterwards, the effect of electromagnetically-induced transparency and Autler-Townes splitting is discussed.

A schematic view of the three-level system is shown in fig. 1.2. The system has a ground state, $|1\rangle$, an intermediate state, $|2\rangle$, and an excited state, $|3\rangle$. In vector notation, we define the basis of the three states as

$$|1\rangle \equiv \begin{pmatrix} 1 \\ 0 \\ 0 \end{pmatrix} \quad |2\rangle \equiv \begin{pmatrix} 0 \\ 1 \\ 0 \end{pmatrix} \quad |3\rangle \equiv \begin{pmatrix} 0 \\ 0 \\ 1 \end{pmatrix}. \quad (1.58)$$

This sorts the components of the density matrix into the pattern

$$\rho = \begin{pmatrix} \rho_{11} & \rho_{12} & \rho_{13} \\ \rho_{21} & \rho_{22} & \rho_{23} \\ \rho_{31} & \rho_{32} & \rho_{33} \end{pmatrix}, \quad (1.59)$$

of which 6 entries are independent. The states are coupled pairwise by the two light fields

$$\mathcal{E}_{12}(t) = \mathcal{E}_{12}(t)\hat{\epsilon}_{12} = \frac{1}{2} \left(\mathcal{E}_{0,12} e^{i\omega_{12}t} + \text{c.c.} \right) \hat{\epsilon}_{12} \quad (1.60)$$

$$\mathcal{E}_{23}(t) = \mathcal{E}_{23}(t)\hat{\epsilon}_{23} = \frac{1}{2} \left(\mathcal{E}_{0,23} e^{i\omega_{23}t} + \text{c.c.} \right) \hat{\epsilon}_{23}, \quad (1.61)$$

whereas the transition from $|1\rangle$ to $|2\rangle$ is usually referred to as the probe transition, and the passage from $|2\rangle$ to $|3\rangle$ represents the coupling transition.

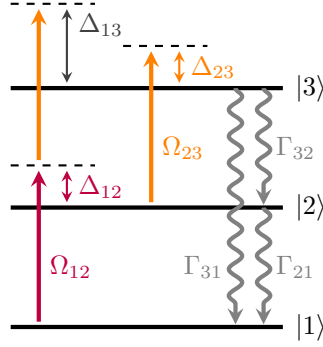


Figure 1.2: Diagram of the three-level ladder system.

The full Hamiltonian reads

$$\begin{aligned} H &= H_0 + H_{AL} \\ &= \hbar \begin{pmatrix} 0 & 0 & 0 \\ 0 & \omega_2 & 0 \\ 0 & 0 & \omega_3 \end{pmatrix} + \begin{pmatrix} 0 & -d_{12}\mathcal{E}_{12}(t) & 0 \\ -d_{21}\mathcal{E}_{12}(t) & 0 & -d_{23}\mathcal{E}_{23}(t) \\ 0 & -d_{32}\mathcal{E}_{23}(t) & 0 \end{pmatrix}. \end{aligned} \quad (1.62)$$

Transforming into the rotating frame, via

$$U = \begin{pmatrix} 1 & 0 & 0 \\ 0 & e^{-i\omega_{12}t} & 0 \\ 0 & 0 & e^{-i(\omega_{12}+\omega_{23})t} \end{pmatrix}, \quad (1.63)$$

yields

$$\tilde{H} = \hbar \begin{pmatrix} 0 & \frac{1}{2}\Omega_{12} & 0 \\ \frac{1}{2}\Omega_{12}^* & -\Delta_{12} & \frac{1}{2}\Omega_{23} \\ 0 & \frac{1}{2}\Omega_{23}^* & -\Delta_{12} - \Delta_{23} \end{pmatrix}, \quad (1.64)$$

In analogy to the two-level system, the detunings are defined with respect to the energy levels, eq. (1.46). The Rabi frequencies are defined in eq. (1.7).

Figure 1.2 also indicates the decay channels. According to eqs. (1.12) and (1.16), the Lindblad operator consists of

$$L_{\text{decay}}(\tilde{\rho}) = \begin{pmatrix} \Gamma_{21}\tilde{\rho}_{22} + \Gamma_{31}\tilde{\rho}_{33} & -\frac{1}{2}\Gamma_{21}\tilde{\rho}_{12} & -\frac{1}{2}\Gamma_{31}\tilde{\rho}_{13} \\ -\frac{1}{2}\Gamma_{21}\tilde{\rho}_{21} & -\Gamma_{21}\tilde{\rho}_{22} + \Gamma_{32}\tilde{\rho}_{33} & -\frac{1}{2}(\Gamma_{21} + \Gamma_{31} + \Gamma_{32})\tilde{\rho}_{23} \\ -\frac{1}{2}\Gamma_{31}\tilde{\rho}_{31} & -\frac{1}{2}(\Gamma_{21} + \Gamma_{32} + \Gamma_{31})\tilde{\rho}_{32} & -(\Gamma_{31} + \Gamma_{32})\tilde{\rho}_{33} \end{pmatrix} \quad (1.65)$$

and

$$L_{\text{deph}}(\tilde{\rho}) = \begin{pmatrix} 0 & -\frac{1}{2}\gamma_{12}\tilde{\rho}_{12} & -\frac{1}{2}\gamma_{13}\tilde{\rho}_{13} \\ -\frac{1}{2}\gamma_{21}\tilde{\rho}_{21} & 0 & -\frac{1}{2}\gamma_{23}\tilde{\rho}_{23} \\ -\frac{1}{2}\gamma_{31}\tilde{\rho}_{31} & -\frac{1}{2}\gamma_{32}\tilde{\rho}_{32} & 0 \end{pmatrix}, \quad (1.66)$$

respectively.

Electromagnetically-induced transparency

Electromagnetically-induced transparency (EIT) describes an effect that can occur in atomic systems with more than two energy levels. By coupling one of the involved levels to a third, an atomic transition between two states becomes transparent for a resonant, and therefore otherwise absorbed light field [50].

EIT spectroscopy involving Rydberg atoms has become a versatile tool for diverse applications: due to the longevity of these states, concise measurements of broadening mechanisms are feasible. For example, some protocols for microwave sensing [51] rely on precise spectra resolving the Autler-Townes splitting [52] of the Rydberg state.

In relevance for this thesis, measuring the resonance position of the additional transition allows for conclusions on energy shifting interactions. We exclusively study 3-level ladder systems, where we tune the first laser on resonance to the transition from the ground-state to an intermediate state, while sweeping the second laser detuning across the two-photon resonance position with a Rydberg state. By measuring the transmission signal of the first laser with a photo-diode, a transparency peak at an otherwise flat background is obtained. The spectral position is then compared to a corresponding reference setup.

1.8 Motional effects

The experiments in this thesis are conducted in vapor cells, with an atomic gas that is held at room temperature or above. A typical range is $T = 300$ to 400 K. In contrast to ultracold atoms experiments $T \lesssim 100$ μ K, where the temperature of a cloud of particles is reduced by a variety of elaborate procedures, vapor cell experiments comprise the velocity as an integral part. In this section, the three main motional broadening effects, Doppler, transit time and collisions, are described.

An exception to this is the so-called frozen gas [53–55], a regime where excitation bandwidths and timescales allow a treatment of the system, as if the atomic motion was effectively suspended.

1.8.1 Doppler broadening

In a thermal ensemble, the velocity of the atoms is given by the Maxwell-Boltzmann distribution. The obvious candidate for an inhomogeneous broadening mechanism is therefore due to the Doppler effect: The absorption frequency for each atom moving at different velocities \mathbf{v} is shifted to

$$\omega'_{ij} = \omega_{ij} - \mathbf{k}_{ij} \cdot \mathbf{v}, \quad (1.67)$$

when \mathbf{k}_{ij} is the wave vector of the light field. This affects a shift of the detunings in the Hamiltonian, eqs. (1.47,1.64),

$$\Delta_{ij}(\mathbf{v}) = \Delta_{ij} - \mathbf{k}_{ij} \cdot \mathbf{v}, \quad (1.68)$$

with respect to the detuning of the light field in the laboratory frame. In the case of a single laser beam, or all wave-vectors \mathbf{k}_{ij} being oriented in parallel, only the velocity component in beam direction is relevant. The Doppler average of such Gaussian ensemble is then

$$\bar{\rho}(\Delta) = \sqrt{\frac{m}{2\pi k_B T}} \int_{-\infty}^{\infty} dv \rho(\Delta, v) e^{-\frac{mv^2}{2k_B T}}, \quad (1.69)$$

where k_B is the Boltzmann constant, m the mass of the particles, and

$$\delta_D = \sqrt{8 \ln 2 \cdot \frac{k_B T}{m}} \quad (1.70)$$

the full width at half maximum of the velocity distribution. As an example, the Doppler averaged absorption profile in the two level atom, eq. (1.55), becomes the convolution of

a Lorentzian curve and a Doppler profile. The result is a Voigt profile [56], with a width of

$$\delta_V = \sqrt{\Gamma^2 + \delta_D^2}. \quad (1.71)$$

For experiments applying spectroscopy in thermal vapor, this effect is typically the dominant contribution to the overall line width. In multi-photon excitation schemes, the Doppler broadening can be diminished by using a suitable geometry of the laser beams. For two lasers, this requires co- or counter-propagating beams [57], using three or more transitions also allows for more elaborate geometric configurations [58]. A lower boundary for resonant excitation schemes is imposed by the residual Doppler width [59],

$$\delta_{D,\text{res}} = \sum_{i=2}^{n-1} k_{i,i+1} \cdot \frac{\Gamma_{21}}{k_{12}}, \quad (1.72)$$

as a result of the wave vector mismatch [60]. In this simplified picture with co-linear lasers, the transition to the first intermediate state *selects* a velocity band from which on atoms further interact with the light field.

1.8.2 Transit time broadening

In a typical vapor cell experiment, the beam diameters of the interrogating laser beams are smaller than the lateral confinement due to the cell walls. Hence, the atoms can enter and leave the laser beam during the interaction with the light field. The timescale of the dynamics is therefore limited to

$$\tau \sim \frac{D}{\bar{v}}, \quad (1.73)$$

where D is a measure for the size of the interaction volume, and \bar{v} the typical velocity of the atoms,

$$\bar{v} = \sqrt{8k_B T / (\pi m)}. \quad (1.74)$$

Atoms that enter the laser beams are typically in the ground state, whereas particles that leave the light field have undergone the excitation dynamics. It is therefore reasonable, to treat the transit time effects as an effective decay rate,

$$\Gamma_{\text{TT}} \sim \frac{1}{\tau} \sim \frac{\bar{v}}{D}. \quad (1.75)$$

As an approximation, the different velocity classes in a thermal ensemble can be represented by a single effective decay rate. In order to determine a sensible value, the actual time scales of the excitation dynamics, and the exact geometry of the intensity profiles

have to be considered. For Gaussian beams with a waist of w_0 , a suitable expression for Γ_{TT} is found [61] by

$$\Gamma_{\text{TT}} = \frac{1}{w_0 \sqrt{2 \log 2}} \sqrt{\frac{8k_{\text{B}}T}{\pi m}}. \quad (1.76)$$

1.8.3 Collisional broadening

The event of a collision suddenly disturbs the phase of an atomic wavefunction. As a consequence of the uncertainty principle, the frequency of the atomic transition in the time domain is less well defined and thus the spectral width appears broadened. In general, we distinguish three types of collisions that contribute to the broadening of an atomic line:

- Inelastic collisions, where the state of the atom is changed, such as n - or l -changing and also ionizing collisions (cf. sec. 2.4),
- elastic collisions, where the collision partner impacts on the valence electron, and
- collisions with the ionic core.

The most abundant collisions are two-body processes, each occurring between an atom and a single perturber. The corresponding collision rate, and thus the broadening rate, is given by

$$\Gamma = \mathcal{N}_{\text{P}} \cdot \bar{v} \cdot \sigma, \quad (1.77)$$

and depends on the density of perturbers, \mathcal{N}_{P} , as well as the cross-section of the respective process. The mean relative velocity between the two collisional partners A and B is given by

$$\bar{v} = \sqrt{\frac{8k_{\text{B}}T}{\pi\mu}}, \quad (1.78)$$

where the reduced mass reads

$$\mu = \frac{m_{\text{A}}m_{\text{B}}}{m_{\text{A}} + m_{\text{B}}}. \quad (1.79)$$

2 Rydberg atoms

When at least one of the electrons of an atom has a large principal quantum number, the atom is called a Rydberg atom. Although there is no specific threshold for the nomenclature, and no convention what a *large* principal quantum number is, usually atoms with $n \gtrsim 15$ are labeled in this way. Nevertheless, Rydberg atoms have in common that the outer electrons orbit the ionic core at large distances. The electrons are therefore only weakly bound to the nucleus, giving rise to exaggerated properties of Rydberg-excited atoms, when compared to, e.g., ground state atoms of the same species. In particular, the energy required to ionize a Rydberg atom—separating the electron from the ionic core—significantly decreases with higher principal quantum number. In combination with the exceptionally high sensitivity to electromagnetic fields [62–64], this enables the phenomenon of optical bistability, which is the main subject of this thesis.

In the following chapter, Rydberg atoms and their properties will be introduced. The energy shifts due to the Stark effect in electric fields will be covered. Finally, we will discuss the interaction between Rydberg atoms. Since the experiments in this thesis only rely on the use of alkali vapors, the discussion is restricted to atoms with only one (excited) valence electron.

2.1 General properties

Rydberg atoms are named in honor of the Swedish scientist Johannes Rydberg [65]. Shortly after its discovery, he generalized Balmer’s observations for hydrogen [66] to the well known formula

$$\frac{1}{\lambda} = -R_\infty \left(\frac{1}{n_1^2} - \frac{1}{n_2^2} \right), \quad (2.1)$$

where λ is the emitted wavelength of the transition, and n_1 and n_2 are the principal quantum numbers of the involved states. Assuming the electron mass to be negligible in comparison to the mass of the nucleus, the binding energy of a state with principal quantum number n is simply given by

$$E_n = -\frac{m_e q_e^4}{8\epsilon_0^2 h^2} \cdot \frac{1}{n^2} = -hc \frac{R_\infty}{n^2}, \quad (2.2)$$

with the Rydberg constant

$$R_\infty = \frac{m_e q_e^4}{8c_0 \epsilon_0^2 h^3}. \quad (2.3)$$

The physical constants are defined in the usual notation:

- h Planck constant ($\hbar = h/2\pi$),
- c_0 speed of light ,
- ϵ_0 vacuum permittivity ,
- m_e mass of an electron and
- q_e elementary charge .

The probability distribution of the Rydberg electron is (spatially) strongly delocalized from the inner shells of the atomic structure. The potential of the Z protons in the nucleus attracting the valence electron is effectively shielded by the $Z - 1$ inner electrons. This is specially true for high angular momentum states. However, for the low angular momentum states ($l < 4$, S, P, D and F states, *defect states*), the remnant penetration of the valence electron into the inner shells does have a sizable influence, appearing as a shift on the energy levels. The effect can elegantly be described by introducing the *effective* principal quantum number

$$n^* = n - \delta_{nlj}, \quad (2.4)$$

thus maintaining the austere beauty of eq. (2.2). The quantum defect, δ_{nlj} , is usually expressed in a series expansion [67]

$$\delta_{nlj} = \delta_{lj,0} + \sum_{k=2,4,\dots} \frac{\delta_{lj,k}}{(n - \delta_{lj,0})^k}, \quad (2.5)$$

and lifts the angular momentum degeneracy of the energy levels. Also considering the finite mass m_+ of the nucleus and the electron, eq. (2.2) becomes

$$E_{nlj} = -hc \frac{R_\infty}{(1 + m_e/m_+)} \cdot \frac{1}{n^{*2}}. \quad (2.6)$$

The Rydberg-Ritz coefficients, $(\delta_{lj,2k})_{k \in \mathbb{N}}$, are usually determined by precision measurements [68–70], individually for each element and for each set of quantum numbers. The values for the elements and states addressed in the course of this thesis are summarized in tab. 2.1. It is noteworthy, that for cesium S states, the quantum defect has almost integer value. Hence, the hydrogen-like high- l manifold energetically lies close to the Rydberg S states.

state		δ_0	δ_2
^{85}Rb	$nS_{1/2}$	3.131 180 4(10)	0.1784(6)
^{133}Cs	$nS_{1/2}$	4.049 356 65(38)	0.237 703 7
	$nD_{5/2}$	2.466 315 24(63)	0.013 577

Table 2.1: Coefficients for the quantum defects for states addressed in this thesis. Cesium values are taken from [68], rubidium from [70].

In a similar fashion to the energy levels, many properties of Rydberg atoms scale with an integer number power of the effective principal quantum number. The scaling behavior is shown in tab. 2.2.

property	scaling	typ. value
binding energy	n^{*-2}	8.2 meV
level spacing	n^{*-3}	$2\pi \times 102.6$ GHz
orbital radius	n^{*2}	$1653 a_0$
radiative lifetime	n^{*3}	40.8 μ s
dipole moment $\langle 7P_{3/2} er nD \rangle$	$n^{*-3/2}$	$0.063 ea_0$
polarizability	n^{*7}	$2\pi \times -356$ MHz/(V/cm) ²
C_3 coefficient	n^{*4}	$2\pi \times 2.13$ GHz $\cdot \mu\text{m}^3$
C_6 coefficient	n^{*11}	$2\pi \times 371$ MHz $\cdot \mu\text{m}^6$

Table 2.2: The exaggerated properties of Rydberg atoms scale with effective principal quantum number n^* [27, 71]. Typical values for the Cs $42D_{5/2}$, $m_J = 1/2$ are given as an example. The pair-interaction of the C_3 coefficient is for $|42D_{5/2}, 42D_{5/2}\rangle \rightarrow |40F_{7/2}, 43P_{3/2}\rangle$.

2.2 Stark effect

Analogous to the Zeeman effect in magnetic fields [72, 73], atoms exposed to an electric field (e.g., the field due to ionized Rydberg atoms) obtain an energy shift called the *Stark effect* [74, 75]. Most often, the energy corrections are negligibly small, e.g., the shift for the rubidium D_1 transition [76] is on the order of $2\pi \times 60$ kHz/(kV/cm)². Rydberg atoms, however, are exceptionally sensitive to electric fields. The energy correction to the $41S$ state in rubidium [47] amounts to $2\pi \times 12.6$ MHz/(V/cm)². At a distance of $1 \mu\text{m}$ to one single ion, this results in a shift of about $2\pi \times 1.3$ GHz, in this case towards lower energy.

2.2.1 Quadratic Stark effect

The Coulomb force of an electric field $\mathcal{E} = \mathcal{E}\hat{\epsilon}$, where $\hat{\epsilon}$ is the unit vector defining the polarization of the field, adds an additional term to the Hamiltonian

$$H_{\mathcal{E}} = -\mathbf{d} \cdot \mathcal{E} = -\mathcal{E} \mathbf{d} \cdot \hat{\epsilon}, \quad (2.7)$$

where $\mathbf{d} = e\mathbf{r}$ is the electric dipole operator and \mathbf{r} the position operator of the electron in the potential of the nucleus. The new, shifted states with respect to the unperturbed energy levels are obtained by diagonalization of the full Hamiltonian

$$H = H_a + H_{\mathcal{E}}, \quad (2.8)$$

where H_a is the Hamiltonian of the unperturbed atom, with eigenenergies as given in eq. (2.6).

For small contributions $\mathbf{d} \cdot \boldsymbol{\mathcal{E}}$, the Stark shift for an atom in sublevel $\mathbf{k} = (n, l, j, m)$ can be calculated using second order perturbation theory [77],

$$E_{\text{Stark},k} = -\langle k | \hat{\mathbf{d}} \cdot \boldsymbol{\mathcal{E}} | k \rangle + \sum_{i \neq k} \frac{\langle k | \hat{\mathbf{d}} \cdot \boldsymbol{\mathcal{E}} | i \rangle \langle i | \hat{\mathbf{d}} \cdot \boldsymbol{\mathcal{E}} | k \rangle}{E_k - E_i}. \quad (2.9)$$

Since $\mathbf{d} \cdot \boldsymbol{\mathcal{E}}$ has odd parity, and for $l < 4$ the degeneracy of the states is lifted by the quantum defect, the linear term vanishes, and the energy shift is quadratic in \mathcal{E} . Introducing the polarizability α yields [78]

$$\begin{aligned} E_{\text{Stark}} &= -\frac{1}{2} \alpha \mathcal{E}^2 \\ &= -\frac{1}{2} \left(\alpha_0 + \alpha_2 \left[\frac{3m_J^2 - J(J+1)}{J(2J-1)} \right] \right) \mathcal{E}^2, \end{aligned} \quad (2.10)$$

where the total polarizability α consists of the scalar polarizability α_0 and a tensor polarizability α_2 , which depends on the total angular momentum J and its projection along the quantization axis z . For electric fields at an angle to a quantization axis, the term reads

$$E_{\text{Stark}} = -\frac{1}{2} \alpha_0 \mathcal{E}^2 + -\frac{1}{2} \alpha_2 \left[\frac{3m_J^2 - J(J+1)}{J(2J-1)} \right] \frac{3\mathcal{E}_z^2 - \mathcal{E}^2}{2}. \quad (2.11)$$

For alkali S states, the angular dependence vanishes because the second term is zero for $J = |m_J| = 1/2$. The Stark shift is hence characterized by the scalar polarizability [79], until level crossings and coupling to neighboring states perturb the quadratic trend.

2.2.2 Stark maps

For larger fields, the perturbative approach is not justified anymore, thus, the diagonalization of the Hamiltonian has to be carried out. Depending on the state in question, several hundreds of energy levels have to be included in the calculation. Powerful software packages exist, that enable such computations with ease [47, 80]. Usually, constructing the matrix of the Hamiltonian is followed by numerical diagonalization for a whole series of different electric field strengths. This results in the typical representation as a *Stark map*, an example of which is shown in fig. 2.1.

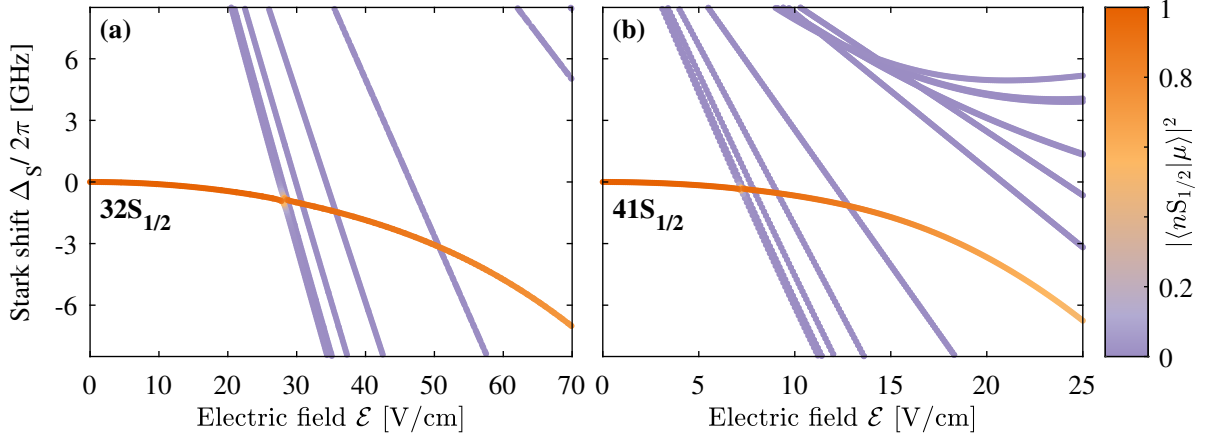


Figure 2.1: Calculated Stark maps for rubidium S states, using [80]. Notice the different range of electric fields for $n = 32$ (left) and $n = 41$ (right) due to the strong n -scaling of the polarizability. For the $41S_{1/2}$ state, level crossings with the hydrogenic manifold (straight lines) and neighboring P, D and F states are visible. The overlap with the unperturbed states is displayed in the color map.

2.3 Rydberg-Rydberg interactions

Rydberg interactions are one of the most well-studied fields in physics, which has awakened interest in the scientific community for several decades [16, 20, 51, 81–83]. Due to the large polarizability and huge dipole moments of inter-Rydberg transitions, the energy landscape of an atom can be heavily influenced due to presence of other Rydberg atoms close by. For instance, the energy required to excite a rubidium atom to the $41S$ state is shifted by $2\pi \times -1.35$ GHz at $1 \mu\text{m}$ distance to a second atom that is in the same $41S$ state.

The interplay between Rydberg atoms is typically handled as a binary interaction, i.e., a pairwise interaction between two atoms at a distance $\mathbf{R} = R\hat{\mathbf{r}}$, each having one electron excited to a Rydberg orbit. Further, we make use of the Born-Oppenheimer approximation [84] to write the Hamiltonian as

$$H(\mathbf{R}) = H_a + H_{\text{int}}(\mathbf{R}), \quad (2.12)$$

again, $H_a = H_{a,1} \otimes H_{a,2}$ giving the unperturbed eigenenergies as in eq. (2.6), but for the pair of two atoms. The operator $H(\mathbf{R})$ is comprised of the interaction between the two Rydberg electrons and the two ionic cores, in all pairwise combinations. Since the core-electron attraction within each atom is already considered by H_a , the additional interaction potential in H_{int} is given by the term

$$V_{\text{int}} = \frac{e^2}{4\pi\epsilon_0} \left(\frac{1}{R} + \frac{1}{R'} - \frac{1}{r_{12}} - \frac{1}{r_{21}} \right), \quad (2.13)$$

where the separations R, R', r_{12} and r_{21} denote the distances as depicted in fig. 2.2.

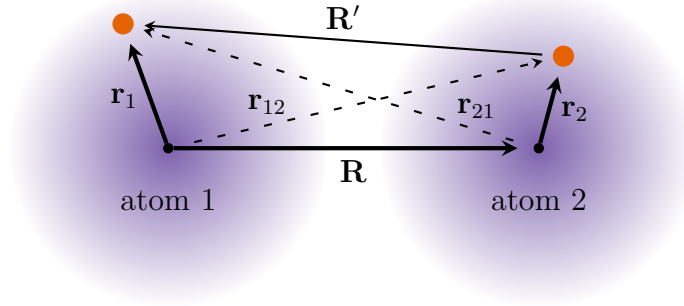


Figure 2.2: Two-center coordinate system of two interacting Rydberg atoms, each composed of nucleus (black center) and electron (orange blob). The purple shaded area represents the extend of the electron wavefunction, indicating the LeRoy radius. For valid calculations of the interaction, there must be no significant overlap between the two atoms. This is the case when the distance R is larger than the LeRoy radius.

For large interatomic distances, eq. (2.13) can be approximated with a multipole expansion

$$V_{\text{int}} = \frac{e^2}{4\pi\epsilon_0} \sum_{L_1, L_2=1}^{\infty} \sum_{M=-L_<}^{L_<} \frac{f_{L_1, L_2, M}}{R^{L_1+L_2+1}} Q_{L_1, M}(\mathbf{r}_1) Q_{L_2, -M}(\mathbf{r}_2). \quad (2.14)$$

In this equation, $Q_{L, M}(\mathbf{r})$ is the multipole operator for each atom, defined with the spherical harmonics Y_{LM} ,

$$Q_{L, M}(\mathbf{r}) = \left(\frac{4\pi}{2L+1} \right)^{1/2} r^L Y_{L, M}(\hat{\mathbf{r}}) \quad (2.15)$$

and

$$f_{L_1, L_2, M} = \frac{(-1)^{L_2} (L_1 + L_2)!}{[(L_1 + M)!(L_1 - M)!(L_2 + M)!(L_2 - M)!]^{1/2}}. \quad (2.16)$$

Distances are considered *large*, when the wavefunctions of the electrons of the two atoms do not overlap. This is fulfilled for $R > R_{\text{LR}}$, where the LeRoy radius [85] is given by

$$R_{\text{LR}} = 2 \left(\langle k_1 | \hat{\mathbf{r}}^2 | k_1 \rangle^{1/2} + \langle k_2 | \hat{\mathbf{r}}^2 | k_2 \rangle^{1/2} \right), \quad (2.17)$$

for states with quantum numbers $k_i = (n_i, l_i, j_i, m_i)$. The LeRoy radius of the 41S–41S pair state in rubidium is $R_{\text{LR}} = 0.5 \mu\text{m}$.

The L in the multipole expansion, eq. (2.14), indicates the order of the operators: $Q_{1, M}$ are dipole operators, $Q_{2, M}$ is the set of quadrupole operators, $Q_{3, M}$ for octopole, etc. The limit for the summation in eq. (2.14) is

$$L_< = \min(L_1, L_2), \quad (2.18)$$

accordingly. Note the absence of the monopole operator, as both atoms are neutral.

Similar to the Stark maps (cf. sec. 2.2.2), we calculate pair-potential maps by constructing the Hamiltonian, followed by numerical diagonalization for the series of inter-atomic distances. The projection of each new, shifted eigenstate $|\mu\rangle$ onto the unperturbed pair states quantifies the admixture of the unperturbed pair states

$$E_{k_1, k_2}^{|\mu\rangle} = \langle k_1, k_2 | \mu \rangle. \quad (2.19)$$

This yields a measure for the coupling strength when exciting pair states with a defined laser beam.

2.3.1 Dipole-dipole interaction

The pair-state energy landscape in Rydberg atoms is often of a very complex and turbid nature. Since eq. (2.14) is the expansion of rising order multipole operators, a typical simplification is to truncate the series at suitable degree. The dominant contribution for large atomic distances is the coupling term between two dipoles [86],

$$V_{\text{dd}}(\mathbf{R}) = \frac{\hat{\mathbf{d}}_1 \cdot \hat{\mathbf{d}}_2 - 3(\hat{\mathbf{d}}_1 \cdot \hat{\mathbf{r}})(\hat{\mathbf{d}}_2 \cdot \hat{\mathbf{r}})}{4\pi\epsilon_0 R^3}. \quad (2.20)$$

For the introductory discussion, we focus on rubidium S-states. On the one hand, due to the spherical symmetry of the S-states, the interaction lacks an angular dependency [87]. On the other hand, the neighboring states of an nS state in rubidium are the P-states above and below, nP and $(n-1)P$, respectively [88]. This makes the discussion more straightforward, and allows us to identify the dipole operators in eq. (2.20) with $\hat{\mathbf{d}}_1 = \langle (n-1)P | e\hat{\mathbf{r}} | nS \rangle$ and $\hat{\mathbf{d}}_2 = \langle nP | e\hat{\mathbf{r}} | nS \rangle$, as sketched in fig. 2.3. In the basis of pair states, we now only consider the dipole couplings to $|nS, nS\rangle$ are $|(n-1)P, nP\rangle$ and $|nP, (n-1)P\rangle$.

Under the assumption that the energy separation,

$$\Delta = E_{nP} + E_{(n-1)P} - 2E_{nS, nS}, \quad (2.21)$$

is smaller than any other dipole-allowed pair state, the Hamiltonian reads

$$H = \begin{pmatrix} 0 & \kappa & \kappa \\ \kappa & \Delta & 0 \\ \kappa & 0 & \Delta \end{pmatrix}, \quad (2.22)$$

where we define the coupling parameter

$$\kappa = \frac{d_1 d_2}{4\pi\epsilon_0 r^3}. \quad (2.23)$$

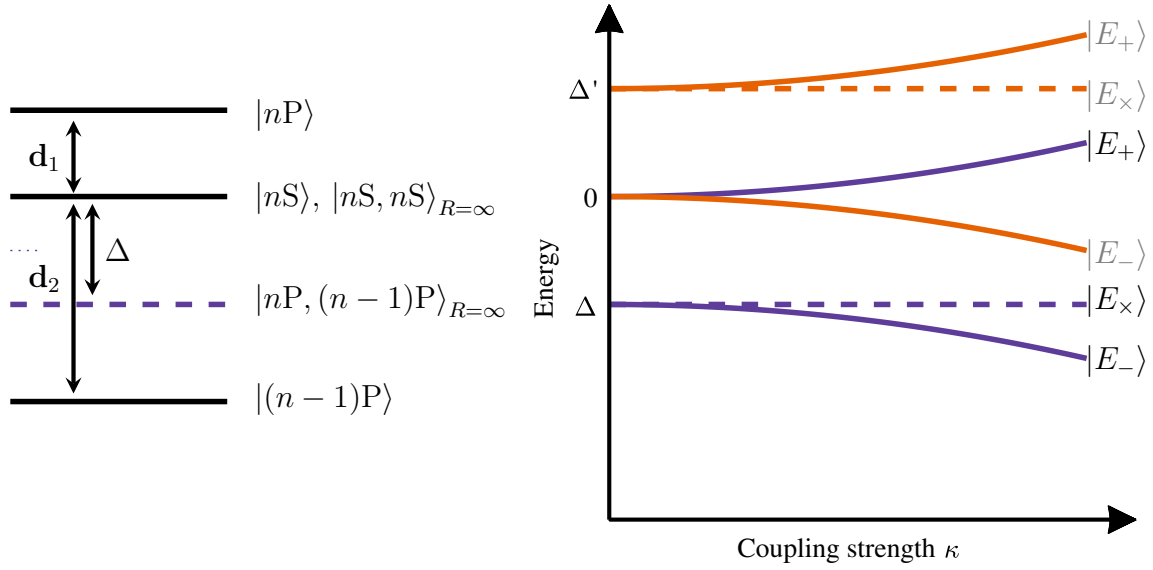


Figure 2.3: Schematic of the van-der-Waals energy landscape for $|nS\rangle$ states in the presence of a second atom. The neighboring levels provide an energy mismatch, Δ . The scenario on the left assumes a higher lying $|nP\rangle$ neighbor which is closer than the lower lying $|(n-1)P\rangle$, and therefore $\Delta < 0$. The dashed line indicates the *per atom* energy in the pair basis exactly in the center between $|nP\rangle$ and $|(n-1)P\rangle$. The three new eigenstates as described in the text are depicted by the purple lines on the right. For the opposite case, when $\Delta' > 0$, the orange lines would be relevant.

By diagonalization, we get three eigenvalues:

$$E_{\pm} = \frac{\Delta}{2} \pm \sqrt{\left(\frac{\Delta}{2}\right)^2 + 2\kappa^2}, \quad (2.24)$$

and

$$E_{\times} = \Delta. \quad (2.25)$$

The corresponding eigenstates are

$$\begin{aligned} |\pm\rangle &= |nP, (n-1)P\rangle + |(n-1)P, nP\rangle + \frac{E_{\pm}}{2\kappa} |nS, nS\rangle \\ |\times\rangle &= |nP, (n-1)P\rangle - |(n-1)P, nP\rangle, \end{aligned} \quad (2.26)$$

of which only the symmetric ones ($|\pm\rangle$) couple to an $\langle P|$ state via the dipolar interaction with a light field. In a two-photon excitation scheme, the intermediate state from which atoms are then excited to the Rydberg state is typically a P state.

For $\Delta = 0$, the r -dependence vanishes, which means that the states $|\pm\rangle$ always contain admixtures of both S and P character. This implies a permanent electric dipole moment

of the pair state [89], and the interaction strength indeed decreases with r^{-3} . The energy of such a Förster resonance [90] is given by

$$E_{\text{Förster}} \stackrel{\Delta=0}{\equiv} \sqrt{2}\kappa \equiv -\frac{C_3}{r^3}. \quad (2.27)$$

The corresponding coefficient scales with $C_3 \propto n^{*4}$, since the dipole moments scale like n^{*2} . Resonant dipole-dipole interaction is also dominant for small distances, at which $\kappa \gg \frac{|\Delta|}{2}$.

For the opposite limit, in case of larger distances, the interaction energy is much smaller than the energy mismatch Δ . The energy shift can be expanded in a Taylor-series, and becomes [87, 91]

$$E_{\text{vdW}} \stackrel{\kappa \ll \frac{|\Delta|}{2}}{\approx} -\frac{2\kappa^2}{\Delta} \equiv -\frac{C_6}{r^6}, \quad (2.28)$$

which has an r^{-6} behavior and is called *van-der-Waals* shift or London dispersion interaction [92], accordingly. The scaling of the coefficient goes as $C_6 \propto n^{*11}$, due to the scaling of the dipole moments and the n^{*-3} dependence of the level spacing, cf. tab. 2.2.

At this point, we want to emphasize on the sign of the interaction. For $\Delta > 0$, state $|+\rangle$ can be identified as $|nS, nS\rangle$ at infinite separation of the atoms. For $\Delta < 0$, it is $|-\rangle$, and the Taylor series in both cases results in eq. (2.28). As already indicated, the closest pair state to any $|nS, nS\rangle$ pair of rubidium atoms with a dipole-allowed transition is $|nP, (n-1)P\rangle$, which has lower energy [87], $\Delta < 0$. Therefore, the pair-potential is repulsive between rubidium S states.

2.4 Ionization processes

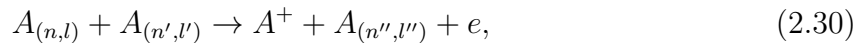
Rydberg atoms are unusually susceptible to ionization for mainly two reasons: For one thing, the binding energy—and thus the first ionization energy—is exceptionally small which sets a shallow threshold for such processes. And for another thing, due to the large geometric size of the Rydberg orbitals the probability of ionizing reactions to happen is heavily increased compared to ground-state atoms. Ever since Rydberg atoms became the focus of more in-depth studies, ionization has always needed proper examination [35, 53] and careful experimental consideration [93].

2.4.1 Collisional ionization

The particles of a thermal vapor—as in the very definition of it—continually propagate with thermal velocity. At room temperature, i.e., $T \approx 300$ K, this complies to a kinetic

energy that, on average, is on par with the binding energy of typical Rydberg principal quantum numbers. As an example, for rubidium S-states, the $26S_{1/2}$ state has a binding energy that is almost equal to the average kinetic energy. Note that also for states below $26S$, the collision energy can exceed the binding energy, in this case a smaller fraction of the collisions can ionize the Rydberg atoms. Hence, inelastic collisions, where the valence electron can be disassociated from its ionic core are a relevant factor that contributes to the properties of the gas. In the event of a collision involving a Rydberg atom, different interaction mechanisms come to play, depending on the nature of the colliding partner. References [94–96] represent a nice series of publications; thorough theoretical background of the subject can be found in [97].

For collisions of an alkali atom in the Rydberg state (n, l) with other alkali atoms, the two processes that lead to ions in the vapor are



where the first reaction is referred to as *associative ionization*, and the latter is denoted as *Penning-type* ionization. Due to the large size of Rydberg atoms, the cross-sections for such events are correspondingly large.

Irrespective of the exact microscopic picture and the details of the accompanying interaction mechanism of such collisions, relevant for the discourse of this thesis is the overall ionization rate due to collisions. The equation for this comes from eq. (1.77). The attributed cross-sections σ_i are on the order of the size of a Rydberg atom, which is

$$\sigma_i \sim \pi(a_0 n^{*2})^2. \quad (2.31)$$

From experiments with cesium atoms [35], we obtain $\sigma_i \approx 0.06\pi (a_0 n^{*2})^2$.

Collisions with charged particles have also been thoroughly studied, both theoretically [97, 98] and experimentally [99, 100]. Being much lighter than any alkali atom, the velocity of the electron compared to the alkali is tremendously faster (for cesium by a factor of about 500). Hence, the collision rate is also increased by these almost three orders of magnitude. The reaction of this process reads



The collision changes the energy E of the electron by Δ_E .

Since electrons are the product of every ionization process in the vapor, significant densities of electrons can accumulate, especially in continuous wave laser beam experiments. The cross-sections for ionization due to collisions with electrons are similarly determined by the size of the Rydberg atom. Experiments in sodium [101] provide cross-sections on

the order of $20\sigma_{\text{geo}}$, but note that the actual value depends on the velocity of the electron. The maximum of the curve, however, is at very low electron energies, close to the ionization threshold of the Rydberg atom [102]. For rubidium and cesium Rydberg atoms—to the best of our knowledge—there are no experimentally verified publications for electron impact ionization at low kinetic energies.

2.4.2 Photoionization

The physical process in which a valence electron is dissociated from its nucleus due to incident photons is referred to as photoionization. The reaction formula here reads



If the energy of one photon is larger than the binding energy a transfer of the electron to the continuum is possible. Cross-sections for photoionization of an atomic state with quantum numbers n and l can be calculated using the power dependence of the form [103]

$$\sigma_{n,l} = \sigma_{n,l}^{\text{thr}} \left(\frac{\omega^{\text{thr}}}{\omega} \right)^{\beta_{n,l}}, \quad (2.34)$$

and the empirical values (i.a., the exponent $\beta_{n,l}$) for rubidium and cesium [104]. In this formalism, $\sigma_{n,l}^{\text{thr}}$ is the threshold cross-section, where the laser frequency ω matches the binding energy $\hbar\omega^{\text{thr}}$. Values of $\sigma_{n,l}^{\text{thr}}$ for the relevant states within this work are on the order of $1 \times 10^{-16} \text{ cm}^2$. Given that the Rydberg states are already very close to the ionization threshold, it becomes apparent that the ionization probability due to the excitation lasers is often negligible: The laser frequency addresses the transition between distinct states. If the photon energy is actually above the ionization threshold the excess energy of the photons is typically quite large; the cross-section is greatly reduced by the second factor in eq. (2.34).

If the photon energy does not reach the ionization limit, the electron can be dissociated via multiple-photon absorption [105], which has even smaller cross-sections.

Black-body radiation

Ionization can also happen due to photo-ionization by photons of the black-body radiation spectrum. Due to the temperature of the experimental environment photons in the broad spectrum of thermal radiation are always present. Possible ionization paths are by either direct ionization,



or via a step-wise process,

$$A_{(nl)} + \hbar\omega_{\text{BBR},1} + \hbar\omega_{\text{BBR},2} \rightarrow A_{(n'l')} + \hbar\omega_{\text{BBR},2} \rightarrow A^+ + e. \quad (2.36)$$

Because the energy spacing between Rydberg atoms is so small, finding a matching photon in the spectrum is not impossible, although the probability is quite low: Estimations in [106] provide ionization rates on the order of a few kilohertz. In cold atom laboratories, black body radiation can already significantly influence the outcome of an experiment [107, 108]. In thermal vapor experiments, the ionization rate is usually negligible in comparison to the collisional effects.

2.5 Recombination

The reverse process to ionization is recombination. By capturing a free electron from the environment, the alkali ion again neutralizes. In its basic form, this is

$$A^+ + e \rightarrow A_{(nl)}. \quad (2.37)$$

Typically, the ion-electron pair does not end up in the ground state of the atom but in a Rydberg state[67]. Subsequently, the newly bound state further decays after the specific lifetime, or is ionized again.

The recombination process is typically described as a volume effect, following the rate equation

$$\frac{\partial \mathcal{N}_e}{\partial t} = -\alpha \mathcal{N}_e \mathcal{N}_+, \quad (2.38)$$

with a recombination coefficient that is on the order of $\alpha = 0.1$ to $1 \times 10^{-11} \text{cm}^3/\text{s}$ [109].

On closer inspection, several mechanisms contribute to recombination e.g., in a plasma, and the reaction in eq. (2.37) is not strictly correct. To fulfill energy conservation, the often times existing mismatch in kinetic energy and binding energy is either radiated

$$A^+ + e \rightarrow A_{(n,l)} + \hbar\omega, \quad (2.39)$$

or consumed by a third collision partner,

$$A^+ + e + e(E) \rightarrow A_{(n,l)} + e(E + \Delta_E). \quad (2.40)$$

An introductory study of the mechanisms of electron-ion recombination can be found for example in [109, 110].

3 Plasmas and electric fields

The typical definition for a plasma reads as follows: A plasma is a quasi-neutral gas that consists of positively and negatively charged particles which are subject to electric, magnetic and other forces, and which exhibit a collective behavior [111]. It is due to the long-range electromagnetic fields that mediate the interactions between the charged particles, that makes the macroscopic properties of a plasma so different from a normal gas. In contrast to collisions between neutral atoms who only exhibit local forces, collective phenomena can occur in this *fourth state of matter*.

Rydberg atoms, as introduced in the previous chapter, are highly likely to be ionized. This holds especially true in thermal vapors, where collisions between the atoms frequently occur. In this chapter, we discuss the relevant concepts that allow us to identify an ionized gas to be a plasma. Since Rydberg atoms are highly sensitive to electric fields, the electric field distribution within the plasma is also discussed. Only a few basic aspects of the much richer field of plasma physics are introduced here. The remarks in this chapter can be found in most introductory textbooks on the subject of plasmas [111–115].

3.1 Properties of a plasma

As a basic principle, a plasma consists of three components: ions, electrons, and a background of neutral, un-ionized atoms. Arguably for any gas, the admixture of charged particles never vanishes completely, although the fraction of ions and electrons may be arbitrarily low. One can estimate the degree of ionization using the Saha equation [116]

$$\frac{n_i}{n_n} \approx \sqrt{\frac{m_e k_B}{2\pi\hbar^2}} \frac{T^{3/2}}{n_i} e^{-U_i/k_B T}, \quad (3.1)$$

which results from an equilibrium between ionization and recombination processes. Here, n_i is the density of ions (assumed equal to the density of electrons), n_n is the neutral gas density, T is the temperature and U_i quantifies the energy required to ionize an atom. As an example, nitrogen at normal temperature and pressure ($U_i = 14.5$ eV [117], $T \approx 300$ K, $n = 3 \times 10^{19}$ cm⁻³) has a fractional ionization of $n_i/n_n \approx 10^{-122}$. In fact, that is fewer than one ionized atom per number of particles in the known universe [118].¹

¹In one particular "field" of medicine, such *homeopathic* fraction would probably be considered *highly potent*, denoted by 26Q.

At sufficiently high temperatures, the fraction of charged particles begins to dominate the properties of the gas. In the following sections, these properties are introduced. In order for a partially ionized gas to be qualified as a plasma, certain criteria need to be fulfilled.

3.1.1 Debye shielding

A fundamental property of a plasma is the ability to effectively *shield* electric potentials, due to its high mobility of the free charges [119]. Even though in an ideal plasma the number densities of electrons and ions is equal (cf. sec. 3.1.2), the density distribution is not necessarily homogeneous: the electric potential, say, of an ion, is attractive for electrons, but acts repulsive on other ions. As a result, the positively charged ions tend to accumulate negatively charged electrons in their vicinity. When sufficiently close to thermal equilibrium, the number densities of the two species in a potential, $\varphi(r)$, fig. 3.1, are distributed according to Boltzmann[120]

$$n_{i,e} = n \cdot \exp(-q_e\varphi/k_B T_{i,e}), \quad (3.2)$$

where n is the density for a vanishing potential, $T_{i,e}$ the temperature and $\pm q_e$ the electric charge of ions and electrons, respectively. When assuming the mean potential energy between the particles and their nearest neighbor to be small in comparison to the kinetic energy,

$$q_e\varphi/k_B T_{i,e} \ll 1, \quad (3.3)$$

a Taylor expansion [121] to first order of the exponential is sufficient. Poisson's equation for the electric potential in spherical coordinates then reads

$$\begin{aligned} \Delta\varphi = \nabla^2\varphi &= \frac{1}{r^2} \frac{d}{dr} \left(r^2 \frac{d\varphi}{dr} \right) \\ &= \frac{q_e(n_e - n_i)}{\epsilon_0} = \frac{nq_e^2\varphi}{\epsilon_0 k_B} \left(\frac{1}{T_e} + \frac{1}{T_i} \right). \end{aligned} \quad (3.4)$$

The characteristic length scale in a plasma is given by the Debye length

$$\lambda_{d_{i,e}} = \sqrt{\frac{\epsilon_0 k_B T_{i,e}}{nq_e^2}}. \quad (3.5)$$

When we define the total Debye length as the combined length scale of both electrons and ions,

$$\lambda_d^{-2} = \lambda_{d_i}^{-2} + \lambda_{d_e}^{-2}, \quad (3.6)$$

the Poisson equation, eq. (3.4), can be rewritten as

$$\frac{1}{r^2} \frac{d}{dr} \left(r^2 \frac{dr}{d\varphi} \right) = \lambda_d^{-2} \varphi, \quad (3.7)$$

and is solved by the Debye-Hückel potential [119]

$$\varphi(r) = \frac{q}{4\pi\epsilon_0 r} \exp\left(-\frac{r}{\lambda_d}\right). \quad (3.8)$$

The potential of a single charge in both plasma and vacuum is plotted in fig. 3.1.

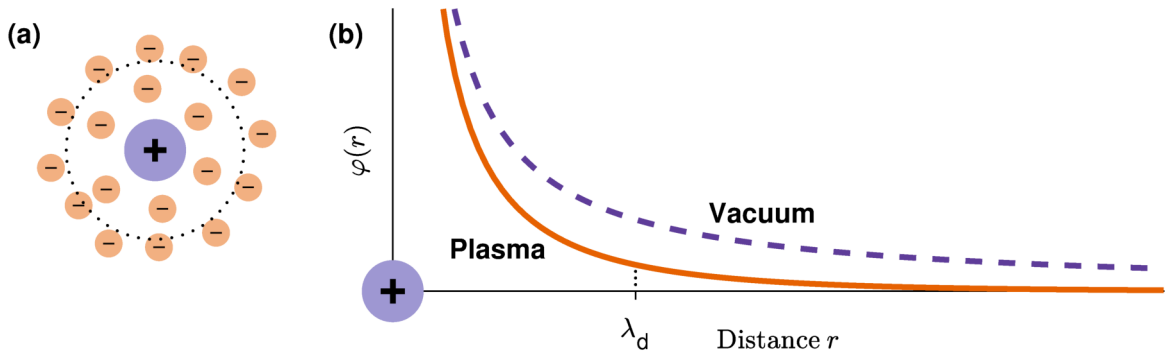


Figure 3.1: Shielding effect in plasmas. Local charge imbalances are compensated by a cloud of electrons. As a result, the electric potential $\varphi(r)$ is effectively shielded, and decreases faster than in vacuum. The dashed purple potential is that of a single charge without shielding. The Debye sphere is indicated by the dotted line.

The first criterion for an ionized gas to be considered a plasma is that the Debye length is shorter than the geometric size of the ionized gas

$$\lambda_d \ll L, \quad (3.9)$$

which implies that any potential due to local charge imbalances becomes shielded on the length scale L under consideration.

3.1.2 Plasma parameter and quasi neutrality

The picture of Debye shielding, as introduced in the previous section, can only be valid if sufficiently many particles participate in the shielding. The plasma parameter quantifies this number of particles within the sphere with a radius of the Debye length:

$$N_d = n \frac{4\pi}{3} \lambda_d^3 = \left(\frac{4\pi\epsilon_0 k_B}{q_e^2} \right)^{3/2} \frac{1}{6\sqrt{\pi}} \frac{T^{3/2}}{\sqrt{n}}. \quad (3.10)$$

The second criterion for *collective behavior*, and also for the ionized gas to qualify as an ideal plasma, is therefore

$$N_d \gg 1. \quad (3.11)$$

Ideal plasma

A typical and well-known classification of an ensemble of charged particles is whether it is an *ideal* plasma. If this is the case, the equation of state for each of the particle species is that of an ideal gas. For such an ideal plasma, binary collisions are negligible in favor of the collective electrostatic interactions. Thus, instead of pair-wise interactions, the plasma particles seemingly only interact with a continuous background field.

Quasi-neutrality

The required large number of particles in the volume V_d of one Debye sphere leads to the concept of quasi-neutrality. Quasi-neutrality is the result of electron screening [122, 123]. A charge, q , is efficiently shielded outside the sphere, if the plasma itself provides an excess charge of the same quantity,

$$e(n_i - n_e)V_d \equiv e\delta n V_d = q. \quad (3.12)$$

For the relative density, this yields

$$\frac{\delta n}{n} = \frac{q/q_e}{N_d}, \quad (3.13)$$

which means that relative density fluctuations within the Debye sphere of $1/N_d$ would impose an excess charge on the order of one elementary charge. Since N_d is large,

$$n_e \approx n_i, \quad (3.14)$$

which is known as the plasma approximation. Closely related to the plasma parameter is the Coulomb coupling parameter, which compares the Coulomb energy to the thermal energy,

$$\Gamma_e = \frac{q_e^2}{4\pi\epsilon_0 k_B T} \sqrt[3]{\frac{4\pi\mathcal{N}_e}{3}}. \quad (3.15)$$

3.1.3 Plasma oscillations

Displacing the electrons from the uniform background of ions creates an electric field in such a way that it forces the electrons back to their original position, and thus restores the

neutrality of the plasma. Because of their inertia, the electrons will overshoot and oscillate around their equilibrium positions. The characteristic frequency of this phenomenon, called the *plasma frequency*, is so fast that—due to their much larger mass—the heavier ions cannot follow the motion.

The equation of motion for the electrons is a Navier-Stokes equation [124] supplemented by the electromagnetic forces. Neglecting magnetic fields and thermal motion of the particles, we obtain

$$m_e n_e \left[\frac{\partial \mathbf{v}_e(\mathbf{r}, t)}{\partial t} + (\mathbf{v}_e(\mathbf{r}, t) \cdot \nabla) \mathbf{v}_e(\mathbf{r}, t) \right] = -q_e n_e \mathcal{E}(\mathbf{r}, t), \quad (3.16)$$

with electric field, $\mathcal{E}(\mathbf{r}, t)$, and electron velocity, $\mathbf{v}_e(\mathbf{r}, t)$. If we assume the number of electrons to be conserved, i.e., no ionization or recombination, also the equation of continuity holds, which is

$$\frac{\partial n_e(\mathbf{r}, t)}{\partial t} + \nabla \cdot (n_e(\mathbf{r}, t) \mathbf{v}_e(\mathbf{r}, t)) = 0. \quad (3.17)$$

For simplicity, the ions are assumed to be fixed in space and are uniformly distributed. Further, the plasma should extend infinitely, and the electron motion is only in x direction. Poisson's equation reads

$$\epsilon_0 \nabla \cdot \mathcal{E}(\mathbf{r}, t) = \epsilon_0 \frac{\partial \mathcal{E}(\mathbf{r}, t)}{\partial x} = q_e (n_i - n_e(\mathbf{r}, t)). \quad (3.18)$$

For small amplitudes of oscillations, one can solve the system of coupled equation by linearization. We separate the dependent variables into the equilibrium solution and a perturbative part:

$$n_e = n_0 + n_1 \quad \mathbf{v}_e = \mathbf{v}_0 + \mathbf{v}_1 \quad \mathcal{E}_e = \mathcal{E}_0 + \mathcal{E}_1 \quad (3.19)$$

Substituting this into eqs. (3.16, 3.17) and neglecting all terms quadratic in amplitude yields

$$m_e \frac{\partial \mathbf{v}_1}{\partial t} = -q_e \mathcal{E}_1 \quad (3.20)$$

$$\frac{\partial n_1}{\partial t} + n_0 \nabla \cdot \mathbf{v}_1 = 0. \quad (3.21)$$

For eq. (3.18), we obtain

$$\epsilon_0 \nabla \cdot \mathcal{E}_1 = -q_e n_1, \quad (3.22)$$

since $n_{i,0} = n_{e,0}$ in equilibrium, and $n_{i,1} = 0$ because the ion positions are fixed. With an

oscillating ansatz,

$$\mathbf{v}'_1 = v_1 \exp(i(kx - \omega t)) \hat{\mathbf{x}} \quad (3.23)$$

$$n'_1 = n_1 \exp(i(kx - \omega t)) \quad (3.24)$$

$$\mathcal{E}'_1 = \mathcal{E}_1 \exp(i(kx - \omega t)) \hat{\mathbf{x}} \quad (3.25)$$

the time derivative and the gradient can be easily evaluated. We obtain

$$-im_e \omega v_1 = -q_e \mathcal{E}_1 \quad (3.26)$$

$$-i\omega n_1 = -n_0 i k v_1 \quad (3.27)$$

$$i k \epsilon_0 \mathcal{E}_1 = -q_e n_1. \quad (3.28)$$

which, for $v_1 \neq 0$, finally leads to the plasma frequency

$$\omega_{pe} = \sqrt{\frac{n q_e^2}{\epsilon_0 m_e}}. \quad (3.29)$$

As a third criterion for the classification as a plasma, these oscillations have to be faster than the timescale τ of collisions of the particles with the un-ionized background gas

$$\omega_p \tau > 1. \quad (3.30)$$

3.2 Electric field distribution

Although plasmas in general are neutral, with positive and negative charges compensating one another, the internal imbalances due to thermal fluctuations cause an electric field distribution. Due to the Debye shielding and possible ion correlations the calculation of these microfield distributions is not trivial. Various approximations have surfaced [125–128], addressing different parameter regimes. For weakly coupled plasmas, where the ions are not correlated and electron screening is negligible, the Holtsmark distribution is apt to model the field strength distribution of the microfield [129]. The probability distribution for the electric field strength \mathcal{E} is given by

$$\mathcal{P}(\mathcal{E}) = \mathcal{H}(\mathcal{E}/\mathcal{Q}_{\mathcal{H}})/\mathcal{Q}_{\mathcal{H}}, \quad (3.31)$$

where the normalizing field for a charge density \mathcal{N} is given by the expression

$$\mathcal{Q}_{\mathcal{H}} = \frac{q_e}{2\epsilon_0} \left(\frac{4}{15} \mathcal{N} \right)^{2/3}, \quad (3.32)$$

and

$$\mathcal{H}(\beta) = \frac{2}{\pi\beta} \int_0^{\infty} dx x \sin(x) \exp\left(-\left(x/\beta\right)^{3/2}\right). \quad (3.33)$$

The mean electric field in this distribution is given by

$$\bar{\mathcal{E}} = \int_0^{\infty} d\mathcal{E} \mathcal{E} \mathcal{H}(\mathcal{E}) \approx 3.38 Q_{\mathcal{H}}. \quad (3.34)$$

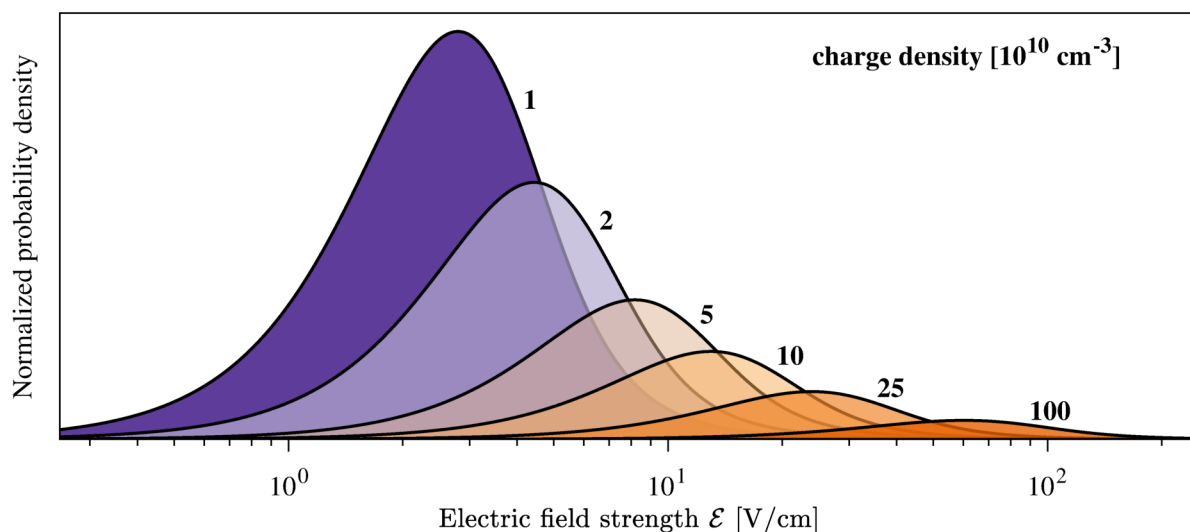


Figure 3.2: Holtsmark probability density distribution for different charge densities, as indicated by the numbers in the plot. The lines are normalized to the area below the curves.

The non-analytic character of the Holtsmark distribution makes it necessary to numerically approach its actual calculation. A suitable substitute is given by the rational approximation from [130]. The asymptotic behaviors are

$$\mathcal{H}(\beta) \sim \begin{cases} \frac{4}{3\pi} \beta^2 & \text{for } \beta \rightarrow 0 \\ \frac{3}{2\pi} \beta^{-5/2} & \text{for } \beta \rightarrow \infty. \end{cases} \quad (3.35)$$

Figure 3.2 exemplarily shows the probability distribution function evaluated for different charge densities.

3.2.1 DC-Stark broadening

Inhomogeneous electric fields have an affect onto an ensemble of atoms that depends on the field properties at the location of each individual atom; the Stark effect (cf. sec. 2.2)

depends on the strength and direction of the electric field. In analogy to the Doppler effect, where the optical Bloch equations of a thermal ensemble of atoms are averaged over all possible velocities, we now have to integrate over all possible electric field configurations. Instead of the Maxwell-Boltzmann distribution, the contributions are weighted with the distribution of the electric fields, i.e., the Holtsmark distribution in case of a dilute plasma. The atomic line with respect to the laser detuning Δ (i.e., a Lorentzian function with a full width at half maximum Γ) is given by

$$L_{\Gamma}(\Delta, \mathcal{E}) = \frac{1}{4} \frac{\Gamma^2}{\left(\Delta + \frac{\alpha \mathcal{E}^2}{2}\right)^2 + \left(\frac{\Gamma}{2}\right)^2} \quad (3.36)$$

where α is the polarizability as introduced in eq. (2.10) and \mathcal{E} the electric field strength. Then the ensemble average is calculated as

$$\overline{L}_{\Gamma}(\Delta) = \int_0^{\infty} d\mathcal{E} L_{\Gamma}(\Delta, \mathcal{E}) \mathcal{P}(\mathcal{E}), \quad (3.37)$$

where the electric field distribution follows eq. (3.31). Figure 3.3 illustrates the shift, broadening and deformation of such an ensemble average. Assuming a scalar polarizability, the lines are shifted towards one side of the spectrum only.

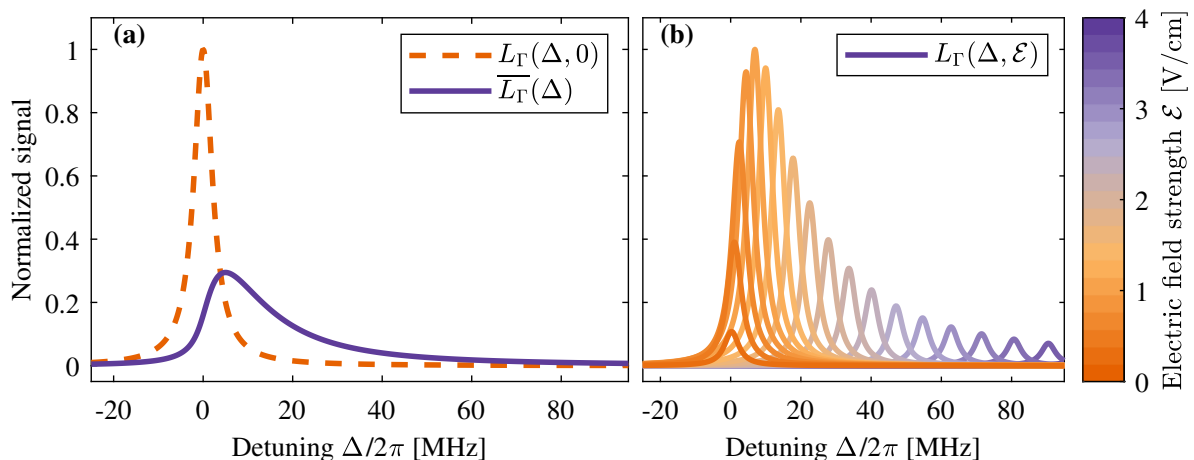


Figure 3.3: Inhomogeneous ensemble of Stark-shifted lines. (a) Original lineshape and Stark affected feature. The shift and broadening of the purple line is clearly visible, as well as the deformation with a tail towards positive detunings. The ensemble average in (a) consists of a superposition of the original line, shifted by the manifold of electric field strengths, as displayed in (b). Example calculation for a Lorentzian line, $\Gamma = 5$ MHz, and polarizability $\alpha = -15$ MHz/(V/cm)².

4 Optical bistability

4.1 Introduction

Bistability refers to the peculiar property of certain systems to have two distinct, but stable equilibrium states at otherwise identical configurations. In other words, for a given input value (among a particular range of input values), a bistable system provides either of two stable output values. According to the definition in [131], such system is required to provide both a non-linearity and a feedback mechanism. Figure 4.1 shows a characteristic curve for a bistable system. In case of *optical* bistability the parameter that is tuned can be, for example, the intensity or the frequency of a light field.

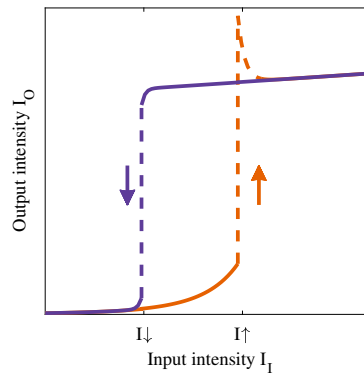


Figure 4.1: Characteristic curve for an optically bistable system. In this example, the input intensity as a parameter is cycled. Depending on the direction and previous state of the system, two different steady states are possible. At critical points, the system switches from one to the other. In this illustration, reproduced from [131], the system exhibits an overshoot, before settling to the steady state. We did not observe this in the intrinsic optical bistability in thermal Rydberg vapor.

Due to the feedback mechanism, a bistable system shows a hysteresis in an observable property when sweeping some parameter back and forth a region of interest. Note that the hysteresis alone is no unique feature to a bistable system: strictly speaking, also *metastable* states can have a relaxation time that is much larger than the time scale of the parameter sweep [132]. Especially in hypothetical considerations, such as, the thermodynamic limit, a rigorous treatment of this matter would be appropriate. However, to simply describe our experiment this strict distinction has no value. In this context, we only seek to explain the following observation: the system has two different steady states that are realized depending on the detuning scan direction.

Optical bistability can be observed in many different systems. The first observation was reported in a sodium vapor using a cavity for the feedback [133], and followed by semiconductor solid state systems [134]. Other systems involve for example nonlinear prisms [135], or photonic crystal cavities [136]. In principle, beside these external mechanisms via a cavity or electronic circuits, the feedback can also be the interactions in a dense bulk of dipoles. Such *intrinsic* or mirrorless optical bistability was demonstrated in a Yb³⁺-doped crystal at cryogenic temperatures [137]. The feedback mechanism that leads to optical bistability as observed in alkali Rydberg vapor experiments [32, 138, 139] is the main subject of this thesis, and will be discussed in detail in part III.

4.2 Mean-field formalism

A picturesque model for optical bistability can be obtained by considering an atomic two-level system as formally introduced in sec. 1.7.1, with the extension of a feedback mechanism that adds a *non-linearity* [140, 141]. Following the derivation from [142], we apply the mean-field approach, and assume an additional effective shift of the energy level of state $|2\rangle$ that only depends on the population of this state, $\tilde{\rho}_{22}$. As a consequence, the detuning between the driving light field and the excited state becomes an effective detuning [143, 144]

$$\Delta_{12}^{\text{eff}} = \Delta_{12} - \kappa\tilde{\rho}_{22}, \quad (4.1)$$

with a mean-field interaction coefficient, κ . The time-evolution of the ensemble is described by the refitted Bloch equations, cf. sec. 1.7.1,

$$\frac{\partial}{\partial t}\tilde{\rho}_{12} = \left(-\frac{\Gamma_{21} + \gamma_{21}}{2} - i\Delta_{12}^{\text{eff}}\right)\tilde{\rho}_{12} - \frac{i}{2}(\tilde{\rho}_{22} - \tilde{\rho}_{11})\Omega_{12}, \quad (4.2)$$

$$\frac{\partial}{\partial t}\tilde{\rho}_{22} = \text{Im}(\tilde{\rho}_{12}\Omega_{12}^*) - \Gamma_{21}\tilde{\rho}_{22}. \quad (4.3)$$

Neglecting the dephasing term γ_{21} , we obtain the steady state solution

$$\tilde{\rho}_{22} = \frac{\Omega_{12}^2/4}{\Delta_{12}^{\text{eff}2} + \Omega_{12}^2/2 + \Gamma_{21}^2/4}. \quad (4.4)$$

Substituting the effective detuning, eq. (4.1), leads to the cubic expression

$$\tilde{\rho}_{22}^3\kappa^2 - \tilde{\rho}_{22}^2 2\kappa\Delta_{12} + \tilde{\rho}_{22} \left(\Delta_{12}^2 + \frac{\Omega_{12}^2}{2} + \frac{\Gamma_{21}^2}{4}\right) - \frac{\Omega_{12}^2}{4} = 0. \quad (4.5)$$

In general, this equation can provide up to three real valued roots for $\tilde{\rho}_{22}$. The domain in which multiple solutions are possible motivates the system to be called bistable: the third solution is merely a mathematical possibility with no vital relevance: the solution

is unstable, and minute fluctuations would tilt the system towards one of the two stable solutions.

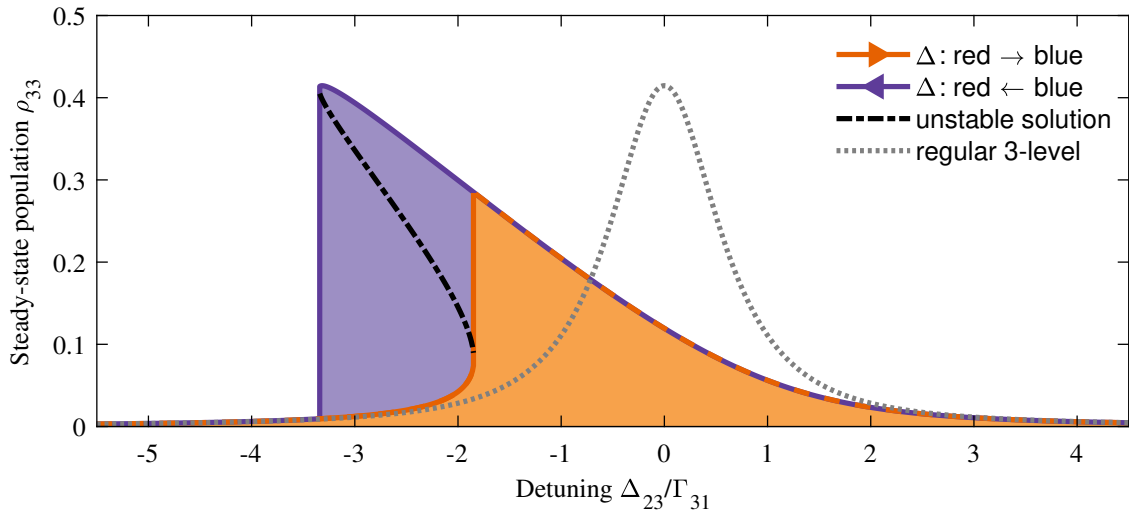


Figure 4.2: Steady-state solution in a three-level system with and without mean-field feedback. Example calculation for $\Gamma_{21} = \Gamma_{31} = \Omega_{12} = \Omega_{23} = 2\pi \times 1$ MHz. Mean-field interaction coefficient $\kappa = -8\Gamma_{31}$ ($\kappa = 0$ for regular three-level system). The system bears three numerical solutions: tracing the detuning from left to right, the system would follow the orange curve. For the opposite sweep direction, the purple curve describes the progress. The difference between the curves manifests as hysteresis. The unstable, third solution splits the hysteresis area, and marks the crossover line at which the system would converge to the respective other steady state if initial ρ_{33} were chosen somewhere between those lines.

The extension to a three-level system is straight forward, although equations become more elaborate. Figure 4.2 shows the numerical solution for both non-interacting ($\kappa = 0$) and mean-field interacting three-level system with feedback in place ($\kappa = -8\Gamma_{31}$). The steady-state population $\tilde{\rho}_{33}$ is shown in dependence of the laser detuning Δ_{23} , assuming $\Delta_{12} = 0$. When *dynamically* sweeping this laser detuning across the resonance of an atomic line, the bistable character of the system comes to play: while for the non-interacting system, the feature has the same shape for both scan directions, for the mean-field shifted system an asymmetry arises. For a detuning sweep from red to blue detunings (i.e., negative to positive frequency values) the orange curve in fig. 4.2 describes the progress of $\tilde{\rho}_{33}$. For the opposite sweep, the purple trajectory is valid. At the two vertical lines, the system undergoes a first-order phase transition [145], and suddenly jumps from low to high population $\tilde{\rho}_{33}$ in the excited state, or vice versa.

The mean-field model qualitatively reproduces the emergence of an intrinsic optical bistability in a two- or three-level Rydberg system. It is clear that for a primal understanding of the underlying mechanisms, a more elaborate model is necessary. Especially the thermal motion of the atom is not considered in this simplified picture, and the interaction between particles is rendered via a highly empirical parameter.

Part II

Distinction between Rydberg-Rydberg Interactions and Charge Induced Bistability

5 Part II: Introduction

Together with the discovery of the *Nonequilibrium Phase Transition in a Dilute Rydberg Ensemble* [32], the authors have published an empirical model that qualitatively explains the observed phenomenon. The mean-field model provided in the manuscript shows qualitative agreement, and reproduces a bistable response of the atomic system. However, the underlying mechanism that causes the bistability is not unveiled persuasively. In the original manuscript, the authors speculate that interactions between Rydberg atoms are responsible for the observed behavior of the system. Based on our own observations of the same phenomenon, our suspicion is that ionized Rydberg atoms could play the dominant role here, instead of Rydberg-Rydberg interactions. Here we present an experimental study that is directly sensitive to the interaction mechanisms and thus allows to discriminate between the two effects.

In this first experimental part of the thesis we investigate the phenomenon of optical bistability in a driven ensemble of Rydberg atoms. By performing two complementary experiments with thermal vapors of rubidium and cesium, we are able to shed light on the underlying interaction mechanisms causing the nonlinear behavior that leads to the phenomenon of *intrinsic optical bistability* in thermal Rydberg vapor. Due to the different properties of these two atomic species, we conclude that the large polarizability of Rydberg states in combination with electric fields of spontaneously ionized Rydberg atoms is the relevant interaction mechanism. In the first part (the experiment involving rubidium) we directly measure the electric field in a bistable situation via two-species spectroscopy, exploiting the availability of the two natural abundant isotopes of the element. In the second part (the procedure comprising a cesium vapor) we make use of the different signs of the polarizability for different l states. The setup also provides the possibility to apply electric fields. Both these experiments allow us to rule out dipole-dipole interactions and support our hypothesis of a charge-induced bistability.

This part of the thesis is based on the experiments and findings that were worked into the manuscript *Charge-induced optical bistability in thermal Rydberg vapor*. It has been published as a research article in *Physical Review A* in 2016 [146]. The measurements based on the cesium setup are contributed by Alban Urvoy; the setup was originally designed and used in [147].

6 Setup and methods

6.1 Two-species rubidium spectroscopy

Figure 6.1 shows the experimental setup for the rubidium part of the experiment. A 2-mm-thick glass cell containing the rubidium vapor is placed at the focus of two pairs of beams. The cell is a spectroscopy cuvette (quartz glass, Hellma Analytics) connected to a reservoir and filled with a droplet of naturally abundant rubidium mixture (i.e., 72% ^{85}Rb and 28% ^{87}Rb) under vacuum. The temperature of the reservoir is stabilized to control the vapor density, while a higher cell temperature ($T_{\text{cell}} = 135^\circ\text{C}$) prevents unwanted condensation of the alkali. By measuring and fitting the absorption profile of the the D_1 line [148], the vapor density of the two isotopes was determined as $\mathcal{N}_{85} = 1.8 \times 10^{12} \text{ cm}^{-3}$ and $\mathcal{N}_{87} = 0.7 \times 10^{12} \text{ cm}^{-3}$, respectively. This corresponds to a reservoir temperature of about $T_{\text{res.}} = 86^\circ\text{C}$, which was kept constant at this setting for all rubidium measurements presented here.

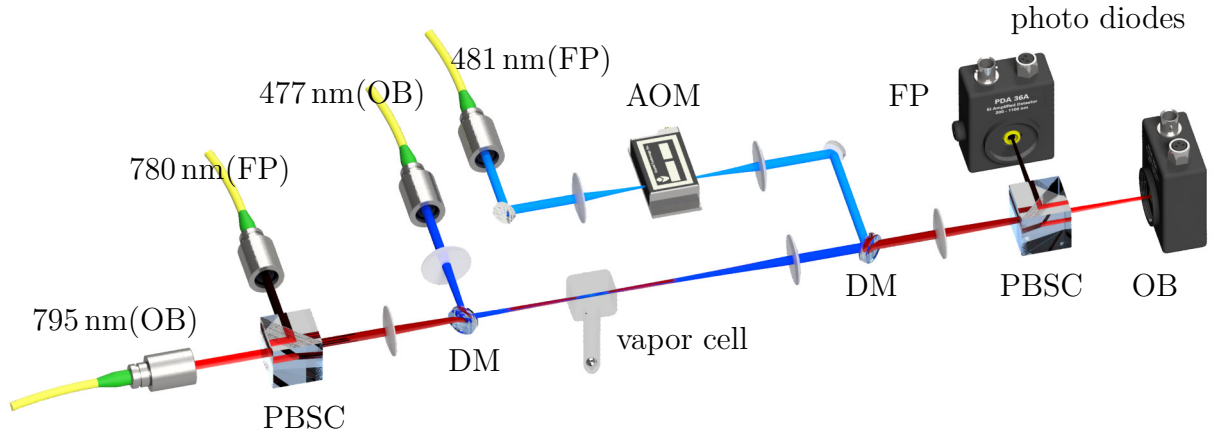


Figure 6.1: Setup of the rubidium experiment. Two pairs of lasers drive the two isotopes in the same volume using an EIT-like excitation scheme, fig. 6.2. One pair drives an optical bistability with the scheme EIT_{OB} , while the other one probes for local fields via EIT_{FP} . The lasers are overlapped and separated with polarizing beamsplitter cubes (PBSC) and dichroic mirrors (DM). The acousto-optic modulator (AOM) acts as a chopper, for lock-in amplification of the EIT_{FP} scheme. All four laser beams are focused in the center of the 2-mm long vapor cell.

We drive an optical bistability in ^{85}Rb similar to the work in reference [32]. Atoms of the isotopic species ^{85}Rb are addressed with an EIT-like excitation scheme [37], as depicted in fig. 6.2(a). In the following, this scheme is referred to as EIT_{OB} .

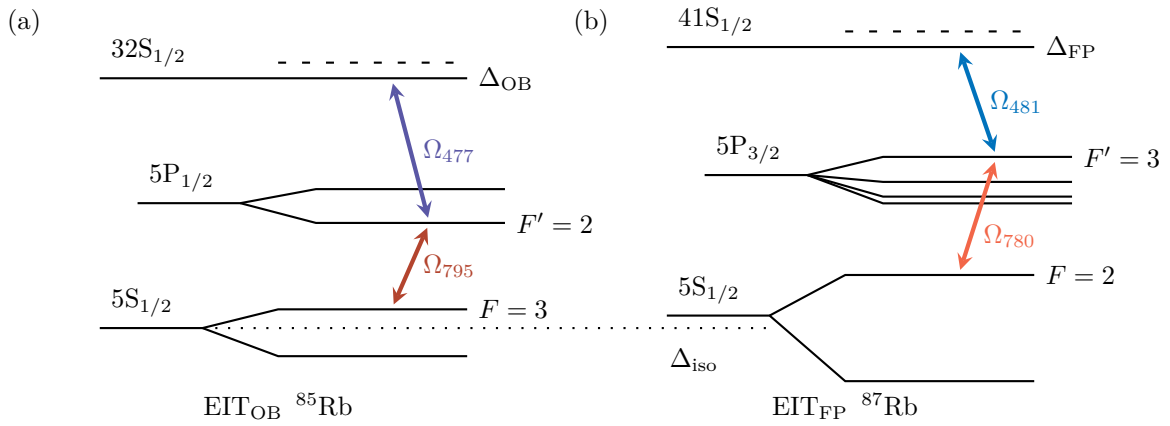


Figure 6.2: Relevant transitions in the resonant two-photon excitation schemes. (a) EIT_{OB} drives the optical bistability for ^{85}Rb atoms. (b) EIT_{FP} acts as a probe for the electric fields inside the cell, using the (less abundant) ^{87}Rb isotope.

The vapor is probed by measuring the transmission of a frequency-stabilized 795 nm laser, which is locked onto the ^{85}Rb $5\text{S}_{1/2}, F = 3 \rightarrow 5\text{P}_{1/2}, F' = 2$ transition, with a typical Rabi frequency of $\Omega_{795}/2\pi = 37$ MHz. The second laser in this scheme couples the atoms to a Rydberg state. This 477 nm laser is scanned over the transition $5\text{P}_{1/2} \rightarrow 32\text{S}_{1/2}$ with a detuning Δ_{477} and Rabi frequencies up to $2\pi \times 25$ MHz, limited by the available laser power and the given beam geometry. The two laser beams are focused down to a waist of $40 \mu\text{m}$ and overlapped in the center of the glass cell. The transmission of the 795 nm laser is then monitored as a function of the detuning. Since we expect bistable behavior with a spectrum depending on the scan direction, we record both positive and negative sweeps, i.e., scanning from red to blue wavelengths, and vice versa.

We chose the co-propagating configuration, since this results in a simple Lorentzian-like excitation spectrum, as plotted in fig. 6.3. Due to population shelving to the long-lived Rydberg state [149], the transmission signal of the 795 nm laser is roughly proportional to the population of the Rydberg state. In contrast, the dependence between Rydberg population and probe transmission in the counter-propagating configuration [37, 60, 150] has a richer structure, which would unnecessarily complicate the analysis. In fact, the Rydberg population in this case follows a bi-modal, M -shaped distribution, fig. 6.3, that is symmetric to the (single-peak) transmission feature of the probe light. Any effect that (directly or indirectly) depends on the Rydberg population would potentially reach a certain threshold value multiple times in a single detuning sweep. If the effect leads to hysteresis, as is the case for optical bistability as discussed in this context, the resulting measurements might lead to a difficult interpretation [138, 151].

In order to probe into the mechanisms and the cause of the optical bistability, we simultaneously measure an additional EIT-like spectrum [37] on the less abundant isotope ^{87}Rb , hereafter named EIT_{FP} , for *field probe*. The advantage of using two different isotopes is

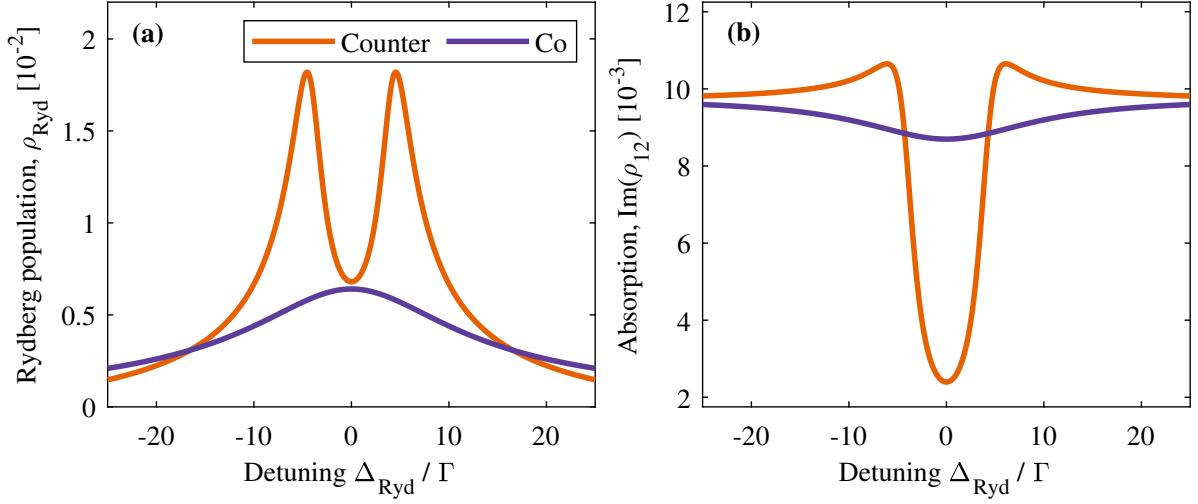


Figure 6.3: Co- vs. counter-propagating laser beams in the three-level scheme as used for EIT_{OB}, calculated according to the system of equations from sec. 1.7.2. The shown traces are the result of Doppler averaging over the thermal ensemble, at a temperature of $T = 135$ °C. Model parameter in units of $\Gamma/2\pi = 6$ MHz: $\Omega_{795} = 2\Gamma$, $\Omega_{477} = 5\Gamma$, $\gamma = 0.1\Gamma$.

that except for interspecies interactions, the two schemes are completely decoupled due to the different wavelengths of the transitions. Similar to the excitation scheme EIT_{OB} presented above, we use two lasers at 780 nm (probe, $\Omega_{780}/2\pi = 66$ MHz) and 481 nm (coupling, $\Omega_{481}/2\pi = 10$ MHz) to drive the ladder scheme $5S_{1/2}, F = 2 \rightarrow 5P_{3/2}, F' = 3 \rightarrow 41S_{1/2}$ of ^{87}Rb , fig. 6.2(b). Again, the 780 nm laser is locked on resonance and the 481 nm laser has a variable detuning Δ_{481} with respect to the upper transition. These two additional laser beams are overlapped with the previous pair. Differing from the EIT_{OB} arrangement, the 780 nm and 481 nm lasers are counter-propagating and the polarizations of EIT_{FP} are perpendicular to EIT_{OB}.

By independently scanning Δ_{481} and Δ_{477} , we obtain two-dimensional transmission spectra of the 780 nm probe laser, an example of which is shown in fig. 7.3(a). The laser detunings are calibrated using a Fabry-Pérot interferometer (free spectral range $\Delta\nu_{\text{FSR}}/2\pi = 1.5$ GHz) in combination with an EIT reference signal. Since the choice of Rabi frequencies compromises between a narrow linewidth and signal visibility, the signal-to-noise ratio is improved by amplitude-modulating the 481 nm laser with an acousto-optic modulator with a frequency of 30 kHz and demodulating the transmission signal using a lock-in amplifier (Femto, LIA-MV-200).

6.2 Cesium spectroscopy

In the experiment based on ^{133}Cs , we excite the atomic vapor with the inverted two-photon ladder scheme $6S_{1/2}, F = 3 \rightarrow 7P_{1/2}, F' = 4 \rightarrow nl$ as depicted in fig. 6.4.

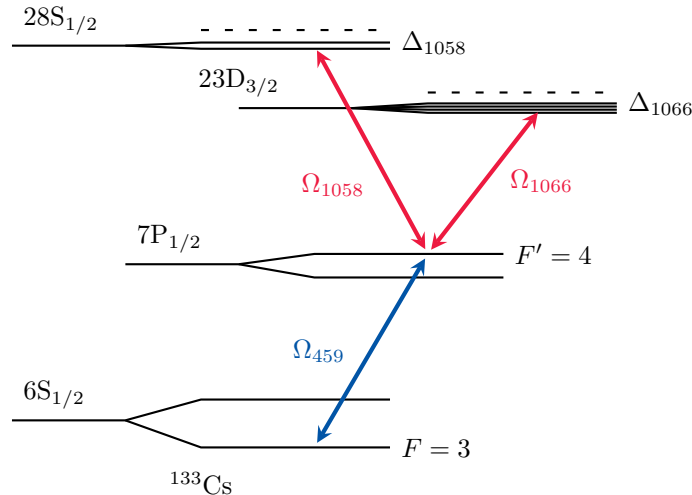


Figure 6.4: Relevant transitions in the *inverted* ladder scheme. In cesium, we can address both S and D Rydberg states as well as a broad range of principal quantum numbers, and thus especially manipulate the sign of the interaction. We refer to the Rydberg laser as the 1060-nm laser.

Our measurements with cesium are performed using counter-propagating lasers as sketched in fig. 6.5. Both lasers are focused into a 3 mm vapor cell, where the illuminated spot-size has a $1/e^2$ radius of $50\ \mu\text{m}$. We determine the cesium density inside the cell to be $\mathcal{N}_{\text{Cs}} = 1.2 \times 10^{13}\ \text{cm}^{-3}$, by recording and fitting the absorption profile of the D_2 spectrum. In the inverted level scheme, where the wavelength of the lower transition is *shorter* than the one for the upper transition, additional decay channels and transit time broadening result in a signal with enhanced absorption [60]. Regarding the shape of the Rydberg population as a function of the detuning, the same argument holds as for the rubidium setup; only for the inverted scheme, both co- and counter-propagating configuration provide a transmission signal that is roughly corresponding to the Rydberg population. We chose the counter-propagating setup for a better separability of the two lasers. Since we measure the transmission of the blue light, the residual transmission of the dichroic mirrors would be an additional background to the actual light level of interest.

The Rabi frequency for the lower transition at 459 nm is set to $\Omega_{459}/2\pi = 6\ \text{MHz}$, while for the upper transitions at approximately 1060 nm we chose $\Omega_{1060}/2\pi = 146\ \text{MHz}$. Similar to the rubidium experiment described in the previous section, the transmission signal of the 459 nm light is measured directly on a photo-diode while varying the 1060 nm detuning Δ_{1060} .

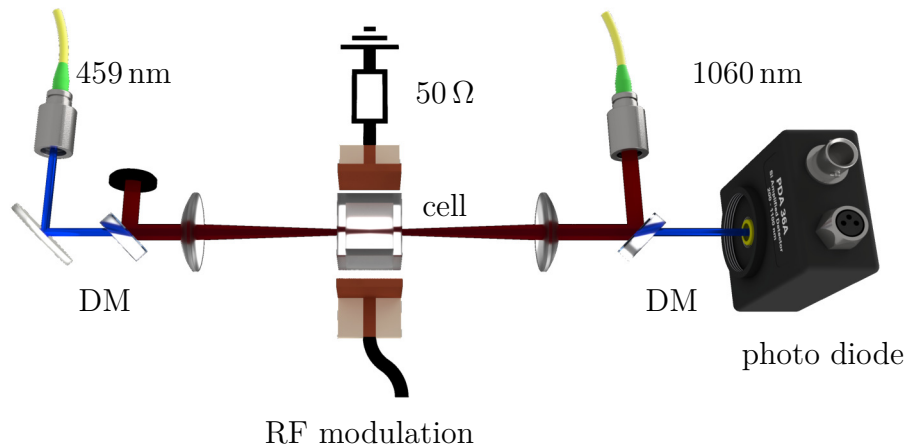


Figure 6.5: Setup of the cesium experiment. Two counter-propagating laser beams are focused in the center of a 3-mm-thick cesium vapor cell. The cell is placed between two electrodes, where an electric field modulation can be applied on one port, while the second is $50\ \Omega$ terminated. The lasers are polarized in parallel to the electric field between the two plates.

With the use of a fiber amplifier we can reach higher Rabi frequencies on the upper transition with cesium than in our rubidium setup. Furthermore, we can address Rydberg states with various principal quantum numbers in two different orbital angular momentum states ($n = 20$ to 60 , $l = S, D$). This allows us to examine the response of systems with different properties. In the context of this part of the thesis, we will consider in particular the Rydberg states $23D_{3/2}$ and $28S_{1/2}$, which have opposing signs of the polarizability.

The major additional feature available in the cesium setup is the ability to externally apply an electric field across the cell. The glass cell is placed between two electrodes, fig. 6.5, that produce an electric field roughly parallel to the polarization of the laser beams. A specially designed strip-line [147] guides the applied microwave to an electrode next to the spectroscopy cell. Possible frequencies range from DC to several GHz. The electrode on the opposite side is terminated with $50\ \Omega$. For our measurements, we inject a sine wave with frequencies of 10 to 500 MHz, yielding an oscillating electric field between the electrodes with an amplitude of approximately $3\ \text{V cm}^{-1}$.

7 Results and discussion

7.1 Two-species rubidium spectroscopy

7.1.1 Optical bistability

Figure 7.1 shows typical traces of the EIT_{OB} system. With increasing Rabi frequencies of the coupling laser, the peak is visibly shifted towards the red and becomes more and more distorted until at sufficiently large intensity the hysteresis appears and the system becomes bistable, as in reference [32]. The analogous observation in cesium is shown in fig. 7.8.

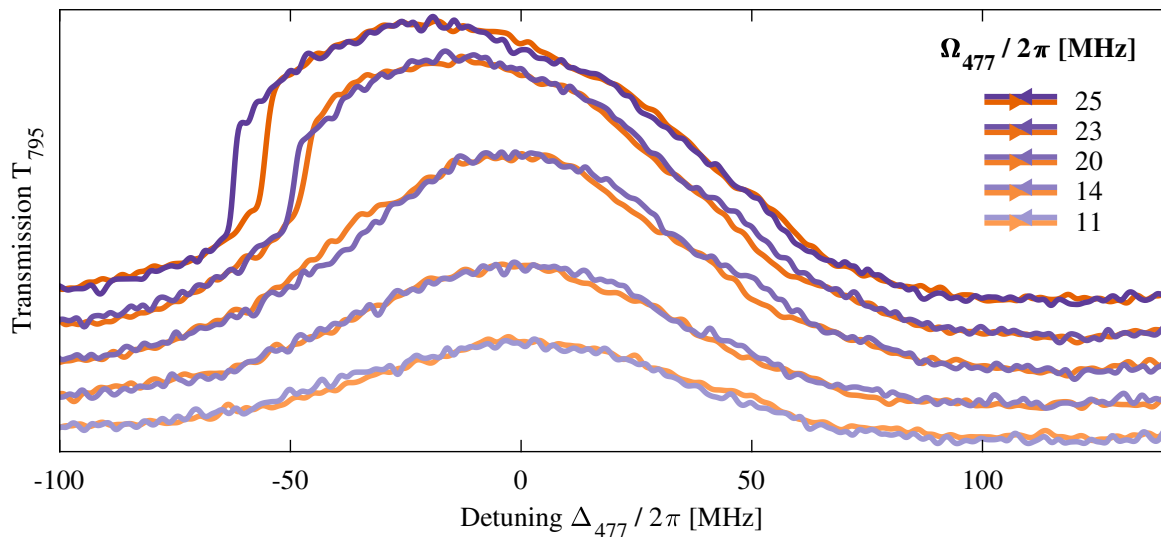


Figure 7.1: Transmission signal of the EIT_{OB} system the rubidium setup. As the laser intensity is raised, the peak amplitude and shift increases. At a sufficiently large Rabi frequency, a hysteresis window appears: the system shows bistability. The lines are offset for better visibility.

The phenomenon of optical bistability is the result of a competition between a nonlinear energy shift which is indirectly dependent on the Rydberg state population, and the decay from the Rydberg state. On the one hand, when the laser frequency is scanned in negative direction, i.e., from the blue detuned side to the red, there is a buildup of Rydberg population that in turn *sustains* the ability to excite Rydberg atoms—even further away from resonance. When the detuning becomes too large, the decay mechanisms prevail and the population eventually breaks down. This results in a sudden change of the

transmission level, as can be observed in the purple lines in fig. 7.1. On the other hand, when the frequency is scanned in positive direction (orange lines), the Rydberg population stays low in the bistable region until the detuning becomes small enough to sufficiently excite atoms. These atoms then act as a seed for subsequent excitations, as atoms close by can be shifted closer to resonance. When a certain threshold is reached, a sudden increase in population is triggered, switching the system to the high population state. Overall, the expected hysteresis in the transmission spectrum can be observed. In fig. 7.1 (and also later in fig. 7.2), besides a broadening of the signal, the sign of the shifts (in both schemes) clearly indicates *attractive* interactions.

7.1.2 Interspecies interaction

A complementary observation to the effects of the Rydberg population onto the driving light field itself can be made when studying the signal of the additional Rydberg EIT scheme EIT_{FP} . By design, this additional EIT scheme probes the inter-atomic interactions in the same excitation volume where the optical bistability is induced. For a fixed detuning Δ_{477} , we observe the signal in the EIT_{FP} scheme as displayed in fig. 7.2.

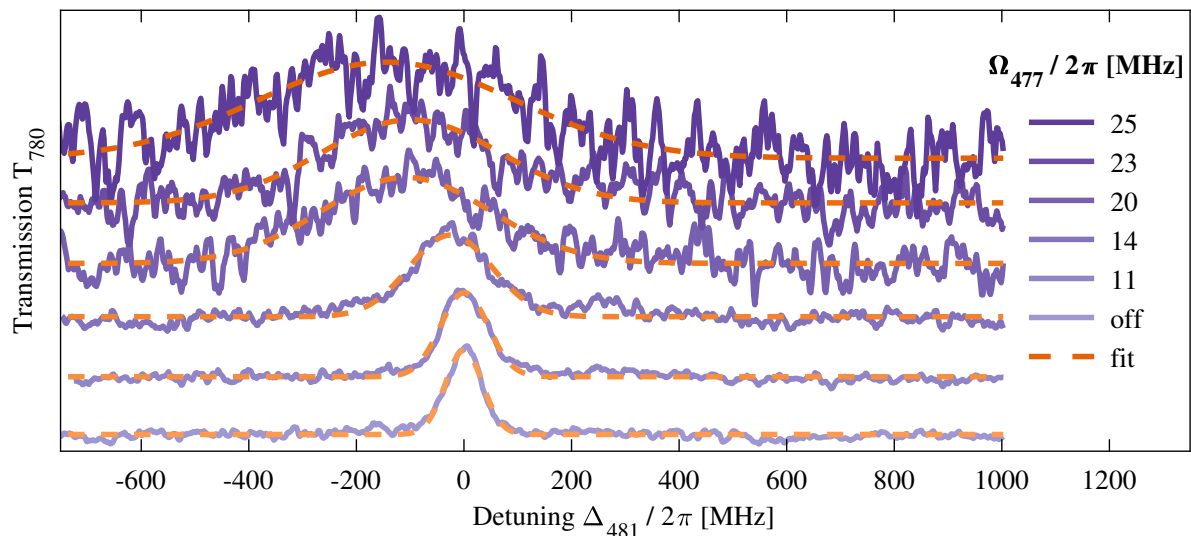


Figure 7.2: Rubidium measurements, EIT_{FP} . The signal is recorded at a fixed detuning $\Delta_{477}/2\pi = -35$ MHz, but with increasing Rabi frequency Ω_{477} . Each trace is normalized and offset for better comparability.

The excerpt of traces shows a significantly growing shift and broadening for increasing EIT_{OB} Rabi frequencies Ω_{477} . For this part of the thesis, we neglect the broadening in the discussion. In the next part, however, the broadening is considered, and turns out to be an integral part of the bistability mechanism. Note that the EIT_{FP} peaks are not asymmetrically deformed as is the case of the EIT_{OB} spectrum, where even a step appears

in the curve. The EIT_{FP} spectrum instead gives a *momentary* measure of the shift and broadening due to the effect of EIT_{OB} , equally for the whole spectrum of this probe. In contrast, the effect of EIT_{OB} onto *itself* induces a shift within the spectrum that is also depending on the current detuning position of the lasers, and therefore results in non-symmetric traces.

A full dataset of the interspecies interaction is captured by independently scanning both detunings Δ_{477} and Δ_{481} . We thereby obtain two-dimensional maps of the EIT_{FP} transmission signal, as shown in figs. 7.3 and 7.5. In the former, we chose a wider range of detunings Δ_{477} , to also address a second Rydberg resonance. At $\Delta_{477}/2\pi = 905$ MHz, resonance conditions for the two-photon transition via the second intermediate state of the ^{85}Rb isotope are fulfilled. This feature here is less prominent than that at zero detuning. Here, fewer atoms are available that match the correct velocity to compensate the splitting of -362 MHz between the hyperfine states $F' = 2$ and $F' = 3$ in the EIT_{OB} scheme, fig. 6.2. As a result, the effect on the probe scheme EIT_{FP} is weaker.

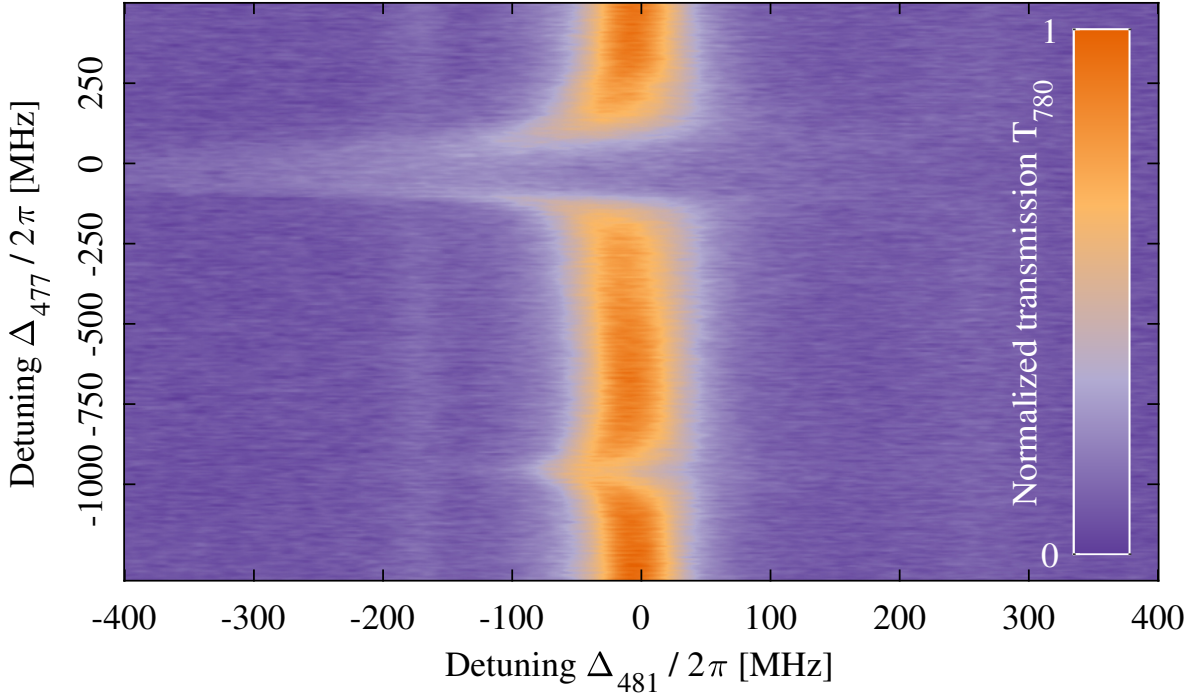


Figure 7.3: Rubidium measurements. One example of the two-dimensional maps showing EIT_{FP} probe transmission, obtained by independently scanning both detunings Δ_{477} and Δ_{481} . The Rabi frequency is $\Omega_{477}/2\pi = 20$ MHz. At approximately $\Delta_{477}/2\pi = -1$ GHz, a second resonance of the EIT_{OB} system is visible. We identify this feature as the second excitation path via the $5P_{1/2}$, $F' = 3$ intermediate state, which should appear at $\Delta_{477}/2\pi = -905$ MHz, due to the wavelength mismatch.

7.1.3 Exclusion of Rydberg-Rydberg interactions

For the discourse of the argumentation, let us first assume that Rydberg-Rydberg interactions (i.e., van-der-Waals type or dipole-dipole interactions) were the underlying mechanism for the optical bistability, and in particular that the observed shift has the sign of the interaction potential. Then, on the one hand, the interactions between 32S states should explain the appearance of the bistability itself. On the other hand, those between 41S and 32S are relevant for the shifts measured with EIT_{FP}. Figure 7.4(a,b) shows computed

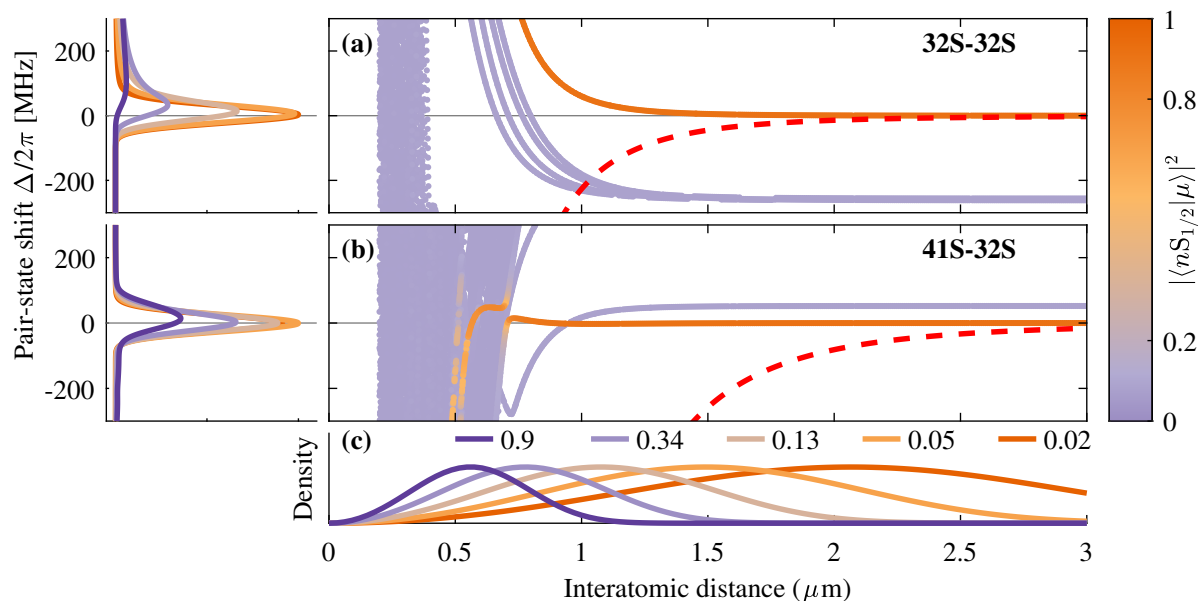


Figure 7.4: Rubidium Rydberg pair-states, calculated up to quadrupole-quadrupole interaction terms using [47]. (a) Pair potential of the interaction 32S – 32S. The color shading represents the projection on the unperturbed pair state. (b) Pair-states with 41S and 32S states, around 41S energy level. Avoided crossings with neighboring pair-states perturb the potential landscape. The Coulomb potential, C_4/r^4 , is plotted as the red dashed lines for the polarizability of 32S (a) and 41S (b). (c) Nearest neighbor distribution for densities from 0.02 to $0.9 \mu\text{m}^{-3}$, normalized to the maximum of each curve. The densities correspond to Rydberg fractions of 1 to 50%. On the left: Projection of the pair potentials (a,b), weighted by the Chandrasekhar distribution (c).

pair-potentials for the interaction of the rubidium 32S state with the 32S and 41S state, respectively. The potentials are calculated up to the order of quadrupole-quadrupole terms similar to those in reference [152], using the Alkali Rydberg Calculator software [47]. It is already noteworthy that between rubidium S states, the van-der-Waals interaction potential is continually repulsive, i.e., leading to a shift towards blue wavelengths, contrary to our observation.

A crude approximation for the pair-wise interaction in the ensemble of atoms can be calculated as follows. The nearest-neighbor distance probability in an ideal gas is given

by the Chandrasekhar distribution [153],

$$P_C(r) = \frac{3}{r_s} \left(\frac{r}{r_s}\right)^2 \exp\left\{-\left(r/r_s\right)^3\right\}, \quad (7.1)$$

where r_s is the Wigner-Seitz radius

$$r_s = \left(\frac{3}{4\pi\mathcal{N}}\right)^{1/3} \quad (7.2)$$

for particle density \mathcal{N} . This is plotted in fig. 7.4(c) for various densities of Rydberg atoms. We weight the pair-potential map with the nearest-neighbor distribution, and thus *project* it to the (vertical) detuning axis in fig. 7.4(a,b):

$$p(\Delta) = \sum_{\mu} \int_0^{\infty} dr P_C(r) \left| \langle nS_{1/2} | \mu \rangle \right|_{\langle \mu | H | \mu \rangle = \Delta}^2, \quad (7.3)$$

where the summation goes over all possible lines in the spectrum. Although this is a very coarse calculation and accounts only for binary interactions between nearest neighbors, it still gives a rough estimate of the expected tendency towards red or blue detuning. It is clear that only blue shifts are to be expected via this mechanism for the two states, 32S and 41S. The shifts even vanish completely for such dilute vapors as given by our experimental conditions. Solving the system of equations in sec. 1.7.2 for ρ_{Ryd} and integrating over the thermal ensemble provides an estimate for the density of Rydberg atoms in the EIT_{OB} system. When we assume the plain three-level system, with $\Gamma_{1,2}/2\pi = 6$ MHz, $\Gamma_{3,1}/2\pi = 1.5$ MHz, $T = 135$ °C, $\Omega_{795}/2\pi = 37$ MHz, and $\Omega_{477}/2\pi = 25$ MHz the maximum Rydberg density is on the order of $0.02 \mu\text{m}^{-3}$ ($\rho_{\text{Ryd}} = 0.016 \approx 2\%$) for the highest Rabi frequency, and even less for weaker excitation laser powers. Given this peak density value, the most probable distance to the next Rydberg atom is already more than $2 \mu\text{m}$, at which virtually no Rydberg-Rydberg interaction takes place for the 41S state.

Apart from these direct interactions paths, it could be conceivable that a significant part of the S state population decays to neighboring P states, e.g., by a superradiant decay [33]. Therefore, also the interaction between the states 32S and 31P, as well as between 41S and 31P are to be considered. The spatial integration of this dipole-dipole interaction averages to zero. In a related experiment with ultracold atoms [154], it was shown that this configuration does *not* lead to a shift of the excitation spectrum, and only a broadening was observed. Also, the 31P – 41S dipole-dipole interaction is much weaker than that of 31P – 32S, because the wave function overlap is smaller. This comes in contradiction with the experimental observations (shown in figs. 7.2 and 7.1) that the interaction shifts on the EIT_{FP} scheme are *larger* than the intrinsic EIT_{OB} shifts. It is therefore unlikely to explain the observed optical bistability by means of Rydberg-Rydberg interactions.

7.1.4 Ionization-induced electric fields

As an alternative explanation for the observed interaction shift towards red detunings, we show that the bistability is caused by charged particles that are a result of ionizing collisions of Rydberg atoms [35, 37, 38]. The interaction potential between a single charge and a Rydberg atom (indicated by the dashed red lines in fig. 7.4) in this picture arises from the dc Stark-shift of the Rydberg state and has the form C_4/r^4 , where C_4 is proportional to the polarizability α of the Rydberg state. Following the usual definition for the sign of the interaction, a positive polarizability value yields a negative energy shift. For rubidium S states, α is invariably positive [67], thus resulting in a red shift as observed. The polarizability for the regarded states are computed as $\alpha_{32S}/2\pi = 2.2 \text{ MHz}/(\text{V/cm})^2$ and $\alpha_{41S}/2\pi = 12.6 \text{ MHz}/(\text{V/cm})^2$, respectively. Examining figs. 7.1 and 7.2 again given these numbers, we find a good compatibility with both the sign and the rough magnitude of the observed shifts. Since both isotopes are probed in the same volume of the cell, they are exposed to the same electric field distribution. Hence, the EIT_{FP} spectrum would be shifted more according to the larger polarizability α_{41S} . This is exactly what we observe: The largest shift of EIT_{FP} is approximately $2\pi \times -150 \text{ MHz}$. Accordingly, the intrinsic shift of EIT_{OB} would amount to $2\pi \times -26 \text{ MHz}$. We find the edge position at about $2\pi \times -55 \text{ MHz}$, which seems to be reasonable given the width of these lines of roughly $2\pi \times 50 \text{ MHz}$.

To further substantiate our hypothesis, EIT_{FP} traces are systematically taken for a set of detunings Δ_{477} and various Rabi frequencies Ω_{477} in the EIT_{OB} scheme. The resulting data are displayed in fig. 7.5. Since this figure contains comprehensive information, let us examine this extensive figure step by step. For an exemplary Rabi frequency $\Omega_{477}/2\pi = 14 \text{ MHz}$, the resulting density plot of the transmission is shown in fig. 7.5(a), along with a sample of EIT_{FP} traces in fig. 7.5(b). This is similar to what is shown in fig. 7.2, where these traces are plotted for various Rabi frequencies Ω_{477} , but here, the detuning Δ_{477} is varied instead. This emphasizes the dependence of the EIT_{FP} signal on the excitation probability of 32S Rydberg atoms. We can gain further insight on the relation between the two systems by evaluating the shift in the EIT_{FP} system relative to the unperturbed line. For a set of Rabi frequencies Ω_{477} , this shift (determined by the center frequency of a Gaussian fit to the EIT_{FP} signal) is depicted in fig. 7.5(c) against the EIT_{OB} detuning Δ_{477} . These traces can be understood by following the vertical ridge in panel (a): There is a clear evolution from the unshifted EIT_{FP} signal in the off-resonant region to a maximally shifted signal, where the EIT_{OB} system is close to resonance. Noticeably, the shift trajectories in the EIT_{FP} spectra show the same characteristic deformation and subtle asymmetry towards red detuned frequencies as the transmission curves of EIT_{OB} in fig. 7.1. To conclude the analysis of the fig. 7.5, both the amplitude and the center frequency (again, Gaussian fits to each curve) of the shift trajectories from panel (c) are plotted versus the Rabi frequency Ω_{477} , fig. 7.5(d). The amplitude here directly reflects the shift in the

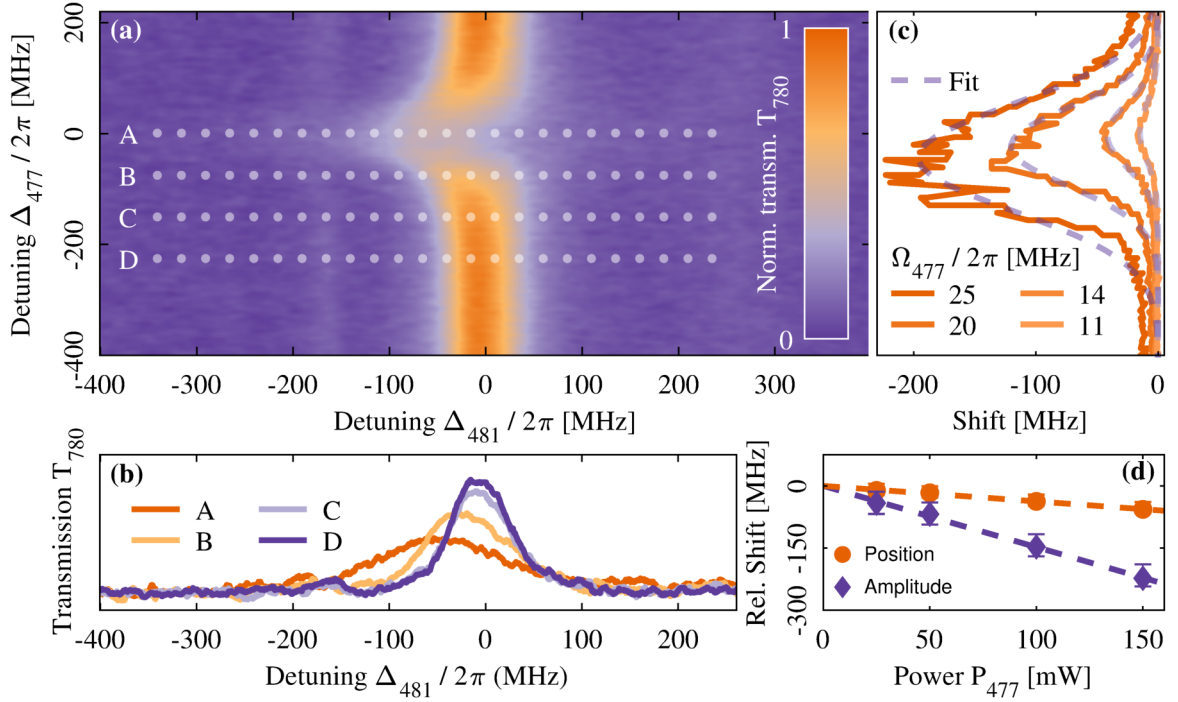


Figure 7.5: Rubidium measurements. (a) Another example of the two-dimensional maps showing EIT_{FP} probe transmission, obtained by independently scanning both detunings Δ_{477} and Δ_{481} , Rabi frequency $\Omega_{477}/2\pi = 14$ MHz. (b) Horizontal slices along the dotted lines in (a), corresponding to single EIT_{FP} measurements. (c) The maximum position in each horizontal slice in (a) as a function of the detuning Δ_{477} , for different Rabi frequencies Ω_{477} . (d) Center frequency and amplitude of the curves in panel (c), as a result of Gaussian fits. The center frequency (purple diamonds) represents the shift in the EIT_{OB} scheme, while the amplitude (orange circles) illustrates the shift of the EIT_{FP} scheme. Offsets are chosen such that the lines intersect at zero.

EIT_{FP} system, while the position is an indirect measure for the shift in the EIT_{OB} system. The ratio between the slopes of the two linear fits amounts to $(4 \pm 1) : 1$. A qualitatively similar observation was made by comparing the shifts shown in figs. 7.1 and 7.2, which again roughly reflects the ratio of polarizabilities between the states 41S and 32S which is 5.7:1.

7.1.5 Quantitative analysis

In order to do a quantitative comparison to previous experiments, we need a suitable measure, such as a cross-section. Hence, we first estimate the charge density present in the cell and then extrapolate to a cross-section that would be necessary for an ionization process to explain these densities. In a very simplified picture, neglecting the free electrons and only considering the ions, the electric field distribution in the medium is described by the Holtmark distribution, cf. sec. 3.2. An estimate of the mean ion density \mathcal{N}_{ion} is

now found by comparing this model with the measured data as follows. The line shape of the measured EIT_{FP} signal $S(\Delta_{481})$, (plotted in fig. 7.6) amounts to a convolution of the Holtzmark probability distribution with the EIT-signal shape $L_\Gamma(\Delta_{481})$, as introduced in eq. (3.37). In this integral, the EIT-line (for example a $2\pi \times 50$ MHz wide Lorentzian profile [50]) is displaced by $-\alpha E^2/2$ according to the Stark shift. By fitting the exponents and coefficients, we find that the center C of the obtained line shape—determined by a Gaussian fit [155]—scales with the ion density and the polarizability as

$$C \approx -2 \times 10^{-13} \text{ V}^2 \text{ cm}^2 \cdot \alpha \cdot \mathcal{N}_{\text{ion}}^{4/3}. \quad (7.4)$$

This can be translated to a first estimate of the observed ion density in the vapor of up to $\mathcal{N}_{\text{ion}} \approx 3 \times 10^{10} \text{ cm}^{-3}$ for a measured shift of up to $2\pi \times 250$ MHz in the EIT_{FP} scheme. Given the atomic ground state density of the ^{85}Rb isotope of $1.8 \times 10^{12} \text{ cm}^{-3}$ and the estimated maximum Rydberg fraction of around 2% as before, this ion density roughly matches the Rydberg density in quantity. This order of magnitude is conceivable, since the natural decay of Rydberg atoms would be anyways dominated by the transit time effect. If the ionization rate is significantly faster than that, the majority of Rydberg atoms will be ionized before propagating out of the excitation volume. The distribution of the nearest-neighbor distance probability for this density has a maximum at $r = 1.7 \mu\text{m}$. The shifted signal for such reasonable range of ion densities is illustrated in fig. 7.6.

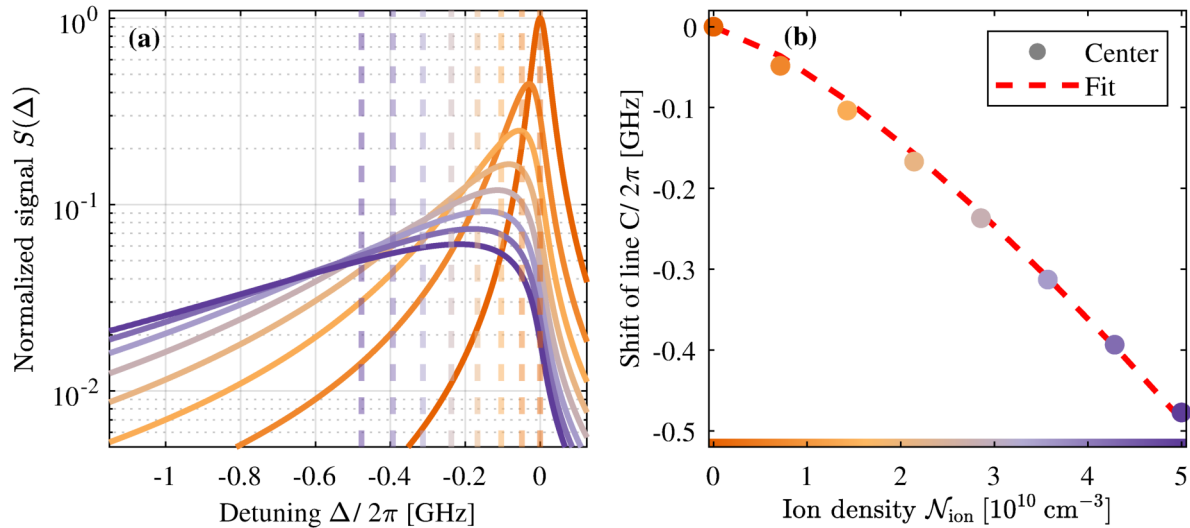


Figure 7.6: Convolution of the Holtzmark distribution function with the quadratic Stark shift. Example calculation for a Lorentzian lineshape ($\Gamma/2\pi = 50$ MHz) and a polarizability $\alpha/2\pi = 12.6 \text{ MHz}/(\text{V}/\text{cm})^2$. Dashed vertical lines are the center of Gaussian fits. The colors in the left panel indicate the charge density according to the abscissa in the right panel. The fit function in the right panel follows eq. (7.4). Due to the very rough nature of this approximation, and determination of the center of an asymmetric line shape, we refrain from error estimates, which are dominantly systematic.

As a second step in the quantitative analysis, we approximate the ionization process with a rate equation. Rydberg atoms with a number density \mathcal{N}_{Ryd} (which is assumed to be a constant source, unaffected by ionization) collide with ground state atoms with a relative velocity v and a cross-section σ , contributing to the increase of the density of ions \mathcal{N}_{ion} . At the same time, ions leave the excitation volume with a rate of $\gamma = 1.5$ MHz, chosen to be the inverse of the transit time radially along the excitation volume [156]. The corresponding rate equation is

$$\dot{\mathcal{N}}_{\text{ion}} = \mathcal{N}_{\text{Ryd}} \times (\mathcal{N}_{85} + \mathcal{N}_{87}) \sigma v - \gamma \mathcal{N}_{\text{ion}}, \quad (7.5)$$

and reaches its steady state at

$$\mathcal{N}_{\text{ion}} = \mathcal{N}_{\text{Ryd}} \frac{(\mathcal{N}_{85} + \mathcal{N}_{87}) \sigma v}{\gamma}. \quad (7.6)$$

Substituting the ion density with the value from the first estimate leads to an ionization cross-section of up to $\sigma = 1.15 \times 10^{-7} \text{ cm}^2 = 0.18 \cdot \sigma_{\text{geo}}$, while the geometric cross-section of the 32S Rydberg atom, eq. (2.31), is given by $\sigma_{\text{geo}} = 6.1 \times 10^{-7} \text{ cm}^2$. Similar measurements in a pulsed experiment with an atomic beam showed $\sigma = 0.06 \times \sigma_{\text{geo}}$ [35]. Note that our result is slightly larger than the reference value. We attribute this to the additional ionization channel due to electron collisions, as is introduced in the next part of the thesis.

7.1.6 Experimental cross-talk

The two laser-atom systems, EIT_{FP} and EIT_{OB}, are chosen such that the spectroscopy on each of the rubidium isotopes should be considered to be independent of the other—except for the electric field due to ionization. Figure 7.7 however does show an unexpected experimental cross-talk from EIT_{FP} to the bistable EIT_{OB}: on each resonance of the two-photon transition, the transmission signal of the probe system, T₇₈₀, shows the characteristic EIT transmission features. Simultaneous to these narrow spikes, the EIT_{OB} system apparently undergoes the phase transition, stimulated by the additional Rydberg atoms in the 41S state available for ionization. When the EIT_{FP} system is out of resonance again, the temporary increase in background vanishes; the system relaxes again to the low population state.

This *reverse* cross-talk is in accordance with the charge-induced hypothesis: by supplying additional Rydberg atoms of a higher lying state to the system, the phase transition of EIT_{OB} for the lower lying state can be triggered earlier. At the short periods of resonance of the EIT_{FP} scheme, these required additional ionization candidates are available. Of course Rydberg atoms of both isotopes are subject to ionizing collisions.

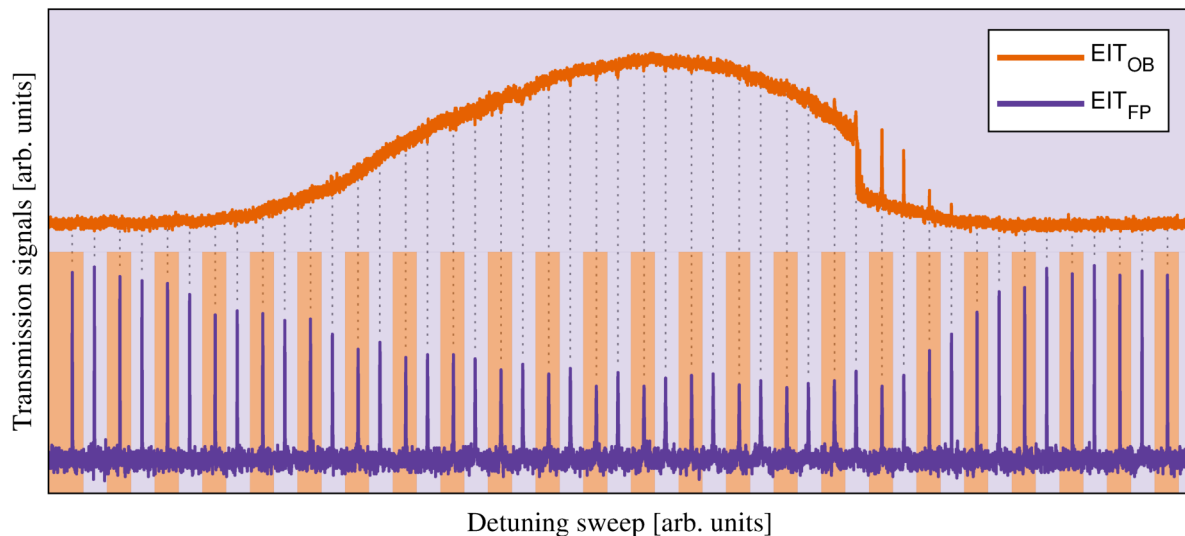


Figure 7.7: Rubidium measurements. Experimental cross talk between EIT_{FP} and EIT_{OB}. Displayed are the transmission signals (T_{795} in orange, T_{780} in purple) for one slow sweep of Δ_{477} across the feature. The acquisition duration for this trace is ≈ 50 s. Simultaneously, Δ_{488} of the probe system is swept back and forth ≈ 25 times, as indicated by the orange and purple background. Coincidentally with the narrow EIT features of the EIT_{FP} system, the transmission signal of EIT_{OB} shows the same spikes. The additional Rydberg atoms in the 41S state are also ionized, and contribute to the phase jump of EIT_{OB}.

7.2 Cesium spectroscopy

7.2.1 Manipulating the sign of the interaction

Further evidence that the optical bistability is caused by electric fields is found by analyzing the position of the bistability window relative to the unperturbed resonance. This gives the sign of the underlying interaction mechanism. Figures 7.8(a) and 7.8(b) show our hysteresis spectra with optical bistability for the 23D and 28S state in ^{133}Cs . For both states, the character of the Rydberg-Rydberg interactions is essentially repulsive [15, 91]. However, the polarizability clearly changes its sign from $\alpha_{23D} = 0.52 \text{ MHz}/(\text{V}/\text{cm})^2$ to $\alpha_{28S} = -0.76 \text{ MHz}/(\text{V}/\text{cm})^2$, as does the position of the bistable region. We summarize these results as well as those from previous measurements in tab. 7.1. When comparing the respective observation to the polarizability of each species and angular momentum states, we find perfect agreement with our hypothesis.

7.2.2 Electric field modulation

Finally, we investigate how the optical bistability is affected by external electric fields. Figure 7.8(c) shows a significant increase in the width of the hysteresis as the frequency

Element	State	E_{vdW}	E_{Stark}	Bistability	Source
Rb	$32S_{1/2}$	+	-	-	fig. 7.1
Rb	$41S_{1/2}$	+	-	-	fig. 7.2
Cs	$23D_{3/2}$	-	+	+	fig. 7.8(a)
Cs	$28S_{1/2}$	+	-	-	fig. 7.8(b)
Cs	18 - 37 $P_{3/2}$	(+)	-	-	[32, 139]

Table 7.1: Compiled signs of Stark shift, van-der-Waals interaction and the actually observed position of the bistability edge. The vdW energy of the cesium P states is essentially repulsive [15, 91]. Interactions are calculated for $|m_J| = 1/2$ and for zero angle.

of the electric field is increased. The applied electric field amplitudes are small enough that the resulting Stark-shift and the modulation frequency are negligible with regard to the relevant energy scales of the Rydberg atoms. The interparticle interactions of neutral particles is therefore not affected. However, charged particles are heavily influenced. In the range of frequencies used for the electric field modulation (10 to 500 MHz), the free electrons from the ionization process are accelerated and perform an oscillating trajectory, thus increasing the ionization rate by additional collisions. We believe that this explains why the width of the bistability region increases. Overall, the susceptibility to electric field modulation contradicts a dipole-dipole interaction between Rydberg atoms and once more designates that ionization significantly contributes to the observed bistability.

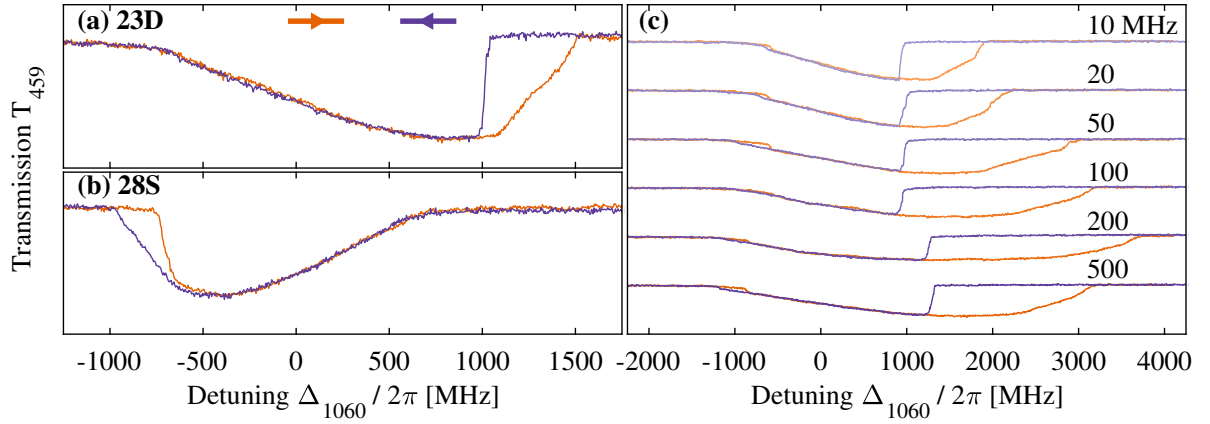


Figure 7.8: Cesium measurements. (a,b) Comparison between the $23D$ and $28S$ state, with opposite signs of the polarizability. (c) Effect on the signal shape for the $23D$ state by RF modulation with a sine wave of 3.2 V cm^{-1} amplitude. The frequency of the injected RF wave increases from top to bottom, as indicated above each curve. The traces are offset for better comparability.

8 Part II: Conclusion

In this part of the thesis, we have established a strong link between the phenomenon of optical bistability in thermal Rydberg vapors and the presence of charged particles in the gas. We have excluded that dipole-dipole and van-der-Waals interactions are the origin of the interaction shift inherent to the bistability. With the consolidated investigation of measurements with two independent atomic species and the variation of principal and azimuthal quantum numbers we are able to deter Rydberg-Rydberg interactions as the dominant mechanism responsible for the interaction shift that causes the non-linear behavior. At the same time, we find strong evidence that electric fields produced by charges originating from Rydberg ionization are the leading contribution to the observed effect. Our argumentation based on the results of two different experimental setups contradicts the previously suggested explanations with dipolar interactions published in Ref. [32, 138, 139], where the spectrum of experimental parameters overlaps with our settings.

In the first experiment presented in this part, we have applied two independent EIT schemes, each addressing only one of the naturally abundant isotopes in a rubidium vapor cell. The first scheme strongly drives the transition in ^{85}Rb , enabling the atoms to enter the bistable regime. Simultaneously, the effect on the ^{87}Rb atoms is monitored by the second EIT scheme. The choice of Rydberg states allows us to exclude dipole-dipole interactions. We find both a deformation of the EIT_{OB} line and a shift of the EIT_{FP} line to the red. These observations are in good quantitative agreement with a Stark effect caused by electric fields. The fields originate from ionizing collisions of the Rydberg atoms, and the estimated ion densities and the required ionization cross-sections are within a sensible range. In the second experiment using ^{133}Cs vapor, we have demonstrated that externally applying weak electric fields significantly alters the width and position of the bistability. Only charged particles being affected by such weak fields and the distinct accordance of the sign of the polarizability for different states finally support our conclusion.

Part III

Characterization of the Plasma and the Bistability

9 Part III: Introduction

In the previous part, we have successfully established a connection between charged particles and the emergence of optical bistability involving Rydberg atoms in thermal vapors. Since the main ingredients in a plasma are also—of course—charged particles, this raises the question, if and what plasma characteristics the vapor of electrons and ions shows.

In this part of the thesis, we demonstrate further analysis of the emergence of optical bistability. We also directly measure the plasma frequency, and thereby show that the origin of the bistable behavior lies in the creation of a plasma that is formed by ionized Rydberg atoms. The recombination of ions and electrons creates a certain fluorescence signature, which allows us to characterize the plasma properties of the vapor. Studying the transient dynamics of the hysteresis that occurs, we also determine a scaling parameter for the point of plasma formation.

This part of the thesis is based on the experiments and findings that were worked into the manuscript *Interplay between thermal Rydberg gases and plasmas*, which has been published as a research article in *Physical Review A* in 2019 [157].

10 Setup and methods

10.1 Experimental setup

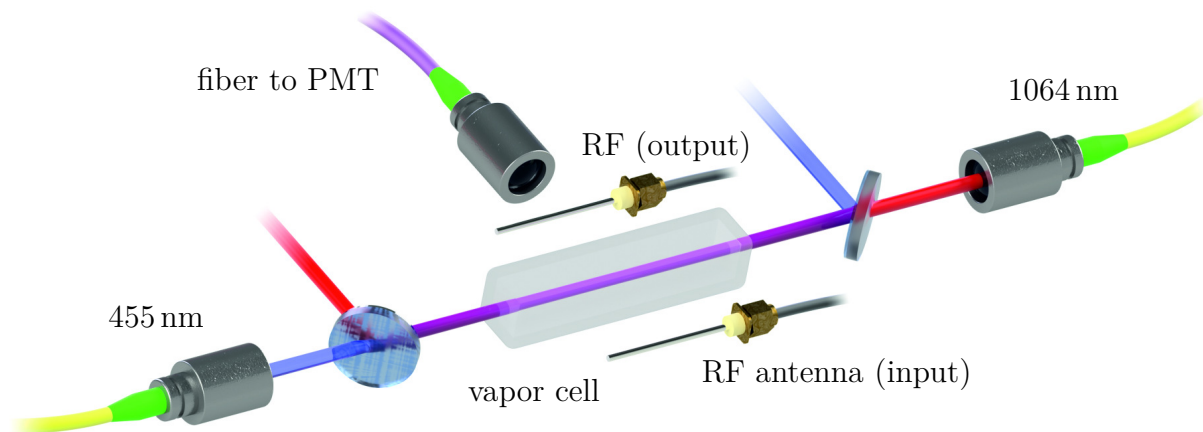


Figure 10.1: Experimental setup for the plasma characterization. Two counter propagating laser beams excite the Cs atoms in a vapor cell to a Rydberg state. The atomic fluorescence is captured with a fiber, bandpass-filtered and detected on a PMT. The change in the radio-frequency transmission through the atomic sample is measured with the dipole antennas.

Figure 10.1 shows the experimental setup for the further investigation of the bistability and the analysis of the plasma. The setup is again straightforward, as is usual for hot atom experiments: A vapor cell containing a macroscopic droplet of cesium is placed in the path of two counter propagating, collimated laser beams. Each beam has a $1/e^2$ radius of 0.7 mm. The vapor cell has a squared cross-section with a side length of 1 cm, and a length in the direction along the beam of 5 cm. The bulk of the cesium resides in a reservoir attached to the bottom of the vapor cell. The temperature of the reservoir is stabilized in order to provide a controlled atomic density of the vapor. The main body of the vapor cell is held at higher temperatures than the reservoir to prevent alkali condensation on the windows. We determine the cesium atomic density before and after each measurement, by recording and fitting the absorption profile of the whole cesium D_2 spectrum. This well-established method is performed in analogy to the procedure described in [148]. The densities used for the experiments described in this part of the thesis are varied from 0.05 to $7 \times 10^{12}/\text{cm}^3$, which corresponds to a reservoir temperature of 25 up to 87°C. In terms of inter-particle distances, this translates to a separation of 0.3 to 1.7 μm between neighboring cesium atoms.

We excite cesium atoms to the $nD_{5/2}$ Rydberg state, again making use of the inverted wavelength two-photon scheme [60], as is depicted in fig. 10.2. In particular, we address the Rydberg state $30D_{5/2}$ in one part of the experiment, and work with the state $42D_{5/2}$ in another. As in the previous part of this thesis, the first laser is a frequency-stabilized,

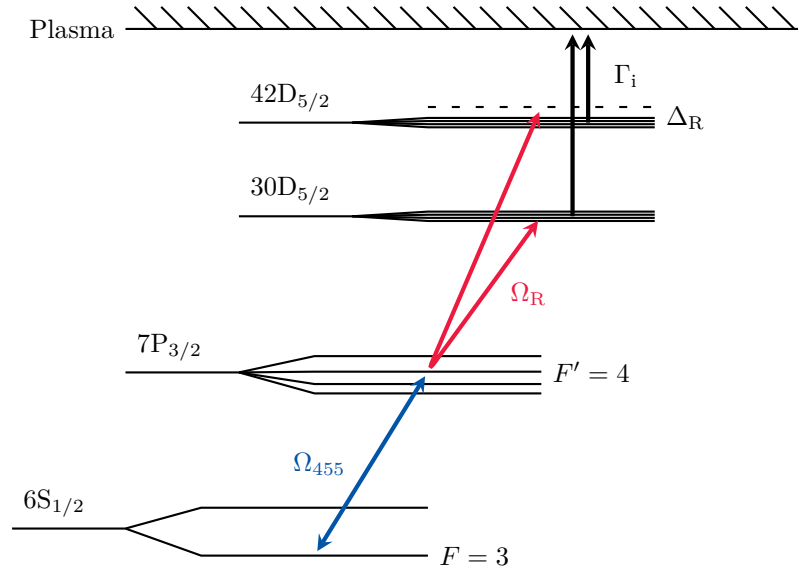


Figure 10.2: Three-level diagram of the inverted wavelength ladder scheme applied in this part of the thesis. The two lasers excite Cs atoms to the intermediate $7P_{3/2}$, and subsequently up to an nD Rydberg state. For measurements with $n = 30$, the Rydberg laser is locked on resonance, while for $n = 42$, the laser is scanned with detuning Δ_R . The additional plasma state is populated at a rate Γ_i due to ionizing collisions of the Rydberg atoms in the vapor.

frequency doubled diode laser, although this time tuned to the cesium $6S_{1/2}, F = 3 \rightarrow 7P_{3/2}, F' = 4$ transition at a wavelength of about 455 nm. This laser is referred to as the *blue* laser, and is associated with variables and parameters with the subscript B. Rabi frequencies, $\Omega_B/2\pi$, used for the experiments range between 1 MHz and 12 MHz. The 455-nm-laser is locked with a separate cesium reference cell via dichroic atomic vapor spectroscopy [158]. The second laser (the fiber-amplified infrared diode laser) excites the atoms from the $7P_{3/2}$ intermediate state to the Rydberg state. Variables and parameters associated with this transition are subscript with the letter R. Rabi frequencies, $\Omega_R/2\pi$, are varied between 3 MHz and 90 MHz. The laser is either scanned over the cesium $7P_{3/2} \rightarrow nD_{5/2}$ transition with a detuning Δ_R (measurements with $n = 42$, laser wavelength $\lambda_{42D} = 1064.98$ nm) or locked on resonance ($n = 30$, $\lambda_{30D} = 1073.50$ nm). We make use of another cesium vapor cell as reference, where we apply the conventional, weak-probe EIT scheme [50]. For this light field, we used side-of-fringe locking to the reference signal in order to stabilize the laser frequency [159]. The laser detunings in case of the scanned measurements are calibrated using a Fabry-Pérot interferometer with a free-spectral range of $\Delta\nu_{\text{FSR}}/2\pi = 1.5$ GHz, in combination with the EIT reference signal.

Typically, a thermal vapor cell is completely wrapped in thermally isolating material. By allowing only the transmitting laser beams to pass through in- and output apertures as small as possible, optimal temperature control is achieved. For the measurements presented in this part of the thesis, we have designed the temperature stabilizing oven with the necessary optical and electromagnetic access to the vapor cell in mind. The sides of our structure are made of thin glass plates (spanning an area of $6\text{ cm} \times 6\text{ cm}$), allowing fluorescence and RF signals to pass through.

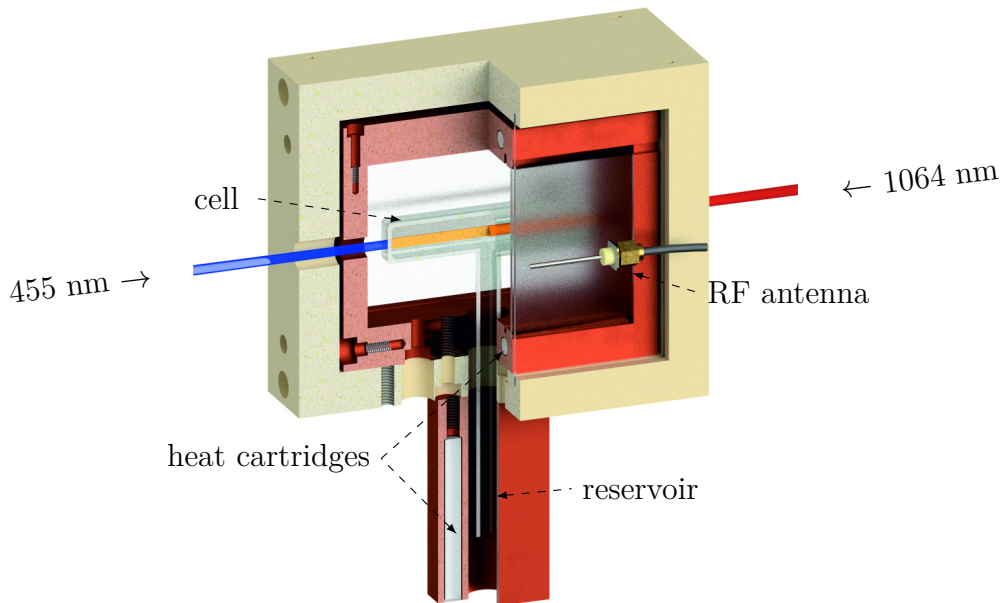


Figure 10.3: Sectional view of the design for the temperature-stabilizing oven, with optical access perpendicular to the laser beams and the possibility to radiate RF frequency into or through the plasma. The second antenna to receive the signal is on the back-side of the oven. The copper parts (brown elements) are heated with resistive wire cartridges, and wrapped by an insulating layer of a polyether ether ketone (TEKAPEEK). The side-windows are each made of two layers of glass. The reservoir points down into a block that has a separately controlled temperature, to define the vapor density.

10.2 Fluorescence measurements

Compared to the typical EIT spectroscopy measurement protocol, the Rabi frequencies applied in our experiments are beyond the weak probe regime. Due to the high laser powers involved, measured changes in the transmission of either light field would suffer from a large background signal. Even small relative fluctuations on this background are large compared to the signal height; an extremely high dynamic range of the oscilloscope is required to capture the signal. As an alternative measure, we detect the fluorescence emitted from the atomic ensemble in the direction perpendicular to the excitation lasers

using a photo multiplier tube (PMT). This has the benefit of being a quasi background-free measurement, and also spacial resolution along the beam axis is possible.

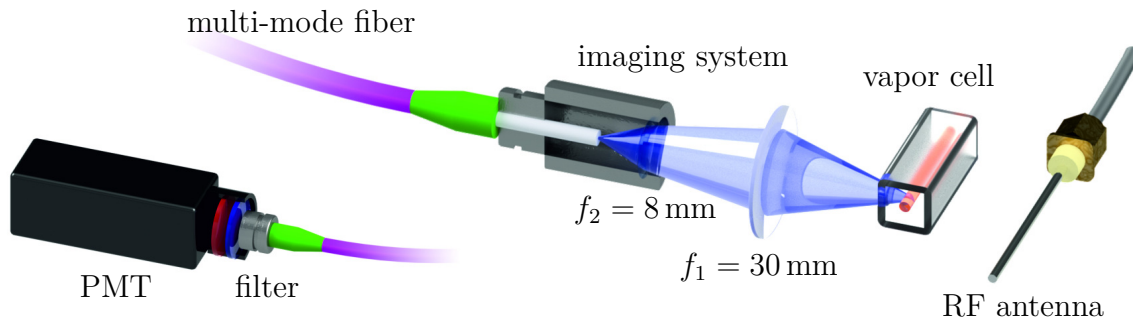


Figure 10.4: Schematic of the assembly collecting fluorescence from within the cell. The light from a spot of $\approx 1.5\text{ mm}$ diameter is projected onto a multi-mode fiber with an imaging system consisting of two lenses. Long and short-pass filters transmit light between 500 to 800 nm, which is then either analyzed with a photo multiplier tube, or dispersed in a spectrometer.

A detailed scheme of the detection setup is shown in fig. 10.4. The fluorescence is collected by an imaging system consisting of two lenses with focal lengths of $f_1 = 30\text{ mm}$ and $f_2 = 8\text{ mm}$. The second lens focuses the light into a multi-mode fiber, $400\text{ }\mu\text{m}$ core diameter. The fluorescence is imaged on to the fiber facet from within the excitation laser beam path, which is about 45 mm in front of the first lens. The diameter of the spot from which photons are collected is approximately 1.5 mm, which roughly reflects the cross-section of the laser beams. We filter the fluorescence with long- and short-pass filters¹ so that only light between 500 to 800 nm is collected. With this interval, we exclude the 455-nm laser light, and the strongly fluorescing decay via the D_2 line at 852 nm that can already occur with the 455-nm excitation on its own. Overall, we estimate that the collection efficiency is on the order of the $(0.1 \pm 0.1)\%$ level of the photons emitted into all directions from that spot.

The setup also allows us to directly image the cell from the side using a camera in combination with an objective². We further have the option to feed the optical fiber into a spectrometer³, to determine the spectral composition of the fluorescence.

10.3 RF-injection and transmission measurements

Complementary to the fluorescence measurements, we can not only inject but also measure the transmission of radio-frequency fields. The RF field is coupled into the vapor cell with

¹Thorlabs, FELH0500 and FESH0800

²Thorlabs DCC1545M, MVL16M1

³Andor Shamrock SR-303i-B-9FT with iDus DU401A-BR-DD

an approximately 4 cm-long dipole antenna that is oriented parallel to the laser beam direction through the cell. A second, identical antenna at the opposite side of the vapor cell picks up the signal, that, due to only minute changes on both phase and amplitude of the RF wave, requires careful processing: In order to improve the signal-to-noise ratio to a level such that a signal is usefully measurable, we modulate the radio-frequency amplitude as well as the laser intensity and make use of two steps of lock-in amplification. Since the crude design of the antennas does by no means provide an impedance matched environment for the RF field, also quadrature detection in order to eliminate the effect of an unknown phase of the detected signals is necessary. Measuring the *in-phase* and *quadrature* components of the transmitted RF field, I and Q , and two stages of lock-in demodulation, a total of four lock-in amplifiers is necessary. A schematic of the electronic circuitry is shown in fig. 10.5.

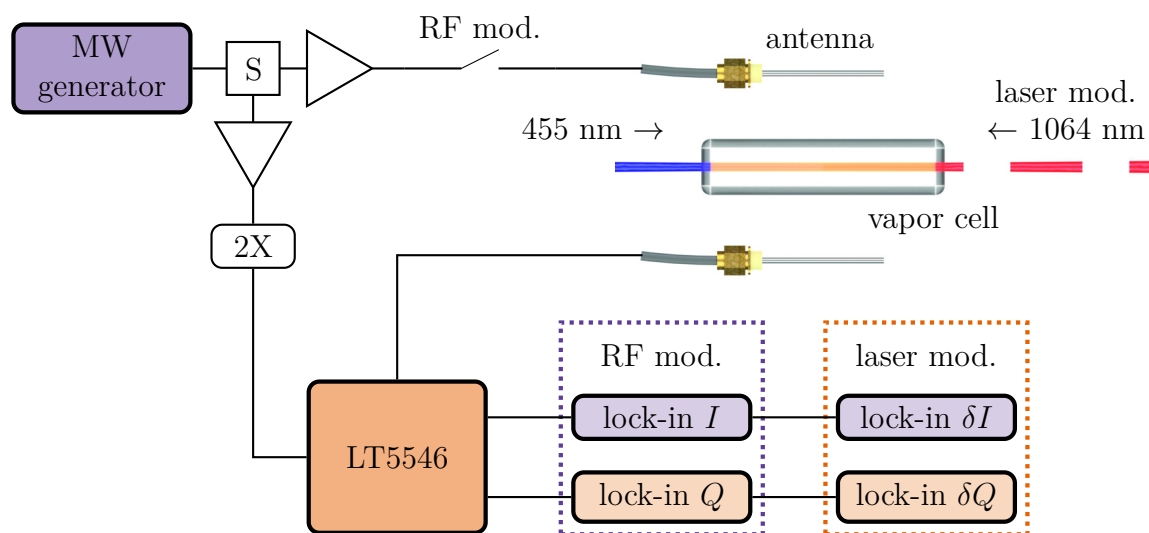


Figure 10.5: Circuit for the RF transmission measurements, based on the I/Q demodulator chip LT5546. The output of the RF-generator is split (buffered by amplifiers): one arm feeds the 2XLO input of the detector chip, the second arm is modulated via an electronic switch and coupled into the antenna. A second antenna feeds the received signal into the detector chip, where it is down-converted to Q and I components. The output of the LT5546 is fed into the two lock-in amplifier stages.

As the detector, we used a commercially available integrated quadrature demodulator from Linear Technology, the integrated circuit LT5546. The chip is a monolithic I/Q demodulator for signals between 40 MHz to 500 MHz. It provides the quadrature down-conversion to I and Q baseband signals. The output of the chip is fed into the first lock-in amplifier stage (all four lock-in amplifiers are from Femto, LIA-MV-200-H), which demodulates the quadrature and in-phase components. Note that lock-in amplifiers could also provide Q and I components of a single signal with respect to the modulation phase. Here we refer to the two output channels of the LT5546 chip, and measure these with a suitable phase delay only with the in-phase channel of the lock-ins. The RF wave

is switched on and off at a rate of 59 742.71 Hz and integrated with a time constant of 0.3 ms, i.e., 18 periods of modulation. The output of the two separate lock-in amplifiers is then again used at the input of the second, identical lock-in stage, that demodulates the changes in I and Q , for which the Rydberg laser is modulated with a chopping wheel at 100 Hz. As a result, the output ports yield the two signals, δ_I and δ_Q . As an observable that quantifies the *change in transmission*, which is merely a complex transfer function than just absorption, we define

$$\delta T_{\text{RF}} = \sqrt{\delta_Q^2 + \delta_I^2}. \quad (10.1)$$

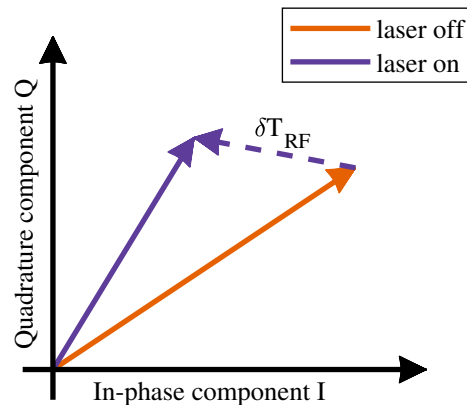


Figure 10.6: Change in the quadrature and in-phase components of the two lock-in stages. The combined change in both phase and amplitude is reflected in the *change in transmission*, δT_{RF} , as defined in eq. (10.1).

The quantity δT_{RF} has to be interpreted as the overall change of the transmission signal in both phase and amplitude combined. Distinguishing between the two requires additional knowledge and stability of the phase information, which is both difficult to obtain. Partly, because it is buried in noise, and partly, because impedance fluctuations caused by subtle changes to the experimental conditions, such as the experimenter wandering around the room during data acquisition, already impact on the phase. With this definition, phase drifts during averaging are (at least partially) equalized. A schematic of the RF transmission signal as captured with our measurement protocol is shown in fig. 10.6.

11 Results and discussion

11.1 Bistability mechanism

In previous work on optical bistability in thermal Rydberg vapor [32, 139, 160], the authors assumed that Rydberg atom interactions give rise to the mechanism that is responsible for the phenomenon. The effect that charges have on the system was not incorporated into the models used to explain the observed behavior. The first experimental part in this thesis associates the bistability with the presence of ions. There, we are able to provide a plausible quantitative assessment of the required densities of Rydberg atoms and charges as well as an ionization cross-sections in consent with literature values. However, a thorough understanding remained yet to be developed. Our experiments with access to the fluorescence emission transverse to the laser beam propagation direction allows a new perspective onto the subject. The spatially resolved fluorescence signal gives insight on the emergence of the bistability itself.

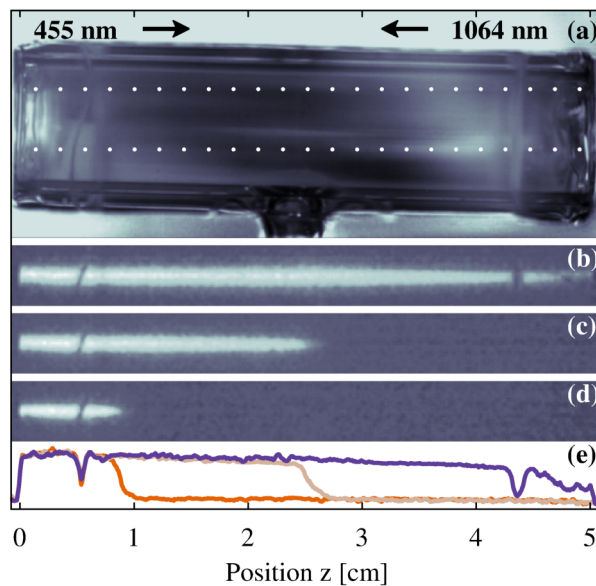


Figure 11.1: (a) Side-view of the cell. The lasers propagate between the dotted lines, 455 nm laser from left to right, 1064 nm laser from right to left. (b-d) Fluorescence signal filtered for wavelengths between 500 and 800 nm. By carefully tuning the laser parameters the spatial position of the phase transition along the beam can be controlled. The fluorescing ray resembles a lightsaber [161] (e) Pixel values along the center of the three beams. The background with the Rydberg laser switched off was subtracted. The two defects on the left and right hand side are due to quartz sublimate on the surface of the cell.

Figure 11.1 shows an actual photograph of our cell as viewed from the side. The beams travel horizontally through the cell, and, given suitable combination of density, laser power, and detuning, create a fluorescing ray (fig. 11.1(c-d)), consistent with the spectra reported in [32]. As the 1064-nm laser is scanned back and forth across the Rydberg resonance position, fluorescence suddenly appears to streak across the whole vapor cell for one scan direction, but then gradually retracts towards the entrance window of the blue laser beam until it completely vanishes for the opposite scan direction. The directionality of the phenomenon was verified to depend on the overall sign of the polarizability by addressing different Rydberg states, as in part II. This *lightsaber*-like phenomenon [161] that has a distinct transition between a light and a dark side along the beam repeats for every cycle of the detuning scan. When filtering out the 455-nm light (e.g., with suitable laser safety goggles), the effect is even visible by eye. This is a visual manifestation of the optical bistability.

The probe signal of the blue light field, measured as the transmission through the vapor with a photo-diode the same way as in the previous part of this thesis, hereby coincides with the temporal progress of the fluorescence, fig. 11.2. The sharp kink in the plot coincides with the sudden streaking of the fluorescing beam through the cell. For the reverse scan direction, the gradual retraction of the *lightsaber* is correlated with the decrease of blue laser transmission. For the remaining spectrum, the fluorescence brightness and transmitted power evolve completely in sync. Since apparently, the lateral fluorescence and the transmitted probe light are interchangeable, we do not record the probe transmission any further. Especially varying the blue Rabi frequency and the density of the vapor requires careful reconfiguration of this absorption measurement. Very frequently, the signal coming from the photo-diode gets saturated, or needs stronger amplification and vastly different offset voltage in order to obtain usable data. Recording the fluorescence signal from the side using a photo multiplier tube lets us focus better on the relevant aspects of the experiments.

Due to these observations of the fluorescence dynamics, we modify the overall concept for the occurrence of the hysteresis as is depicted in fig. 10.2. As evidenced before, charges play the essential role in the optical bistability that takes place in thermal Rydberg gases. In fact, it is not Rydberg-Rydberg interactions that mediate the optical bistability, but a plasma of ions and electrons which are created at suitable Rydberg densities. With the new measurements presented in this part of the thesis, we demonstrate that not only in the typical optical bistability experiments but over a much wider range of experimental parameters, a weakly coupled plasma exists in the vapor. It is due to the sudden switching to the plasma state via a nonlinear ionization process and the feedback due to the Stark shift in an electric field distribution that leads to the observation of the hysteresis, and motivates the term optical bistability.

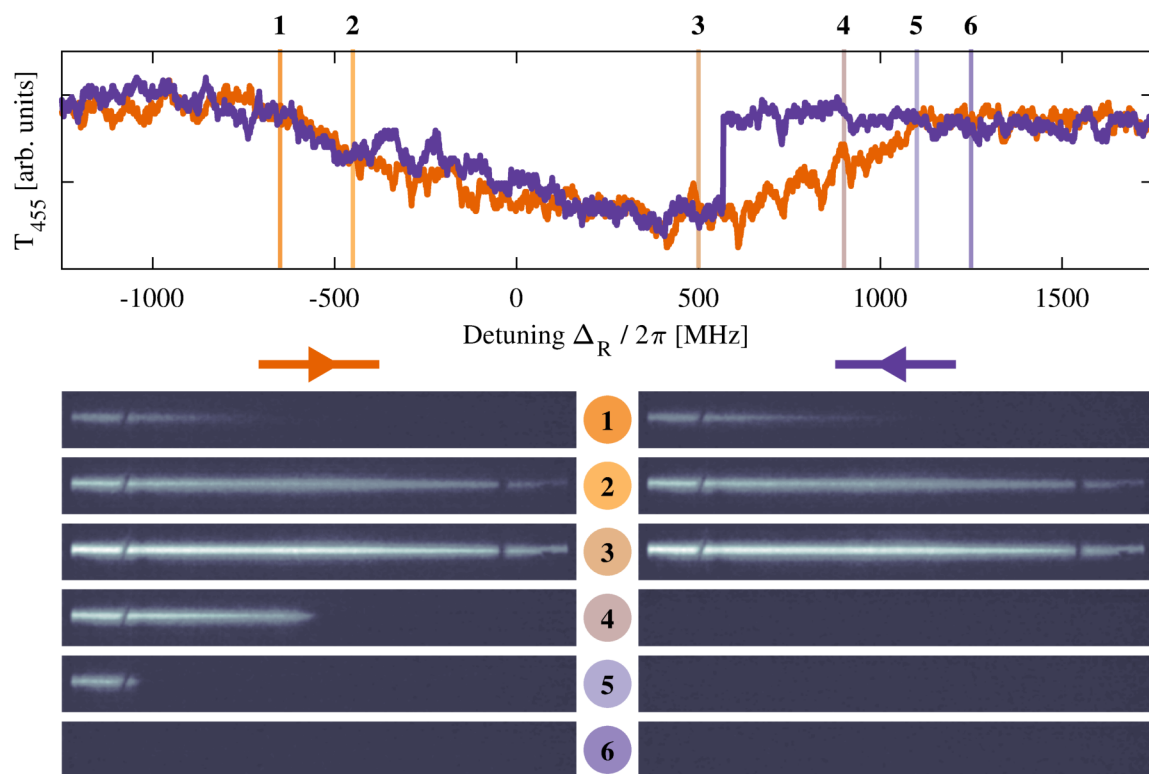


Figure 11.2: Transmission signal and synchronized fluorescence images of the cell from the side. The behavior of the probe beam, T_{455} , coincides with the glowing beam along the laser axis. For a negative detuning (1), the fluorescence is very dim, and even appears not to extend across the cell due to absorption of the 455-nm laser from left to right. The transition from light to dark is smooth. Approaching the center of the peak (2), fluorescence gets continually stronger. It stays at high brightness until shortly before the phase transition. Within the hysteresis window, the previous state of the system is of relevance: Coming from negative detuning (3,4,5,6, orange curve), the beam gradually retracts until completely vanished. For the opposite scan direction (6,5,4,3, purple), it is all dark until the beam suddenly flashes across the cell.

We propose two mechanisms that contribute subsequently, and explain the transition to a plasma. First, Rydberg atoms collide with ground state atoms, thereby creating a background-level of ions and free electrons. Then, these electrons collide with other Rydberg atoms, giving rise to a much higher rate of ionization Γ_i . Because electrons are so lightweight, their velocity is by orders of magnitude higher than that of the heavy alkali atoms. Thus, the collision rate is accordingly large. Only once a critical density of charges exist via the first mechanism, the second process takes over in a much more efficient way. Overall, this is a well known effect, and commonly described as the *avalanche process* [35, 83, 162].

The plasma plays a fundamental role in the atomic dynamics, and thus the bistability mechanism. With charges present in the gas, the Rydberg energy levels are shifted due to

the Stark shift, Δ_S . As thermal atoms move through the electric field distribution and also ions and electrons are continuously reshuffled, the Rydberg energy levels rapidly change during the atom-light interaction. Therefore, an additional dephasing γ_S on the Rydberg coherences needs to be taken into account which changes the excitation dynamics of the driven system. On average, this variation affects each atom of the ensemble more or less equally, although the individual course of shifts might differ. To be able to describe it with a Lindblad operator later, we assume this dephasing to be a homogeneous effect. In a dilute plasma, the ion density dictates the electric field distribution, while the electron vapor disturbs the coherences directly by collisions. This is usually referred to as the impact approximation [128, 163].

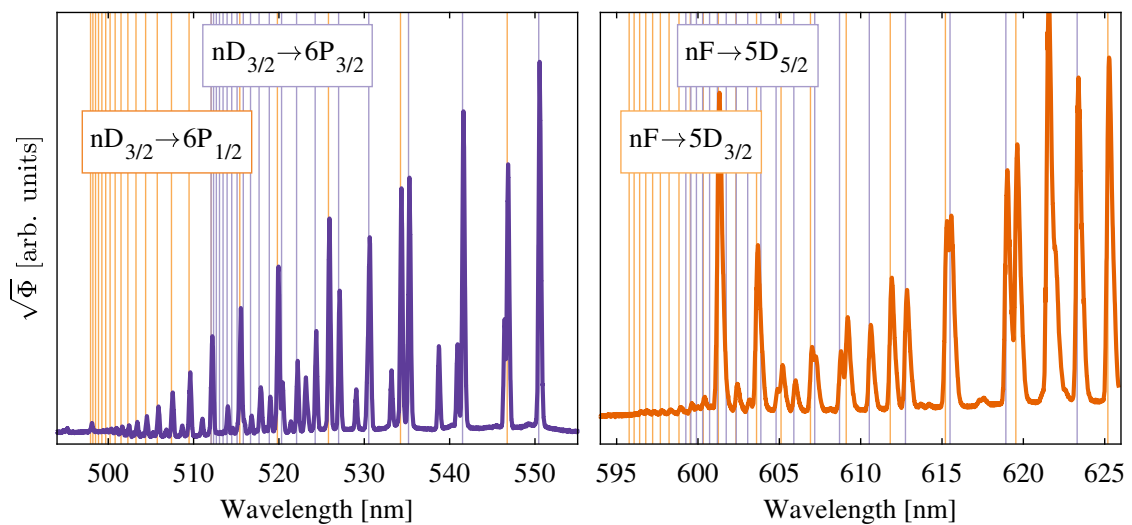


Figure 11.3: Exemplary recombination spectrum of the plasma, plotted as the square root of the photon flux. The two panels show different wavelengths ranges, but the relative amplitudes are comparable. The vertical lines show the expected wavelength series of decays up to $n = 30$. Due to their larger ionization cross-section and longer lifetime, the radiative decay is suppressed for transitions originating from higher principal quantum numbers, i.e., towards shorter wavelengths.

Finally, the recombination in the plasma gives rise to the distinct fluorescence spectrum [32, 164, 165] which can be measured. The neutralization of the positively charged ions with the negative electrons leads to a broad, discrete distribution of Rydberg principal quantum number states which then subsequently decay. Figure 11.3 shows such characteristic spectrum that extends over a wide range of different wavelengths. Each of the discrete transitions itself designates a certain decay to an energetically lower lying state. Note that only radiative decay contributes to the fluorescence spectrum. Since the vapor is still heavily perturbed by the charges in the plasma, re-ionization within the lifetime of such state is quite possible. As a consequence, fluorescing transitions originating from higher Rydberg states (with larger cross-sections) are suppressed, compared to lower lying states. We could not verify a threshold behavior as in [142], such that only

Rydberg decays *up to* the addressed state are visible. Instead, we observe a *fading-out* of the decays from the higher lying states, as is shown in fig. 11.4, as also hinted to in [165]. The supposed threshold seems to be coincidental and requires further research.

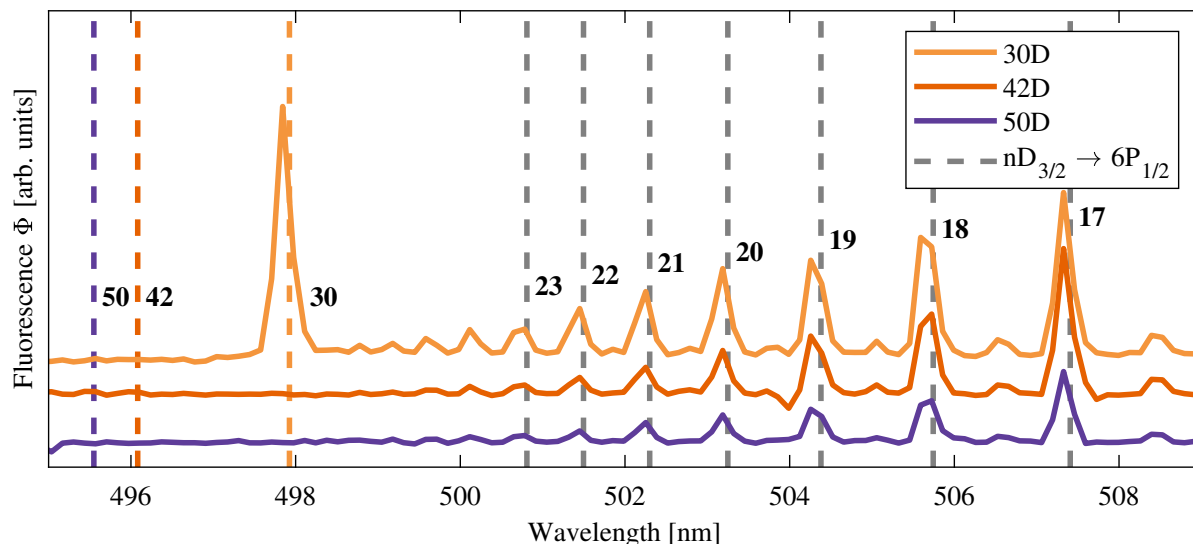


Figure 11.4: Details of the fluorescence spectra when driving to different Rydberg states. The vertical lines indicate the transition wavelength from the $nD_{3/2}$ state to $6P_{1/2}$. Note that the $nD_{5/2}$ is addressed by the lasers, so the $nD_{3/2}$ state is indirectly populated. The manifold of lines fades out for higher lying states, independent of the addressed Rydberg level. Due to the n^4 scaling of the cross-section, ionization dominates the decay from 42D and 50D, but fluorescing decay is still visible as a distinguished peak in the 30D trace. Laser intensities are adjusted to achieve equal Rabi frequencies Ω_R for all three states.

11.2 Microwave-transmission and fluorescence measurements

We measure the change in transmission δT_{RF} of a radio-frequency signal to demonstrate that a plasma exists in the gas. The dispersion relation for electromagnetic waves through a plasma is given by

$$\omega^2 = \omega_p^2 + c_0^2 k^2, \quad (11.1)$$

under the assumption of no magnetic fields. The wave number k is cut-off for frequencies above the plasma frequency. Inspired by [166], we anticipate to be able to detect such a change in either phase and/or transmission of the RF wave. The resulting traces are plotted in fig. 11.5 and show a single peak in the regarded frequency range. The resonance position and its shift with the Rydberg Rabi frequency already hints towards the presence of an (electron) plasma: The effect of the radio-frequency excitation does not occur in a neutral cesium gas at these frequencies. As the resonance position does not scale linearly

towards zero with the Rabi frequency Ω_R (see also fig. 11.6), we can exclude Autler-Townes splitting as the origin, which would be at lower frequencies anyways. Transitions between different Rydberg states are also highly unlikely, because the resonance frequency becomes lower for decreasing Rabi frequencies. In sec. 11.3, we show that interpreting the resonance position as the plasma frequency leads to electron densities that are plausible. The data-set was taken for two different Rydberg excitation laser Rabi frequencies, Ω_R , but otherwise identical configurations. Both lasers were locked on resonance and excite the atoms to the $30D_{5/2}$ state. The ground state cesium density was $\mathcal{N}_g = 3 \times 10^{12}/\text{cm}^3$ and the set radio-frequency power of the microwave-generator¹ was $P_{\text{RF}} = -15$ dBm. For the RF transmission measurements, additional attenuation of -33 dB was placed in front of the sending antenna.

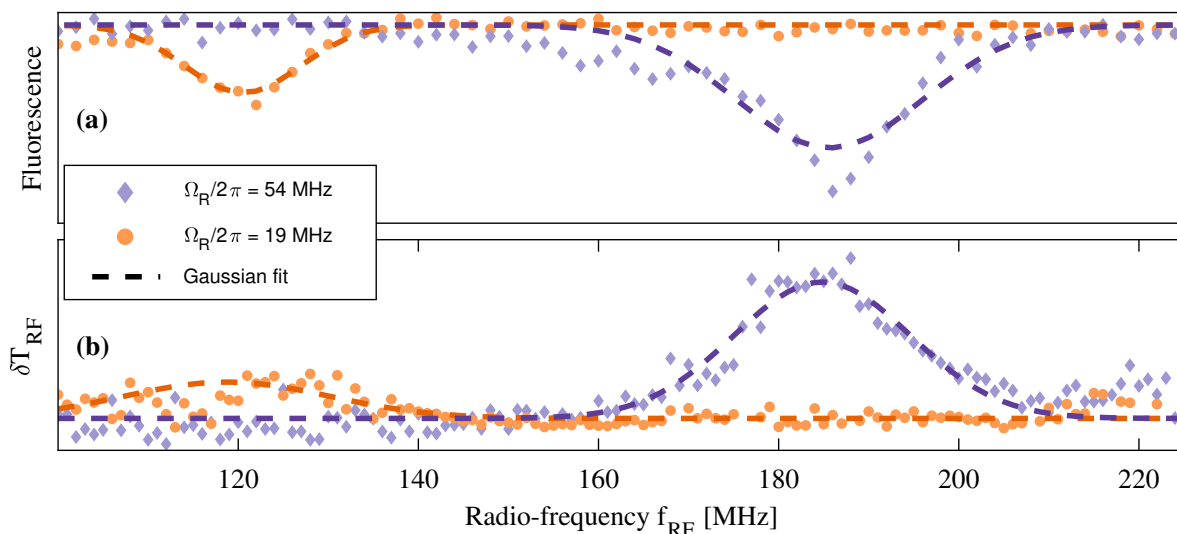


Figure 11.5: Fluorescence vs. radio-frequency (a) and radio-frequency transmission change (b) for the $30D_{5/2}$ Rydberg state for the same experimental conditions, with both lasers locked. Experimental parameters are $P_{\text{RF}} = -15$ dBm, $\Omega_B/2\pi = 3.6$ MHz and $\mathcal{N}_g = 3 \times 10^{12} \text{ cm}^{-3}$. The dashed lines are Gaussian fits to guide the eye.

A careful look at fig. 11.5 appears puzzling at first, since the radio-frequency field does not appear in absorption but seems to be an increased transmission. This is deceptive. Normally, one would expect reflection of RF below the plasma frequency, and transmission above the resonance. According to our definition of δT_{RF} , eq. (10.1), changes in both amplitude and phase contribute to the positive definite spectrum. Thus, both imaginary and real part of the electric susceptibility are probed simultaneously, and their contributions are mixed together. Additionally, one has to consider that the two antennas in our experiment are in the near-field of each other, which disputes assumptions with macroscopic properties of a medium, such as susceptibility or refractive index. We therefore avoid quantitative statements about the degree of phase shift or the decrease in transmission

¹Anritsu, MG3694C

The important information we excerpt from these measurements is that a distinguished resonance frequency exists and that this frequency strongly depends on the excitation Rabi frequency.

Figure 11.5 additionally shows the change in fluorescence measured as a function of the modulation frequency, f_{RF} . The overlap of the radio-frequency and fluorescence signals show that the fluorescence can be used as a surrogate for the radio-frequency transmission signal. Such a connection has important experimental implications, because the fluorescence signal has a much better signal-to-noise ratio than the radio-frequency transmission signal, and therefore requires less averaging to obtain a clear signal. Measuring the fluorescence is a much easier and faster procedure: it takes about one hour for each trace in fig. 11.5(b), while the data for fig. 11.5(a) is captured within tens of seconds.

The change in fluorescence can be explained by considering how the radio-frequency field accelerates the free electrons into an oscillating motion with an amplitude depending on the frequency of the radio-frequency field. If the radio-frequency field is resonant with the plasma frequency, the amplitude of the electron oscillation is maximal and this motion effectively decreases the electron density within the laser beams. If the amplitude of the electrons exceeds the radial extent of the laser beams, the recombination probability in the center of the beam—where the ions are presumably located and most fluorescence is collected—decreases. For large electric field amplitudes, the electrons can also collide with the walls of the vapor cell. This also reduces the number of particles contributing to the fluorescence signal.

11.3 Plasma properties

As we have established relations between the fluorescence signal and the probe laser transmission, as well as between fluorescence and an effect on RF transmission properties, it appears that we can study the plasma characteristics using the fluorescence signal. Figure 11.6 shows a typical series of measurements with varying Rydberg excitation laser intensities. As the Rabi frequency Ω_{R} gradually increases, the plasma resonance clearly shifts its position while the signal simultaneously increases in amplitude. The shift in the plasma resonance enables us to extract the density of the electron plasma. Given the relation between plasma frequency f_{p} and the electron density \mathcal{N}_{e} , eq. (3.29),

$$\mathcal{N}_{\text{e}} = (2\pi f_{\text{p}})^2 \frac{\epsilon_0 m_{\text{e}}}{q_{\text{e}}^2}, \quad (11.2)$$

the electron density can be calculated. The axis ticks above fig. 11.6 are computed in exactly this way, yielding an electron density on the order of $1 \times 10^8 \text{ cm}^{-3}$.

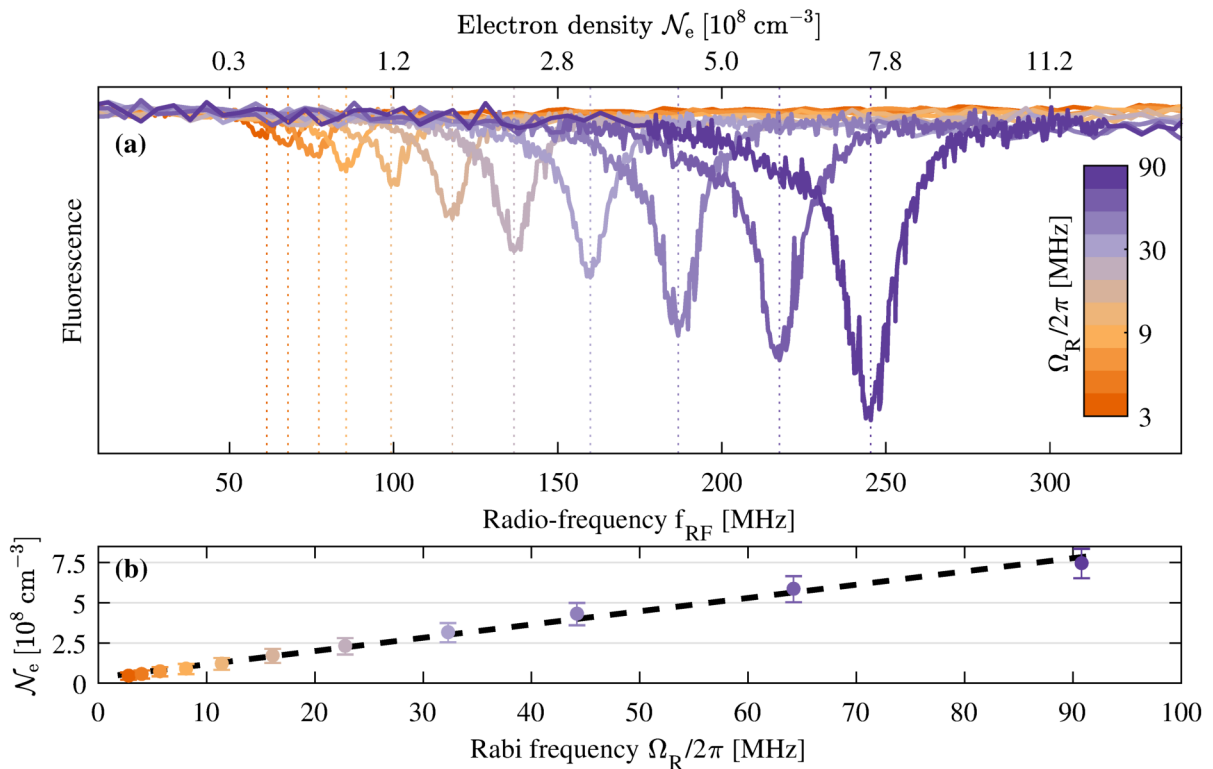


Figure 11.6: Plasma resonance peaks in the fluorescence signal, and corresponding electron density. Error margin in (b) is the full-width at half maximum of the features in (a). Experimental parameter: radio-frequency power $P_{\text{RF}} = -16$ dBm, density $\mathcal{N}_{\text{g}} = 3 \times 10^{12} \text{ cm}^{-3}$, $\Omega_{\text{B}}/2\pi = 3.6$ MHz. The $30\text{D}_{5/2}$ Rydberg state was used for the measurements.

Along with the plasma frequency, the Debye length, eq. (3.5), and the Coulomb coupling parameter, eq. (3.15) characterize the plasma. We assume the plasma temperature to be equal to the vapor temperature, $T \approx 370$ K, because the ions are created in the vapor at that temperature, and the electrons quickly thermalize with the ions via Coulomb interaction. The Debye length is then $\lambda_{\text{D}} \sim 100 \mu\text{m}$, and the Coulomb coupling parameter is $\Gamma_e \sim 0.006$. These characteristics indicate that the electron plasma is in the weakly coupled regime. The associated plasma parameter, eq. (3.10), which measures the number of electrons in a Debye sphere, is $N_{\text{D}} = 10^3$. The volume of the Debye sphere hence contains 10^3 ions on a background of 1.3×10^7 cesium atoms. The plasma is weakly ionized with properties comparable to the earth's ionosphere [167].

Note that the observed plasma resonance in fig. 11.6 must be that of the electrons: calculating the ion density using these resonant frequencies results in densities that are 2 to 100 times larger than the peak cesium vapor density $\mathcal{N}_{\text{g}} = 3 \times 10^{12} \text{ cm}^{-3}$ we measured in the cell. A prediction for the corresponding ionic plasma frequency can be drawn from the ratio between the electron mass and the mass of a cesium ion. Assuming the same

density, the ionic plasma would oscillate at a frequencies

$$f_{\text{ion}} = f_e \sqrt{\frac{m_e}{m_{\text{Cs}}}} \approx \frac{f_e}{500}. \quad (11.3)$$

A search for the ionic plasma frequency around 1 MHz did not show any signature in the fluorescence. For two reasons this is not surprising: on the one hand, the ions are much heavier than the electrons, and therefore require even stronger fields to be accelerated significantly. On the other hand, the mismatch between the dipole antenna and wavelength increases, and therefore less RF power reaches the atoms. It is unclear, if RF power is brought into the cell volume at all at these low frequencies in our experimental apparatus.

11.4 Scaling behavior of the bistability edges

11.4.1 Plasma transition and edge frequency

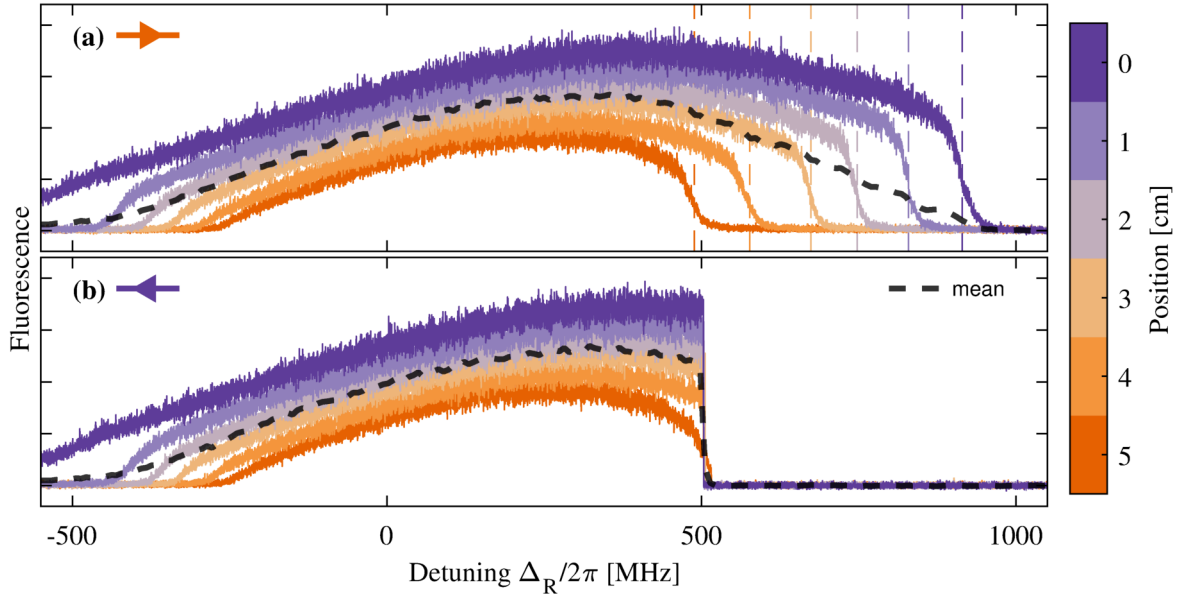


Figure 11.7: Fluorescence signal collected from different spatial positions along the vapor cell, with increasing distance from the entrance window of the blue laser beam. (a) Scan from red to blue detuning (i.e., left to right). (b) Scan from blue to red detuning. All traces in (b) feature the same sharp edge at approx. 500 MHz. The dashed line shows the mean of the fluorescence signal. The mean is similar to the integrated signal one would obtain by measuring the probe transmission, cf. fig. 11.2. Experimental parameters are $\mathcal{N}_g = 3 \times 10^{12} \text{ cm}^{-3}$, $\Omega_B/2\pi = 2.5 \text{ MHz}$ and $\Omega_R/2\pi = 18 \text{ MHz}$. Data is shown for the $42\text{D}_{5/2}$ Rydberg state.

Figure 11.7 shows a set of fluorescence signal data for both red to blue and blue to red 1064-nm laser scans at different fluorescence collection positions z along the vapor cell. The fluorescence is associated with population in a large number of different Rydberg states, as a result of the recombination of the plasma. By interpreting the plots only at the blue detuned side, we note that the system stays in the state with a high Rydberg density—where high Rydberg density simultaneously implies high charge density—when scanning from red towards blue detuned wavelengths, even for larger detunings, fig. 11.7(a). The behavior of these curves is to be contrasted with that in the second panel, fig. 11.7(b), where a sharp transition upwards occurs at the same 1064-nm laser detuning for all fluorescence collection positions. Because a lot of *directions* are involved in the following analysis, we try to avoid confusion by clarifying: The laser detuning scan has a *positive* direction which goes from the red to the blue detuned side of the resonance, and a *negative* direction, from blue to red. The fluorescence signal, cf. fig. 11.7, must be followed along the scan direction in which the data was recorded: For the positive detuning scan, fig. 11.7(a), the signal quickly falls *down* to the baseline; for the negative detuning direction, fig. 11.7(b), the signal starts from the baseline, and suddenly rises *up*.

It is apparent that for larger distances from the 455-nm laser beam input window (corresponding to larger propagation distances of the blue light through the vapor cell), the overall strength of the fluorescence signal decreases. The decreasing 455-nm laser intensity affects the detuning at which the falling edge of the hysteresis occurs for red to blue detuning, fig. 11.7(a). In opposition, the plots in fig. 11.7(b) all feature the same sharp edge at a detuning $\Delta_R/2\pi$ of approximately 500 MHz. This rising edge, fig. 11.7(b), where the data is acquired for blue to red detuning, is unaffected by the varying 455-nm laser absorption along the length of the vapor cell. When the system is in the bistable part of the spectrum, but in the low Rydberg population state, the conditions for the ionization only need to be fulfilled at any position along the laser beam. The avalanche ionization then quickly spreads across the whole cell, cf. sec. 11.1. The transition based on a *seeding* suggests that it is a first-order phase transition between two meta-stable states, although in general, the transition from a neutral gas to a plasma is continuous (e.g., with respect to the temperature), and typically classified as a second-order phase transition. In fig. 11.2, the transition to the plasma state happens much faster than two consecutive frames of the camera (frame rate 5 s^{-1}). A more restrictive upper limit is found by looking at the rising slope of the edge in fig. 11.7(b), which is recorded as a function of time: it takes about 0.1 ms for the signal to rise. If we assume this to be the duration it takes for the domain boundary to pass the extend of the 1.5-mm spot from which fluorescence is collected, we can estimate the timescale for the whole cell length of 5 cm to be on the order of 5 ms.

Typically, the conditions for the avalanche ionization are fulfilled first where the maximum Rabi frequency Ω_B exists, i.e., at the entrance window of the blue laser. One can, however, carefully tune the system to feature two transitions, as displayed in fig. 11.8. In principle

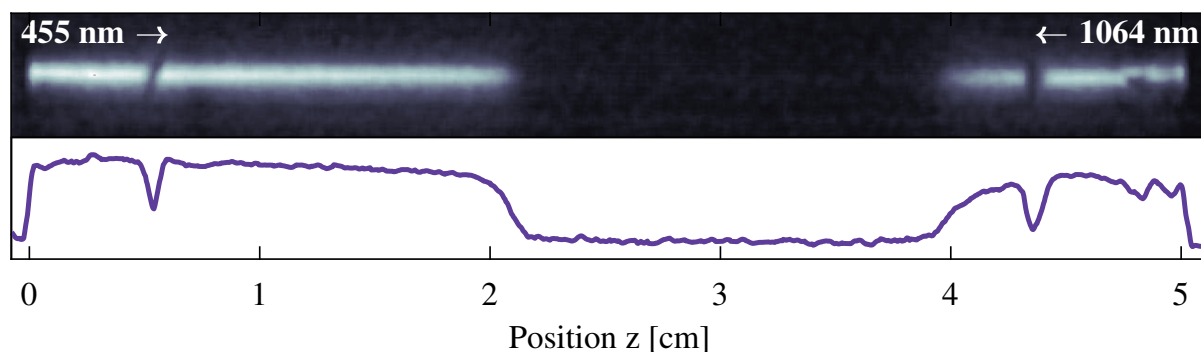


Figure 11.8: Two simultaneous phase transitions along the beam. The back-reflected blue light and less dispersed red light from the right side decrease towards the left. This leads to the additional threshold criterion from right to left. The bottom panel shows the pixel values along the center line. Our vapor cell does not have an anti-reflective coating.

the same argument as before holds, only this time it might be caused by the additional back reflection of the blue light, and possibly a very subtle gradient in the red light, with stronger intensity closer to the entry window on the right hand side. Our cell does not have an anti-reflective coating.

The abrupt jump in the Rydberg population and associated change in fluorescence is referred to as the *edge frequency*. In the numerical evaluation of the data, we determine the edge frequency as the 1064-nm laser detuning value, Δ_E , where the fluorescence signal exceeds 1/4 of the maximum value in each curve, when tracing the data from the blue side (in this definition regardless of the detuning sweep direction for which the data was recorded). For the positive sweep, this gives us $\Delta_{E,\downarrow}$, for the negative sweep we have $\Delta_{E,\uparrow}$, respectively. It is useful to look at $\Delta_{E,\downarrow/\uparrow}$ to determine how its value scales with the laser Rabi frequencies and density, in order to learn about the dynamics of the driven system.

11.4.2 Adjusted Rabi frequency

The laser beams are being absorbed while propagating through the atomic medium. Therefore, the Rabi frequency in general is a function of the position, $\Omega = \Omega(z)$, cf. fig. 11.1. In our experiment, the 1064-nm laser intensity is assumed to be not considerably affected by absorption along the cell. The blue 455-nm laser beam however is strongly absorbed, since it couples the highly populated ground state to the intermediate state. For this beam, the optical depth is large, and even though the intensity is above saturation, there is still considerable absorption. As the *local* Ω_B varies along the length of the vapor cell, also the excitation and ionization conditions vary. The spectrum one obtains by measuring the fluorescence therefore depends on the spatial position at which the fluorescence is

collected. As a consequence, one needs to adjust Ω_B according to the position where the measurement is made, which is indicated by the asterisk, Ω^* . We numerically propagate the intensity through a thermal ensemble of the respective density to determine Ω^* at the z -position of interest. We hereby follow the derivation in [49], and numerically integrate eq. (1.38).

11.4.3 Scaling behavior

The plasma and its role in the appearance of the bistability can be further analyzed by investigating the dependence on the laser Rabi frequencies and vapor density. To study the optical bistability, the 1064-nm laser is scanned across the $7P_{3/2} \rightarrow 42D_{5/2}$ transition. Since the system is bistable, both positive and negative scan directions are recorded and treated separately. We measured spectra for a wide range of experimental parameters, varying vapor density and both excitation laser Rabi frequencies, Ω_B and Ω_R . We focus on analyzing the edge, i.e., the transition from and to the plasma state, as we sweep the 1064-nm laser detuning across the two-photon resonance. The overall shape and amplitude of the signal is not considered further in this analysis. It turns out to be possible to combine the experimental parameters into two scaling parameters S_\downarrow or S_\uparrow , for the positive (red to blue) scan and negative (red to blue) direction, respectively. These scaling parameters are defined as

$$S_{\downarrow/\uparrow} = \left(\frac{\mathcal{N}_g}{\mathcal{N}_0}\right)^a \cdot \left(\frac{\Omega_B}{\Omega_0}\right)^b \cdot \left(\frac{\Omega_R}{\Omega_0}\right)^c, \quad (11.4)$$

striped of its units by arbitrary normalization factors Ω_0 and \mathcal{N}_0 . We have discovered that the two sets of exponents $(a, b, c)_\downarrow$ and $(a, b, c)_\uparrow$ can be chosen in such a way that the detuning frequencies at which the system jumps between high and low Rydberg/ion population state scale linearly with S_\uparrow or S_\downarrow ,

$$\Delta_{E,\downarrow/\uparrow} = p \cdot S_{\downarrow/\uparrow} + q, \quad (11.5)$$

where p and q are arbitrary proportionality factors and offsets, respectively. Additionally, we introduce the following notation for the scaling factors: The asterisk, e.g., S_\uparrow^* , denotes that for the calculation of this scaling factor, the blue Rabi frequency is compensated for absorption up to the position where the fluorescence measurement is made, as described in sec. 11.4.2.

The set of data points we acquired for the bistability edge position are plotted in fig. 11.9. The plots cover $\Omega_B/2\pi$ over a range of 1.8 to 12 MHz, $\Omega_R/2\pi$ from 15 to 50 MHz, and \mathcal{N}_g within 0.05 to $7 \times 10^{12}/\text{cm}^3$. The values for the three scaling exponents, $(a, b, c)_{\downarrow/\uparrow}$, are obtained by non-linear least-squares fitting to the data plotted in fig. 11.9, independently for both detuning sweep directions. The cost function that is minimized here is the deviation of each point from the point cloud to a linear regression line. Hence, in every

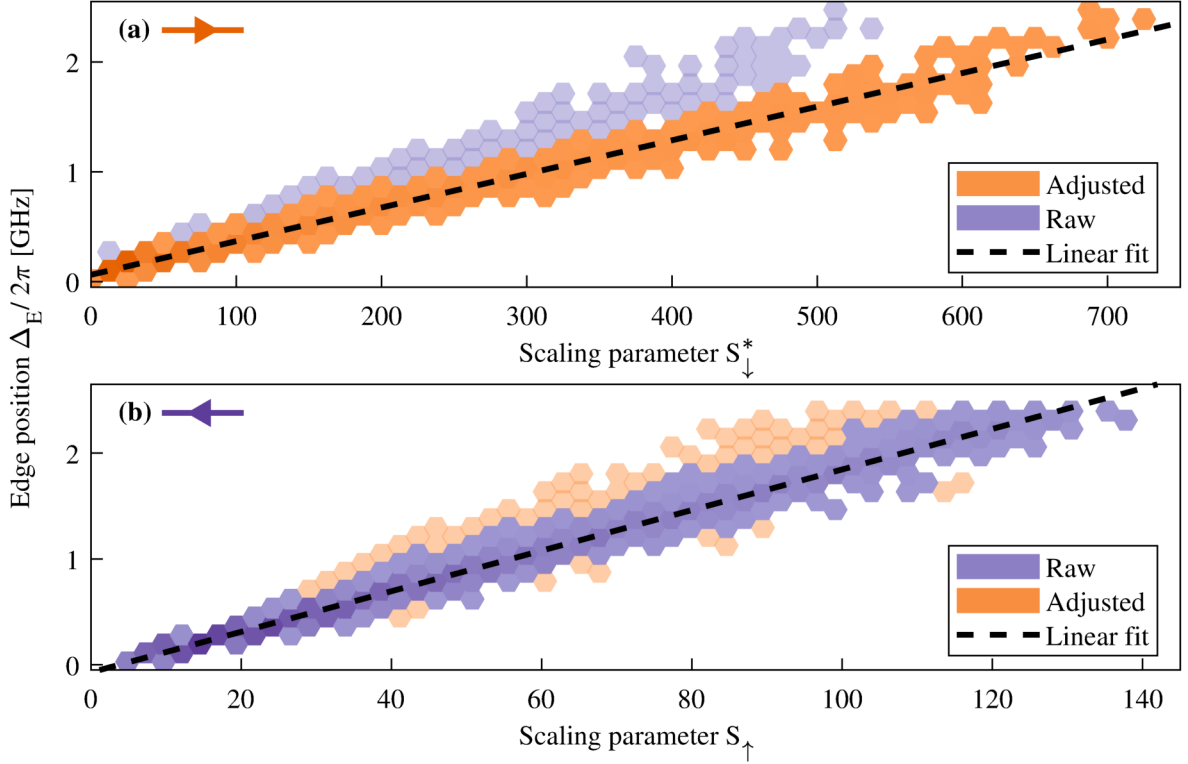


Figure 11.9: Heat map of the bistability frequency edge positions, $\Delta_{E,\downarrow/\uparrow}$, as a function of the scaling parameters S_{\downarrow}^* and S_{\uparrow}^* , according to eq. (11.4). (a) Red to blue detuning sweep. (b) Blue to red sweep. For comparison, the larger spread of the distributions with the respective raw and absorption adjusted Rabi frequencies (Ω_B and Ω_B^* , respectively) are also shown.

iteration step of the least-squares fitting routine, the scaling parameter for the current values of the three exponents needs to be computed for each datapoint first. Then, a linear regression line is fitted to this point cloud and the cost values can be calculated. We calculate the scaling for both adjusted and raw Rabi frequencies, $\Omega_B^{(*)}$. The results are given in tab. 11.1. We find that using the blue Rabi frequencies as indicated by the asterisk in the table leads to more narrow distributions of points, cf. fig. 11.9. Using the other two combinations, corresponding to S_{\uparrow}^* or S_{\downarrow} , leads to the broader distribution of the point-clouds that are shown in the same figure. This again reflects on the fact that for S_{\uparrow}^* , the maximally available Rabi frequency anywhere in the cell is relevant, while for S_{\downarrow}^* the conditions at the position of measurement define the behavior, cf. sec. 11.1.

Related experiments demonstrate that the frequency shift of the phase transition additionally scales with the fourth power of the effective principal quantum number, n^{*4} [139]. This is in agreement and consistent with our interpretation, because the geometric cross-section of Rydberg atoms for ionizing collisions also scales with n^{*4} , eq. (2.31).

The fact that the values are different for S_{\uparrow}^* and S_{\downarrow}^* indicates that the dynamics are different for the two scanning directions, which is an indication, but not required for

	(Scan)	a (\mathcal{N}_g)	b (Ω_B)	c (Ω_R)
correct adjustment				
S_\uparrow	(\leftarrow)	0.81 ± 0.01	0.95 ± 0.02	1.08 ± 0.02
S_\downarrow^*	(\rightarrow)	0.54 ± 0.01	0.56 ± 0.01	0.97 ± 0.02
wrong adjustment				
S_\uparrow^*	(\leftarrow)	0.86 ± 0.02	0.80 ± 0.02	1.11 ± 0.03
S_\downarrow	(\rightarrow)	0.47 ± 0.01	0.59 ± 0.01	0.89 ± 0.02

Table 11.1: Scaling exponents as in eq. (11.4) with 95% confidence intervals obtained by the fitting routine. The systematic error is probably much larger. We therefore believe that these values can easily be in agreement with integer or half-integer values. For completeness, we also show the parameters one would obtain with the *wrong* Rabi frequency adjustments, that lead to wider spread of the point-clouds, cf. fig. 11.9.

the bistable behavior. In the next section, we compare these numbers to a simple rate model.

11.4.4 Assessment of the scaling behavior via rate equations

Interpreting the numerical values of the exponents for the scaling parameters reveals interesting properties of the bistable system. An intuitive picture based on rate equations can be developed, to explain the rough trend of the determined exponents, (a, b, c) , and also justify the distinction between the *raw* and *adjusted* Rabi frequency. The most important parameters are the density of Rydberg atoms and ions, \mathcal{N}_{Ryd} and \mathcal{N}_{ion} . The two steady state densities can be obtained by solving the coupled system of rate equations,

$$\begin{aligned}
\dot{\mathcal{N}}_{\text{ion}} &= \mathcal{N}_{\text{Ryd}}\mathcal{N}_g\sigma_g\bar{v} + \mathcal{N}_{\text{Ryd}}\mathcal{N}_e\sigma_e\bar{v}' \\
&\quad - \mathcal{N}_{\text{ion}}\mathcal{N}_e\sigma_r\bar{v}' - \mathcal{N}_{\text{ion}}\Gamma_t \\
\dot{\mathcal{N}}_{\text{Ryd}} &= -\mathcal{N}_{\text{Ryd}}\mathcal{N}_g\sigma_g\bar{v} - \mathcal{N}_{\text{Ryd}}\mathcal{N}_e\sigma_e\bar{v}' \\
&\quad + \mathcal{R}_{\text{pump}}.
\end{aligned} \tag{11.6}$$

The parameters in the two equations are cross-sections for Rydberg-ground state collisions σ_g (first term in both $\dot{\mathcal{N}}_{\text{ion}}$ and $\dot{\mathcal{N}}_{\text{Ryd}}$), Rydberg-electron collisions σ_e (second term, also both eqs.), and recombination of ions with electrons σ_r (third term in $\dot{\mathcal{N}}_{\text{ion}}$). For every collision term, \bar{v} is the mean relative velocity of the respective interacting species. It is reasonable that the velocity of all the heavier particles is the same. When the much lighter electrons are involved, this is indicated by a prime. Ions diffuse away at a rate Γ_t . The effective rate at which atoms are excited to the Rydberg state is $\mathcal{R}_{\text{pump}}$, which will be specified for the two cases of high and low Rydberg population later. The decay of the Rydberg population, also dominated by transit time decay, only results in an offset in the effective pump rate, and does not play a role for the scaling behavior. Depending

on whether the system approaches Δ_E from the ground state side ($\mathcal{N}_{\text{ion}}, \mathcal{N}_e, \mathcal{N}_{\text{Ryd}} \approx 0 \text{ cm}^{-3}$) or the highly populated excited state side ($\mathcal{N}_{\text{ion}}, \mathcal{N}_e, \mathcal{N}_{\text{Ryd}} \gg 0 \text{ cm}^{-3}$), different approximations for eq. (11.6) are to be applied. For the analysis of the scaling behavior in both of these two extremes in the following paragraphs, we assume the electron and ion density to be approximately the same, $\mathcal{N}_e \approx \mathcal{N}_{\text{ion}}$, both given by the parameter \mathcal{N}_c .

For blue to red detuning sweeps which are described by S_\uparrow in tab. 11.1 and fig. 11.9(b), Δ_E is approximately linear with respect to all 3 parameters, $(a, b, c) \approx 1$. We also observe that all traces in fig. 11.7(b) feature a sharp edge at the same detuning value. In order for the system to jump to the plasma state, it seems sufficient to trigger the threshold for the avalanche mechanism at any point along the vapor cell. Close to the entry of the blue laser, the highest Rydberg excitation rate is available. Therefore, the *raw* Rabi frequency, calculated from the intensity right in front of the cell, determines when the system jumps to the plasma state. It is important to understand that the Stark shift and associated spectral broadening due to the charge distribution does *not* play a role before this transition has happened. The system starts from the ground state, so we can approximate the rate equations, eq. (11.6), as

$$\begin{aligned} \dot{\mathcal{N}}_c &\stackrel{\mathcal{N}_c \ll \mathcal{N}_g}{=} \mathcal{N}_{\text{Ryd}} \mathcal{N}_g \sigma_g \bar{v} - \mathcal{N}_c \Gamma_t \\ \dot{\mathcal{N}}_{\text{Ryd}} &\stackrel{\mathcal{N}_c \ll \mathcal{N}_g}{=} -\mathcal{N}_{\text{Ryd}} \mathcal{N}_g \sigma_g \bar{v} + \mathcal{N}_g \frac{\Omega_B \Omega_R}{\tilde{\Delta}}. \end{aligned} \quad (11.7)$$

Here, the pump rate to the Rydberg state is taken to be the effective two-photon Rabi frequency divided by an effective detuning $\tilde{\Delta}$, considering this a non-resonant two-photon excitation. Due to the Doppler effect, most atoms in the ensemble are detuned with respect to the $7P_{3/2}$ intermediate state, The detuning of the Rydberg laser with respect to the transition is trivial. Without the plasma or a significant number of charges present, the line width of the Rydberg transition corresponds to its natural width, and both lasers are above saturation. Hence, both Rabi frequencies contribute linearly to the pump rate. In steady state, the charge density in eq. (11.7) is proportional to

$$\mathcal{N}_c \propto \mathcal{N}_g \Omega_B \Omega_R, \quad (11.8)$$

which reflects the measured scaling, that is close to being linear in all three parameters.

For the opposite scan direction, scaling parameter S_\downarrow^* in tab. 11.1 and fig. 11.9(a), the dominant terms in eq. (11.6) are

$$\begin{aligned} \dot{\mathcal{N}}_c &\stackrel{\mathcal{N}_c \gg 0}{=} \mathcal{N}_{\text{Ryd}} \mathcal{N}_c \sigma_e \bar{v}' - \mathcal{N}_c^2 \sigma_r \bar{v}' \\ \dot{\mathcal{N}}_{\text{Ryd}} &\stackrel{\mathcal{N}_c \gg 0}{=} -\mathcal{N}_{\text{Ryd}} \mathcal{N}_c \sigma_e \bar{v}' + \mathcal{N}_g \frac{\Omega_B^*}{2\Gamma_D} \frac{\Omega_R^*}{\Gamma_{\text{Ryd}}}. \end{aligned} \quad (11.9)$$

With the plasma present, the Rydberg transition is massively broadened by the varying Stark shifts and the 1064-nm laser intensity is effectively on resonance, and *below* the saturation intensity, while the 455-nm laser transition remains saturated. The intermediate state population at each position along the cell is proportional to the local Rabi frequency Ω_B^* . More precisely, it is proportional to Ω_B^* divided by the Doppler width Γ_D , reflecting the fact that a wider range of velocities contribute to the population as the excitation linewidth is increased due to power broadening. From the intermediate state population, atoms are then excited to the Rydberg state. Since the Rydberg line width is disturbed by the plasma, this is an incoherent effect, and only the number of photons is of importance here. As a result, the Rydberg population depends quadratically on Ω_R . Solving eq. (11.9) for the steady state charge density gives

$$\mathcal{N}_c \propto \sqrt{\mathcal{N}_g} \sqrt{\Omega_B^*} \Omega_R, \quad (11.10)$$

which is in agreement with the experimentally obtained scaling S^* shown in tab. 11.1.

Since both \mathcal{N}_c from our theoretical considerations and Δ_E from the measurements yield the same scaling behavior, we can conclude that the detuning at which the system undergoes the transition between the two meta-stable states is proportional to the charge density in the vapor,

$$\Delta_E \propto \mathcal{N}_c. \quad (11.11)$$

It is important to note that most of the measurements are not performed in one of the extreme cases mentioned here. The crude simplification does not hold, and a more elaborate scaling follows. Also, only the detuning at which the transition happens is considered here, the overall line shape of the signal has been neglected. Therefore a detailed numerical model is developed in the next part of this thesis.

12 Part III: Conclusion

In this part of the thesis, we have built on the previously established awareness that charged particles are present when exciting atoms in a thermal vapor to Rydberg states. We introduced a new experimental layout that allows both electromagnetic and optical access to the vapor cell perpendicular to the excitation laser beams. We were able to confirm the natural supposition that the vapor of ionized Rydberg atoms shows the characteristics of a plasma. By measuring the change in transmission of an RF signal, although in phase and amplitude simultaneously, we saw a resonance feature that changes its position with the Rabi frequency. Identifying this resonance with the plasma frequency of the electron gas, we obtained an estimate of the electron density that is within a plausible range. We derived values for the Debye length and the Coulomb coupling parameter and thereby characterized the plasma as a weakly ionized one.

By analyzing the fluorescence that is radiated perpendicular to the laser beam axis, we gained a deeper understanding of the mechanism that is responsible for the optical bistability in thermal Rydberg vapors. With the help of spatial resolved fluorescence measurement, we shed light on the temporal progress of the phenomenon. For one detuning sweep direction, a characteristic fluorescing ray suddenly streaks across the length of the cell. For the opposite direction, this ray gradually retracts. Systematic measurements of the phase transition in the fluorescence signal allowed us to quantify scaling exponents of all our experimental parameters. We demonstrated that the point of plasma formation scales linear in all three parameters ($\Omega_B, \Omega_R, \mathcal{N}_g$), while the reverse transition is only linear in Ω_R , and scales with the square root of the remaining two. This scaling behavior agrees very well with a simple empirical rate model for the charge density.

Part IV

Numerical Modeling of the Interplay between Rydberg Atoms and the Plasma

13 Part IV: Introduction

Measuring the fluorescence perpendicular to the beam axis instead of the usual transmission signal facilitates—literally—a new perspective on optical bistability in thermal Rydberg vapors. In the previous part of the thesis, we developed a microscopic picture of the phenomenon by asserting that a plasma is formed. We presume that the mechanism which contributes to this plasma formation is that inelastic, ionizing collisions between Rydberg atoms and ground state atoms create an initial concentration of charged particles in the vapor. As a secondary step, the electrons produced by the ionization of the Rydberg atoms then become an additional source for collisions with Rydberg atoms, leading to even more charges in the system. Eventually, when sufficiently many Rydberg atoms are ionized, a steady-state plasma is formed.

In this part of the thesis, we provide affirmation that our assumptions are sound by engineering a numerical model of the *atom-plasma-laser* system. The simulation is based on the density matrix formalism and ensemble averaging of an inhomogeneous medium. The key aspect of the model is to project the charge density to a distribution of Stark shifts and dephasing. This provides a feedback mechanism, that, in combination with the non-linearity of the avalanche ionization, is responsible for the emergence of optical bistability in thermal Rydberg vapor.

We first describe the building blocks of the model and demonstrate the iterative algorithm to calculate equilibrium states of the system. Fluorescence measurements from the experimental setup as described in the previous part of this thesis allows us to validate the model and refine its parameters by least squares optimization. We show that measured and simulated spectra are strikingly similar, and the obtained parameters that are plausible.

14 Concept and methods

14.1 Fundamental procedure

To calculate the state populations and coherences of the ensemble of thermal atoms excited by laser beams, we evaluate the steady state solution for the Lindblad master equation

$$\dot{\rho} = -\frac{i}{\hbar} [\rho, H] + L \stackrel{!}{=} 0, \quad (14.1)$$

as introduced in part I. Each calculation is performed for a given set of experimental parameters; i.e., a given set of density, laser detuning and Rabi frequencies. The key aspect of our model is to factor the effect of the electric field distribution of the plasma in terms of a shift and broadening into the system. The mechanisms covered by our simulation are as developed in sec. 11.1 and schematically depicted in fig. 14.1.

As is the usual approach for such calculations in a thermal ensemble of atoms, the solution to eq. (14.1) is independently calculated for each velocity class in a discretized binning of the velocities. Due to the Doppler effect, the actual laser detuning with respect to the transition frequency in the atoms reference frame differs for each velocity class. Only afterwards is the ensemble then averaged over the probability distribution of these bins, to get the comprehensive solution for the atomic vapor. Since additionally to the Doppler effect, we have to consider the electric fields caused by the plasma, we implement the equivalent with the Stark shift distribution. Analogous to the method of Doppler averaging, we now integrate over the combined probabilities of the electric field and velocity to obtain the observable quantities from the density matrix. Since the electric field distribution and the density matrix (and thus also the ion density) are mutually dependent, we calculate the two with an alternating method: for a given ion density, we first compute the electric field distribution. For this electric field distribution, we calculate the entries of the density matrix. From the density matrix, we get an updated value for the ion density. This leads us to an iterative algorithm, which will be described in sec. 14.5. The value for a density matrix element, given a specific Rydberg laser detuning and a known ion density, is the average of the density matrix element obtained using the respective probability distribution functions for the Stark shifts and the atomic velocities,

$$\bar{\rho}_{i,j} = \int_{-\infty}^{\infty} dv \int_0^{\infty} dE \quad f(v) \mathcal{P}_{\mathcal{N}}(E) \rho_{i,j}(v, E). \quad (14.2)$$

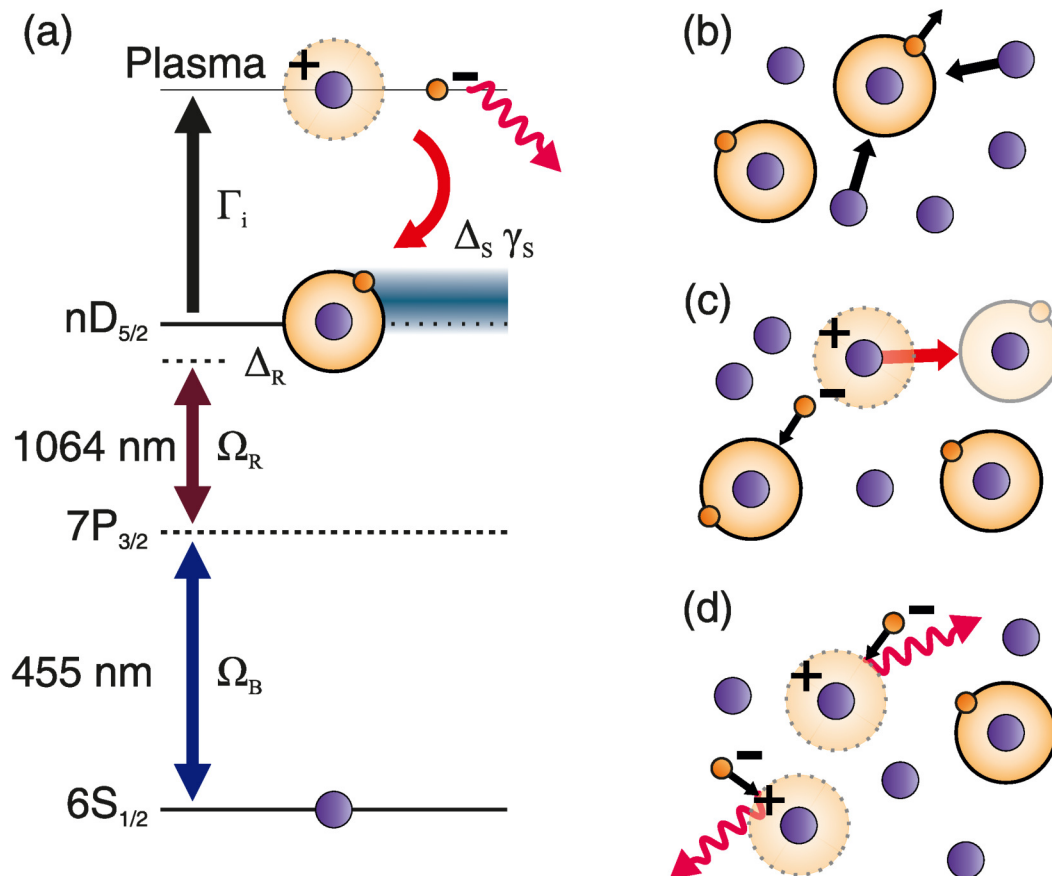


Figure 14.1: Key aspects of the numerical model. (a) Modified 3-level diagram of the inverted ladder scheme, with the additional plasma state, similar to [38]. The feedback of the plasma onto the Rydberg state imposes a shift and broadening. Also, the recombination leads to fluorescence from a broad distribution of many different states. (b-d) Illustration of the underlying mechanisms. (b) Rydberg-ground state collisions ionize few atoms, and lead to fast electrons. (c) Avalanche ionization due to electron-Rydberg collisions and broadening because of steep electric field gradients. The broadening and shifts of the Rydberg state facilitate an increase in Rydberg population. (d) Fluorescence due to the recombination in the plasma.

Hereby, $f(v)$ is the one dimensional Maxwellian distribution function [168] for the velocity, v , in the beam direction and $P_{\mathcal{N}}(E)$ is the electric field distribution as given in eq. (3.31).

14.1.1 Density matrix formalism

Applying the density matrix formalism, we interpret the thermal gas interacting with the lasers as a conventional 3 + 1 level system. The three lower levels represent the neutral gas including its excitation to the Rydberg state. The additional level (+1) describes the generation of ions, fig. 14.1(a), which gives rise to the plasma. The details of the density matrix, Hamiltonian and the Lindblad operator are as follows.

Density matrix The density matrix is given by

$$\rho = \begin{pmatrix} \rho_g & \rho_{1,2} & \rho_{1,3} & 0 \\ \rho_{2,1} & \rho_{2,2} & \rho_{2,3} & 0 \\ \rho_{3,1} & \rho_{3,2} & \rho_{\text{Ryd}} & 0 \\ 0 & 0 & 0 & \rho_{\text{ion}} \end{pmatrix}, \quad (14.3)$$

which already reveals the character of the system. The three atomic levels are fully described by the entries of the density matrix, with both populations and coherences. The plasma state is an incoherent addendum to it; since no coherence can be built up for this state, setting the appropriate entries in the density matrix to zero reduces the computational overhead.

Hamiltonian The states are coupled by the two lasers according to the Hamiltonian

$$H = \hbar \begin{pmatrix} 0 & \frac{\Omega_B}{2} & 0 & 0 \\ \frac{\Omega_B}{2} & -\Delta_1 & \frac{\Omega_R}{2} & 0 \\ 0 & \frac{\Omega_R}{2} & -\Delta_1 - (\Delta_2 + \Delta_S) & 0 \\ 0 & 0 & 0 & 0 \end{pmatrix} \quad (14.4)$$

with Rabi frequencies Ω_B and Ω_R . Because the 455-nm laser is assumed to be tuned to resonance, the detuning to the intermediate state only arises due to the Doppler shift, $\Delta_1 = \vec{k}_B \cdot \vec{v}$. The detuning with respect to the Rydberg state also includes the laser detuning Δ_R , which results in $\Delta_2 = \Delta_R + \vec{k}_R \cdot \vec{v}$. This allows to simulate spectra as recorded in the experiments, where the Rydberg laser detuning is scanned. Further, \vec{k}_B and \vec{k}_R are the wave vectors and \vec{v} is the atom velocity. Due to the low polarizability of the lower states, the ground state and intermediate state Stark shifts typically can be neglected. In the case of the Rydberg state, the additional term Δ_S produces the Stark shift by reason of the electric field strengths, fig. 14.1(c). As the electric field distribution

depends on the ion density ρ_{ion} , also the distribution of Stark shifts is ρ_{ion} dependent, and gives rise to a feedback mechanism, cf. sec. 4.1. The conversion between electric field distribution and Stark shift distribution is described in sec. 14.4.

Lindblad operator The Lindblad operator, $L = L_1 + L_2 + L_3$ accounts for dephasing, decay and ionization mechanisms. For better comprehension, it makes sense to split the operator into three parts.

The first part, L_1 , covers the intermediate state decoherence and decay, which is dominated by its natural lifetime. In the case of Cs $7P_{3/2}$, the rate is given by $\Gamma_{2,1}/2\pi = 1.18$ MHz [169]. This term gives the contribution

$$L_1 = \begin{pmatrix} \Gamma_{2,1}\rho_{2,2} & -\frac{1}{2}\Gamma_{2,1}\rho_{1,2} & 0 & 0 \\ -\frac{1}{2}\Gamma_{2,1}\rho_{2,1} & -\Gamma_{2,1}\rho_{2,2} & -\Gamma_{2,1}\rho_{2,3} & 0 \\ 0 & -\frac{1}{2}\Gamma_{2,1}\rho_{3,2} & 0 & 0 \\ 0 & 0 & 0 & 0 \end{pmatrix}. \quad (14.5)$$

Second, L_2 takes ionization and recombination into account,

$$L_2 = \begin{pmatrix} \Gamma_{\text{d}}\rho_{\text{ion}} & 0 & -\frac{1}{2}\Gamma_{\text{i}}\rho_{1,3} & 0 \\ 0 & 0 & -\frac{1}{2}\Gamma_{\text{i}}\rho_{2,3} & 0 \\ -\frac{1}{2}\Gamma_{\text{i}}\rho_{3,1} & -\frac{1}{2}\Gamma_{\text{i}}\rho_{3,2} & -\Gamma_{\text{i}}\rho_{\text{Ryd}} & 0 \\ 0 & 0 & 0 & \Gamma_{\text{i}}\rho_{\text{Ryd}} - \Gamma_{\text{d}}\rho_{\text{ion}} \end{pmatrix}. \quad (14.6)$$

The ionization rates are given by Γ_{i} while the loss of charged particles due to both recombination and particles propagating out of the region of interest, are represented by Γ_{d} . In our model, these two factors depend on the ion population of the ensemble, This nonlinear feedback is one of the two key aspects that contribute to the emergence of the optical bistability. Details are to be found in sec. 14.2. Note that recombination does not necessarily end up in the exact Rydberg state that is addressed by the lasers. Instead, the atoms end up in a broad distribution of several states which then subsequently decay, cf. fig. 11.3. Therefore, this decay does not contribute to the population of the Rydberg state. It is rather directly added to the ground state, in order to achieve atom number conservation.

The interaction between the ensemble of Rydberg atoms and the plasma is the last part of L and is modeled as

$$L_3 = \begin{pmatrix} \Gamma_{\text{Ryd}}\rho_{\text{Ryd}} & 0 & -\frac{1}{2}\gamma\rho_{1,3} & 0 \\ 0 & 0 & -\frac{1}{2}\gamma\rho_{2,3} & 0 \\ -\frac{1}{2}\gamma\rho_{3,1} & -\frac{1}{2}\gamma\rho_{3,2} & -\Gamma_{\text{Ryd}}\rho_{\text{Ryd}} & 0 \\ 0 & 0 & 0 & 0 \end{pmatrix}. \quad (14.7)$$

The rate Γ_{Ryd} includes the natural lifetime of the Rydberg state and transit time effects. Due to the longevity of the highly excited states, the dominating part in thermal Rydberg experiments is the transit time decay Γ_t due to the finite size of the excitation beams. For our experimental setup and measurements, the beam sizes amount to $\Gamma_t/2\pi = 0.2$ MHz. The dephasing factor γ accounts for all line broadening mechanisms. Similarly to the ionization and de-ionization rates, the broadening also depends on the ion population. This is the second key aspect of the model, and will be described in sec. 14.3.

14.2 Ionization mechanisms

The two dominant mechanisms that we identified to be responsible for the ionization process are Rydberg-ground-state (fig. 14.1(b)) and Rydberg electron collisions (fig. 14.1(c)). The ionization rate, which accordingly must depend on the ion population ρ_{ion} , is given by

$$\Gamma_i(\rho_{\text{ion}}) = \mathcal{N}_g \sqrt{\frac{8k_B T}{\pi}} \left(\sigma_g \rho_g \sqrt{\frac{2}{m_{\text{Cs}}}} + \sigma_e \frac{\rho_{\text{ion}}}{\sqrt{m_e}} \right), \quad (14.8)$$

in which σ_g and σ_e are the ionization cross sections for Rydberg atoms colliding with ground state atoms and with electrons, respectively. Since the ground state density is not significantly influenced by the excitation, we take $\rho_g \approx 1$ in our model. We further neglect that the electron impact ionization cross section depends on the velocity of the electron [102]. In any case, since the relative variation of vapor temperatures is small, we assume that the ensemble average of impact velocities provides us with roughly the same outcome.

In a similar fashion, the rate

$$\Gamma_d(\rho_{\text{ion}}) = \Gamma_t + \mathcal{N}_g \sqrt{\frac{8k_B T}{\pi m_e}} \sigma_r \rho_{\text{ion}} \quad (14.9)$$

quantifies the mechanisms leading to losses in the ion population. The most obvious contribution is ions simply leaving the interaction volume due to their thermal motion which is described by Γ_t . The second term describes recombination of ions with electrons into neutral particles. It is basically the collision rate, eq. (1.77), weighted by the ion population, where the square-rooted term is the mean velocity. The transit time losses, Γ_t , are determined by the diameter of the excitation volume and the velocity of the particles. Note that the electrons on the one hand move much faster than the ions. This would result in a higher transit time rate. On the other hand, they are kept back by the electric potential caused by the ion excess. Therefore, we assume all charges to have the same transit time rates, which is that of the ions.

14.2.1 Fluorescence signal

The fluorescence flux is proportional to the electron density, multiplied with the recombination rate:

$$\Phi \propto \Gamma_r \mathcal{N}_e. \quad (14.10)$$

Recombined ion-electron pairs end up in a broad, discrete distribution of Rydberg states which then subsequently emit the fluorescence photons via their decay chain. Substituting the previous definition of the recombination rate (the second term in eq. (14.9)) and assuming that the electron density is approximately equal to the ion density, (cf. sec. 11.4.4) leads to the fluorescence signal being proportional to the square of the ion density,

$$\Phi \propto \rho_{\text{ion}}^2. \quad (14.11)$$

The fluorescence spectrum as measured in the experiment can thus be easily compared to simulated ion density spectrum.

14.2.2 Linearization of the recombination rate

As the distinction between a linear and quadratic component—such as in in eq. (14.9), which is quadratic in ρ_{ion} when substituted into eq. (14.6)—is not feasible for small parameter values, we reduce the complexity of the model by the following substitution. We replace the recombination term in eq. (14.9) with

$$\mathcal{N}_g \sqrt{\frac{8k_B T}{\pi m_e}} \sigma_r \rho_{\text{ion}} = \Gamma_r = \text{const.}, \quad (14.12)$$

and thereby assume Γ_d to be an effective ion-loss rate, with a constant value independent of the ion density. We also suppose ions to leave the beam geometry at the same rate Γ_t as Rydberg atoms, because their masses are equal and the Coulomb coupling in our experiment is weak, cf. sec. 3.1.2. These simplification enabled us to fit the parameters of the model to match simulated and measured spectra, as will be described in sec. 15.3.1.

14.3 Plasma broadening

The electric environment for the atoms during excitation by the lasers is subject to rapid changes as the atoms move through the plasma. The ionic background redistributes due to its own motion and therefore continuously samples different realizations of the Holtsmark distribution. The free electrons, traveling much faster than the ions, and also being influenced by their fields, further change the background on timescales much shorter

than the laser excitation dynamics. Each atom *sees* a different sequence of local electric fields, resulting in different accumulated phase shifts. As a result, the influence of the plasma needs to be considered two-fold: as a distribution of *average* detunings as well as an additional broadening due to the dephasing of the Rydberg transition [163]. The overall effect of the plasma is therefore implemented as an effective shift (covered by Δ_S in eq. (14.4)) and a homogeneous broadening. We define the overall dephasing factor as

$$\gamma = \gamma_0 + \gamma_S, \quad (14.13)$$

where γ_0 accounts for the laser line width and other parasitic broadening mechanisms. We assume $\gamma_0/2\pi = 1$ MHz. The effect of the Stark shift distribution is approximated to be proportional to its weighted mean

$$\gamma_S \propto \overline{\Delta_S} = \int_0^\infty dE \mathcal{P}_N(E) \Delta_S(E). \quad (14.14)$$

14.4 Converting electric fields into Stark shifts

Solving the Lindblad master equation requires knowledge about the detuning of the light fields. The crucial point of our model is to include the Stark shift of the Rydberg energy levels into the calculation. If the ionized fraction of an atomic ensemble is known, calculating the distribution of electric field strengths is uncomplicated. As discussed in sec. 3.2, the electric field composition of randomly positioned charges follows the Holtsmark distribution. The subsequent mapping of these electric fields to energy shifts that are useful for the calculations is a more elaborate procedure, and was implemented as follows.

Figure 14.2 shows computed Stark maps for cesium. One can see that the $42D_{5/2}$ state starts as a degenerate manifold of magnetic sub-levels m_J , that splits up for higher electric field values. Close by, at approximately $\Delta_S/2\pi = -1$ GHz, also the $42D_{3/2}$ state is located, which will not be further considered. Since the addressed state is a D state, the electric field direction (with respect to the laser polarization direction as the quantization axis) becomes relevant. With this choice of the quantization axis and due to dipole selection rules when no additional electric fields are present, driving the transition to the $42D_{5/2}$ state with a linearly polarized laser beam couples only to the $m_J = \pm 1/2$ sub-level. This becomes also apparent in the first panel, fig. 14.2(a), where the angle between electric field and quantization axis is set to zero. The color code here shows that only the top most branch overlaps with the $42D_{5/2}$ $m_J = 1/2$ state. For increasing angles, α , the admixed overlap is more and more biased towards the other available sub-levels. As expected for $\alpha = 45^\circ$, fig. 14.2(b), the *unrotated*¹ $m_J = \pm 3/2$ branch now has dominant contribution,

¹“Unrotated” refers to the basis states for $\alpha = 0^\circ$.

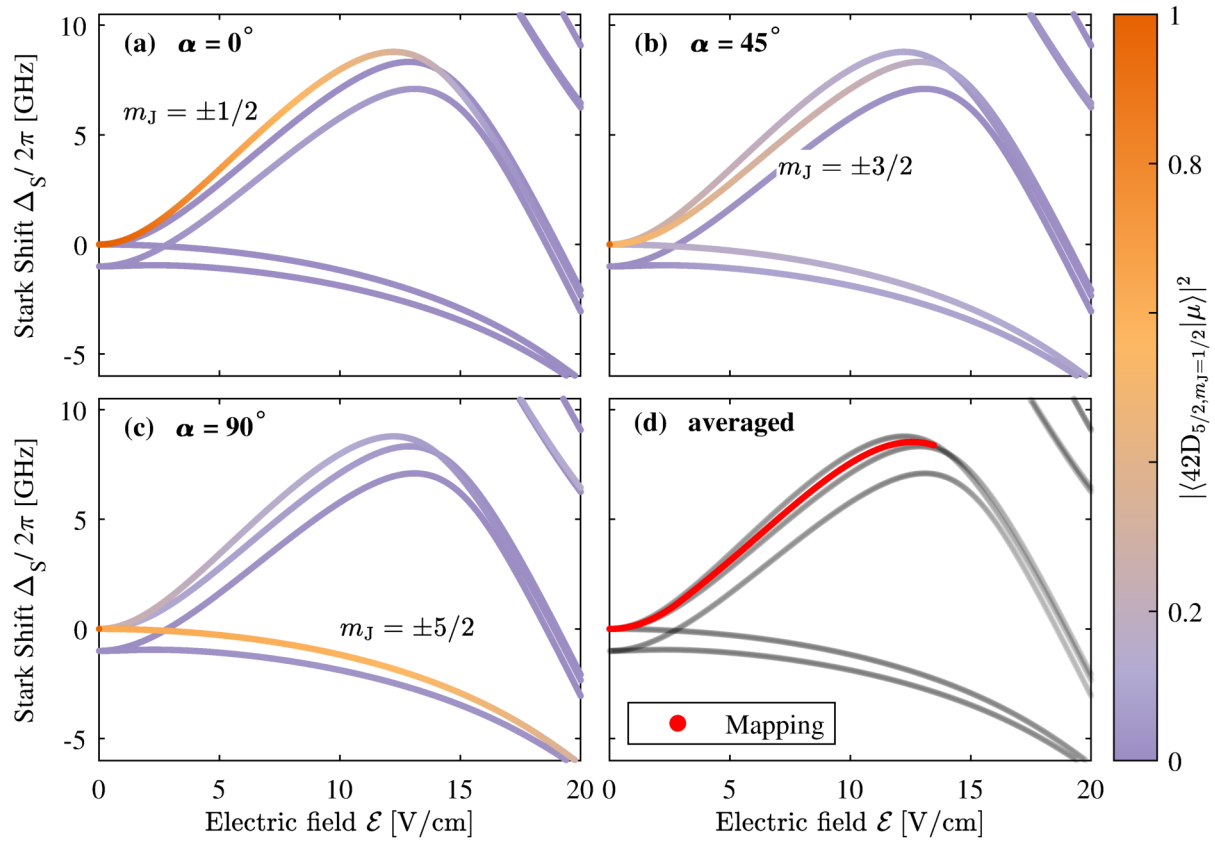


Figure 14.2: Stark map of the 42D states in cesium showing the angular dependency of the electric field. Visible in all panels are the $42D_{5/2}$ state manifold, starting at zero field, and the neighboring $42D_{3/2}$ at an offset of approximately -1 GHz. In the top right corner, the high- L manifold appears. (a-c) Projection of the $42D_{5/2, m_J=1/2}$ on the Stark-shifted manifold for different angles between laser polarization and electric field direction. The overlap (displayed in the color map) measures the relative excitation strength by the laser. Since the electric field direction is randomly distributed in the plasma, the mapping between electric field strength and effective Stark shift for the simulation is calculated by integrating over all possible angles. (d) The mapping used for the simulation, following eq. (14.16).

while for $\alpha = 90^\circ$, fig. 14.2(c), the (unrotated) $m_J = \pm 5/2$ branch is coupled the most. The calculation method is equivalent to rotating the atomic basis to the direction of the electric field, and projecting the laser polarization.

Since the charges are located at random positions also the electric field direction is random. We account for this by integrating the Stark maps for all possible angles, weighted by the respective overlap with the initial $42D_{5/2}$, $m_J = 1/2$ state. Because the $m_J = \pm 5/2$ branch is well separated from the two others and also shifts towards red detunings, we only sum over those states μ that contribute with a blue detuning Stark shift

$$\Delta_S(E) = \int_0^{2\pi} d\alpha \sum_{\mu} \left| \langle 42D_{5/2}, m_J = 1/2 | \mu \rangle \right|^2 \Delta_S(E, \alpha), \quad (14.15)$$

where the overlap factor is assumed to be normalized to the contributing branches. The result of eq. (14.15) is plotted in fig. 14.2(d).

The Stark shift for zero field vanishes, and is supposed to start as a quadratic function, sec. 2.2. For higher fields, the admixture of the different m_J sub-levels, and other energy levels start to contribute. For the simulation, we map the Stark shift as a function of the electric field with the following semi-analytic approximation using a piece-wise defined polynomial,

$$\Delta_S(E) = \begin{cases} p_1 E^2 & \text{for } E < E_t \\ p_1 E_t^2 + p_2(E - E_t) + p_3(E - E_t)^2 + p_4(E - E_t)^4 & \text{otherwise.} \end{cases} \quad (14.16)$$

Above a certain threshold, E_t , the shift continues as a linear function with quadratic and cubic correction terms. The parameters for the angular average of the $42D_{5/2}$ state, when only considering the *positive* branch of the m_J sub-levels, are obtained by least-square fitting, and result in $p_1/2\pi = 0.1462 \text{ GHz}/(\text{V}/\text{cm})^2$, $p_2/2\pi = 0.849 \text{ V cm}^{-1}$, $p_3/2\pi = 2.417 \times 10^{-2} \text{ GHz}/(\text{V}/\text{cm})^2$ and $p_4/2\pi = -3.585 \times 10^{-4} \text{ GHz}/(\text{V}/\text{cm})^4$. The interval of electric field strengths with a purely quadratic Stark shift goes up to $E_t = 2.856 \text{ V cm}^{-1}$.

As a sanity-check, the polarizability of the Cs $42D_{5/2}$ state for the sub-level $m_J = 1/2$ is $\alpha_{1/2}/2\pi = -0.34 \text{ GHz}/(\text{V}/\text{cm})^2$ while that of the $m_J = 3/2$ sub-level amounts to $\alpha_{3/2}/2\pi = -0.26 \text{ GHz}/(\text{V}/\text{cm})^2$ [47]. The obtained value for p_1 therefore agrees with the average of the two, $p_1 \approx -\frac{1}{2} \frac{(\alpha_{1/2} + \alpha_{3/2})}{2}$, considering the definition of the Stark shift's sign and coefficient, eq. (2.11).

For electric field strengths above $E_{\text{max}} = 13.5 \text{ V cm}^{-1}$, the Stark map appears to be too disturbed by admixture to justify the one-to-one mapping as described in this section. Values above E_{max} are cut off the mapping and are ignored in the simulation. For ion densities of up to $0.01 \mu\text{m}^{-3}$, more than 98% of the electric field distribution are below

the cut-off field. We later find that the peak ion density that appears in the simulation is only $0.003 \mu\text{m}^{-3}$, sec. 15.3.2.

14.5 Iterative algorithm

Obtaining the steady state solution for the entries of the density matrix in the Lindblad master equation, eq. (14.1), is straight forward, when all parameters in the Hamiltonian and the Lindblad operator have a given value; it simply requires the diagonalization of the resulting *linear* system of equations. Even the exact analytic solution to this problem is quickly found with the help of modern technical computing systems, such as Wolfram Mathematica. In this case, however, the parameters need to be considered to be variable, but independent of each other. The computational challenge now arises from the *non-linear* feedback due to the ion density, ρ_{ion} , which influences the electric field distribution—and hence the values of the detuning distribution and broadening—and the ionization rate. In order to calculate the actual ion density as a function of the detuning Δ_{R} and for a given set of experimental parameters (Ω_{B} , Ω_{R} , atomic density, temperature,), an iterative approach proves beneficial: Assuming an initial ion density defines the missing parameters required for the analytic solution to eq. (14.1). With this set of values, a steady state solution of the master equation is then obtained. This yields an updated ion density

$$\mathcal{N}' = \rho_{\text{ion}} \mathcal{N}_{\text{g}}, \quad (14.17)$$

which in turn is then used again as the assumption for a subsequent calculation. The equations are solved iteratively using the previous calculation of the ion density as an input parameter for subsequent computation steps. This procedure is repeated until the system has converged to an overall equilibrium solution, shown in fig. 15.1. A flow-chart summarizing this algorithm is shown in fig. 14.3.

14.5.1 Damping overshoots and oscillations

The model calculation exhibits oscillations around the equilibrium and is subject to overshoots, as will later be shown in fig. 15.1. To minimize these effects, the updated ion density after each iteration step is a modification of eq. (14.17). Instead of the direct updated value, we use the biased weighted average of the update and the previous step,

$$\mathcal{N}' = \beta \rho_{\text{ion}} \mathcal{N}_{\text{g}} + (1 - \beta) \mathcal{N}. \quad (14.18)$$

The actual choice of the damping β is not crucial for the computations, as it mostly affects the number of iterations required to reach equilibrium. By changing the parameter after reaching the equilibrium to $\beta = 1$, the system does not change further.

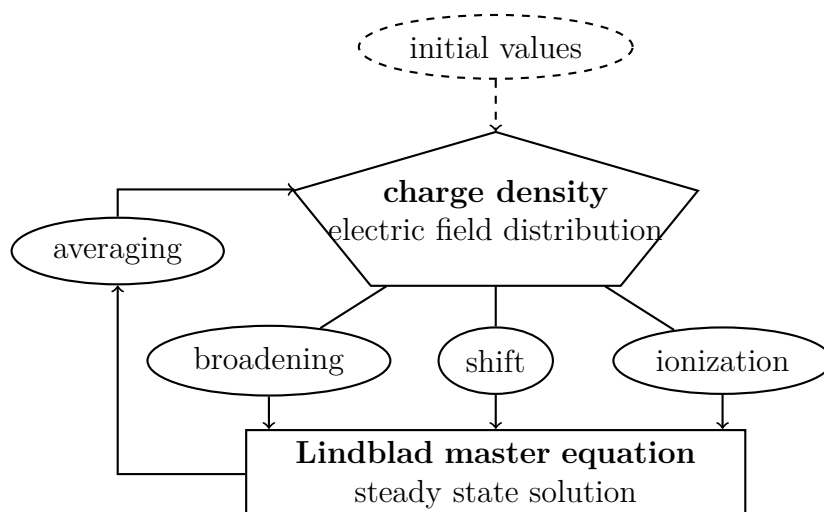


Figure 14.3: Flow chart of the iterative algorithm leading to an overall convergence. The current ion density determines the electric field distribution, and hence the broadening and shift of the Rydberg energy level. The charge density also influences the ionization rate. With these values, the ensemble of updated steady-state solutions of the master equation is calculated. When averaged over all velocity and electric field components, an improved estimation of the ion density at each laser detuning is achieved. The procedure is repeated until the system converges to a steady-state solution.

14.5.2 Numerical parameter

We compute our results for the simulation with the following numerical settings : The detuning $\Delta_R/2\pi$ ranges from -550 to 1250 MHz in 396 steps, providing a resolution of $2\pi \times 4.5$ MHz. The velocity vector contains $\pm 2\delta_D$ ($\approx \pm 800$ m s $^{-1}$) in 5001 entries, where δ_D is the Doppler width, eq. (1.70). The natural line-width of the $7P_{3/2}$ state is thereby resolved by $\mathbf{k}_B \cdot \mathbf{v}$. The electric field is separated into 501 steps, going from zero field up to $15Q_H$. The numerical values depend on the current ion density. In this configuration, the steady state solution of the Lindblad master equation is evaluated 10^9 times per iteration. We further set the damping to $\beta = 2/3$ and calculated for a fixed number of 200 iterations. Apart from a few very rare exceptions the relative change in the ion density after this number of iterations is well below 1×10^{-9} . Such exceptions occur when one of the discrete detuning values at which the system is evaluated lies in too close proximity to the actual edge frequency. This is related to the retardation of the convergence, which will be discussed in sec. 15.2.

15 Results and discussion

15.1 Convergence and hysteresis

The obvious choice for an initial ion density to begin the iterative convergence process, fig. 14.3, is to start from zero,

$$\rho_{\text{ion}}(\Delta_{\text{R}}) = 0, \forall \Delta_{\text{R}}. \quad (15.1)$$

This resembles the case of the Rydberg laser being scanned *towards* the resonance, in positive as well as in negative direction. Far off-resonant, the system naturally starts without any charges present, as previously no Rydberg excitations have happened. Applying the iterative algorithm then leads to a convergence sequence, as plotted in fig. 15.1 in purple.

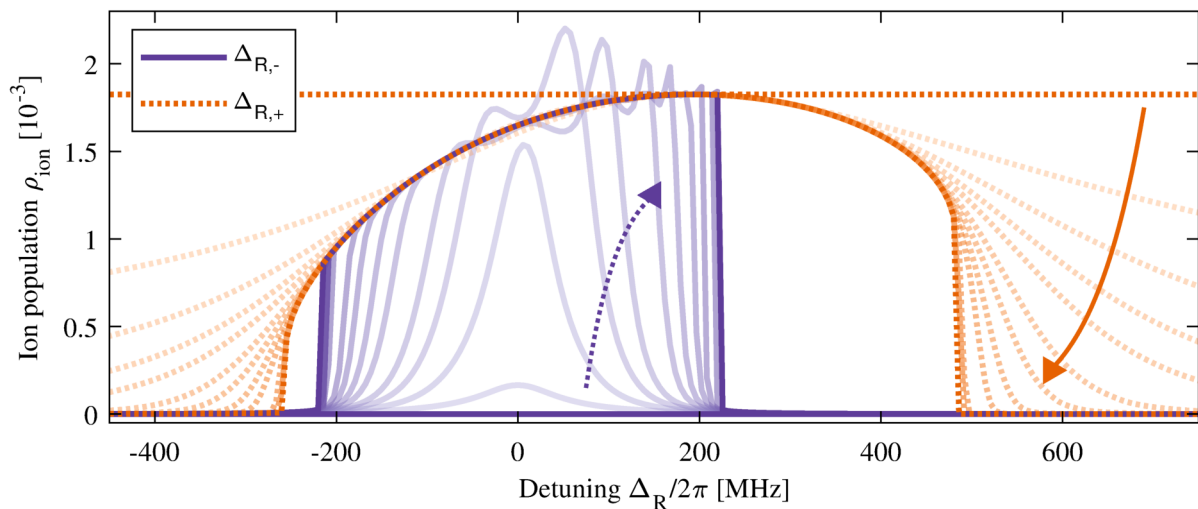


Figure 15.1: Convergence behavior of the iterative algorithm. The purple family of curves $\Delta_{\text{R},+}$ shows how the ion population converges upwards when initialized with zero density. As indicated by the dashed arrow, the feature starts as a narrow peak, that increases and broadens with each iteration step. It converges to the box-like solution plotted in dark purple. The orange dashed curves $\Delta_{\text{R},-}$ are the equivalent when starting from the high population state. Beginning with a large ion population, the feature is initially extremely smeared out. With each iteration step, the feature becomes more narrow, while also converging to a steady state solution. Interpreting the spectrum as if captured by a detuning scan, the difference between the two final curves resembles the hysteresis of the optical bistability.

When the lasers are scanned away from resonance, charges are still present in the system from the situation immediately before. Therefore, we calculate a second equilibrium, this

time starting from a non-zero ion density as the initial configuration. For all detunings of one spectrum, we use the maximum value of the previously calculated equilibrium spectrum that was initialized with zero charges,

$$\rho_{\text{ion}}(\Delta_{\text{R}}) = \max \rho_{\text{ion,ss}}(\Delta_{\text{R}}), \forall \Delta_{\text{R}}. \quad (15.2)$$

The iteration progresses as shown with the dashed orange lines in fig. 15.1.

It is apparent that for certain detuning values, the two different initial configurations lead to two different equilibrium solutions. Interpreting the spectrum as if captured by a detuning scan, the difference between the two curves resemble the hysteresis that occurs for parameters where one can observe the optical bistability. In order to map the two equilibrium solutions to the actual detuning sweep direction from the experiments, one has to consider that the laser is swept starting from negative end of the detuning-range *towards* resonance, but then continues *away* from the peak heading further to positive detuning value. At the positive end of the detuning range, the sweep direction is reversed, and the laser is again swept towards resonance, but this time in the negative direction. For the following plots, the equilibrium solutions for negative detuning values are interchanged. Thus, the orange traces resemble positive scan direction and the purple traces cover the negative sweep for all detuning values, in consistency with the color coding throughout this thesis.

15.2 Retardation of the convergence

Critical slowing down is a well-known indication for a phase transition [170, 171]. The temporal signature for switching between plasma and non-plasma state has been studied in detail in [32]. With our numerical approach, a corresponding signature in the convergence behavior can be observed: At careful inspection of the purple traces, fig. 15.1 reveals that for detuning values close to the edges of the transition significantly more iteration steps are required before the equilibrium is reached. The delay τ , defined as the number of steps required to reach 50% of the equilibrium value, diverges according to a power law

$$\tau \propto (\Delta_{\text{R}} - \Delta_{\text{E}})^{-\theta}. \quad (15.3)$$

Figure 15.2 shows the iterative progression of the ion density for different detunings. Fitting the exponent of the power law yields a value of $\theta = 0.5 \pm 0.3$. Our iterative approach therefore shows consistency in the convergence behavior with the direct measurements and matching predictions in [32, 172] of the *switching time*, and previous work on first-order phase transition and optical bistability [173, 174]. Note that a later study [165] did not confirm the algebraic divergence.

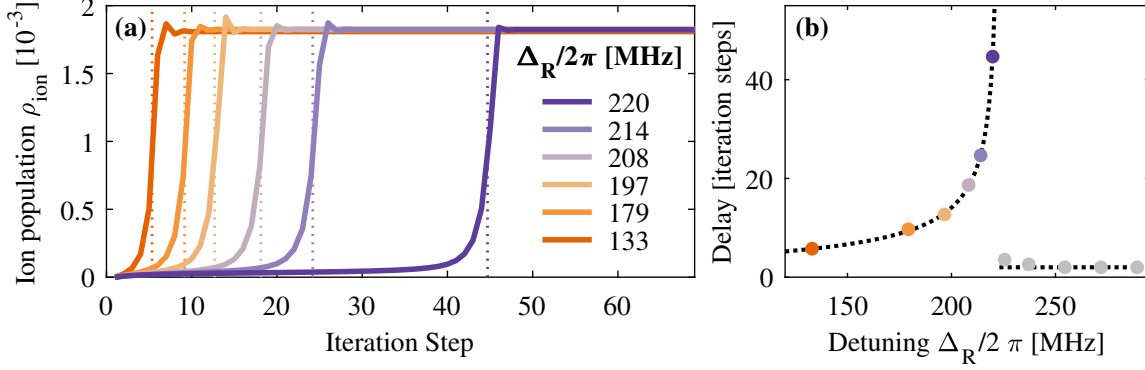


Figure 15.2: Critical slowing down revealed in the number of iteration steps required for the system to reach equilibrium. (a) The legend in MHz refers to the detuning values in fig. 15.1. The delay is indicated by the orange vertical lines, which signify when 50% of the equilibrium value is reached. (b) The delay diverges as $(\Delta_R - \Delta_{\text{crit}})^{-\theta}$. The black line shows the fit, which results in a critical exponent of $\theta = 0.5 \pm 0.3$.

In [32], the critical exponent with respect to the *intensity* as the control parameter is studied. The analysis in this section refers to the *detuning* from the edge position. These two are, in fact, interchangeable, which has been demonstrated in sec. 11.4. The edge position, Δ_E , scales linearly with the Rabi frequency, i.e., with the square root of the laser intensity. A sweep of the laser intensity therefore effectively sweeps Δ_E , instead of Δ_R . Note that the convergence behavior of our iterative approach has no *obvious* relation to the actual dynamics of the physical system. The iteration steps are nevertheless—in some way—related to time steps of the physical system. It is a nice accompaniment that the critical slowing down also has its appearance in the numerical model described in this thesis.

15.3 Comparison to the measured spectra

One of the incentives for the numerical model was to provide a *physically sensible* description of the phenomena and mechanisms that are related to the observation of measurements, such as shown in fig. 11.7. Many of the parameters are directly imposed by the experimental settings (Δ_1, Δ_2, T) or derived from known context $(\Omega_B, \Omega_R, \mathcal{N}_g, \Gamma_t, \Gamma_{\text{Ryd}})$. Others are well-established literature values $(m_e, m_{\text{Cs}}$ and the physical constants). The degrees of freedom of our model are expressed in the following four parameters:

- i. σ_e , electron impact ionization cross-section, eq. (14.8),
- ii. σ_g , ground state collision ionization cross-section, eq. (14.8),
- iii. Γ_d , effective de-ionization/recombination rate, eq. (14.12), and
- iv. γ , dephasing rate, eq. (14.14).

Except for γ , which is an empirical relation between the Stark shift distribution and the effective dephasing, these parameters can, in principle, be independently verified with suitable measurements. Note that Γ_d also depends on the geometry of the lasers.

Figure 15.3 shows the simulated spectra from the model overlaid with the measured data as described in the previous part. We achieve remarkable agreement between the calculations and the measurements, by fitting the four degrees of freedom of the model to the measured data as described in next paragraph. The spectral broadening and the line shape are described well, and the hysteresis feature is correctly reproduced for both positive and negative detuning sweeps of the Rydberg laser.

15.3.1 Parameter estimation by least-square optimization

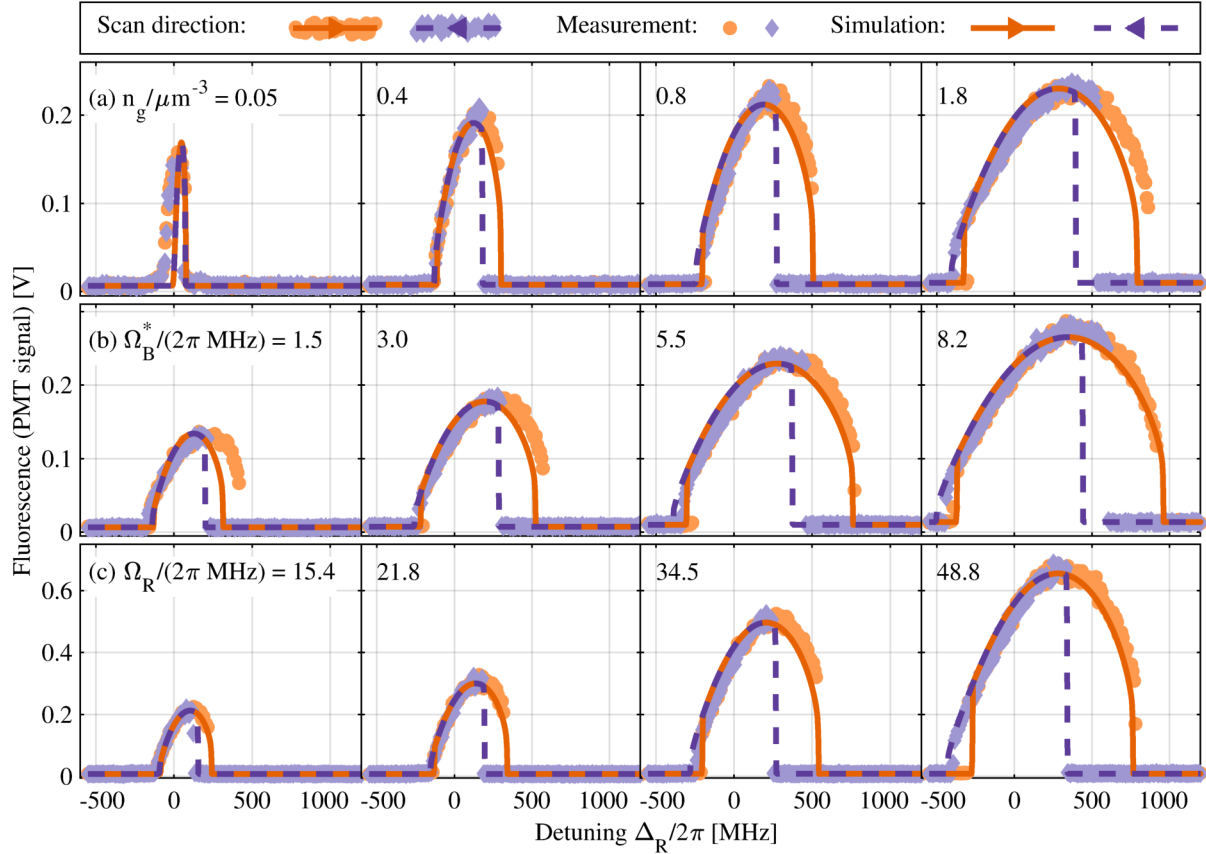
The values we obtain for our model are refined to the actual measurements via non-linear least-squares optimization. For this, we assume suitable initial values, and optimize the matching between simulated and measured spectra, $S(\Delta_R, \mathbf{p}, \mathbf{c}_k)$ and $M(\Delta_R, \mathbf{p}_k)$, using the Levenberg-Marquardt method [175, 176]. The cost function \mathbf{C} we minimize is defined by the vector components

$$C_k = \sum_{\Delta_{R,\pm}} (S(\Delta_R, \mathbf{p}, \mathbf{c}_k) - M(\Delta_R, \mathbf{c}_k))^2, \quad (15.4)$$

introducing \mathbf{p} and \mathbf{c}_k , which are the array of parameters (i - iv), $\mathbf{p} = (\sigma_e, \sigma_g, \Gamma_d, \gamma)$, and the array containing the experimental configurations, $\mathbf{c}_k = (\Omega_{B,k}^*, \Omega_{R,k}, \mathcal{N}_{g,k})$, respectively. The index k denotes the particular configuration. We chose a subset of $k = 1..12$ configurations in order to cover a wide range of experimental settings, with $\Omega_B^*/2\pi$ ranging from 1.5 to 8.2 MHz, $\Omega_R/2\pi$ from 15 to 50 MHz, and densities between 0.05 and 1.8 cm⁻³.

Summation in eq. (15.4) is performed over the discrete detunings for both detuning sweeps, $\Delta_{R,-}$ and $\Delta_{R,+}$. For the negative scan direction we excluded the values close to the plasma formation edge, $\Delta_{R,-} > 0$. The steep waveform has a disproportionate contribution to the overall error measure. Also the point of plasma formation is prone to additional uncertainties, such as, fluctuations in the electron density near the cell walls which can trigger the formation of the plasma state. Furthermore, as previously shown in fig. 11.9, the edge frequency for the plasma formation point depends on the raw Rabi frequency while the line shape of the system is defined by the *adjusted* Rabi frequency.

Since the numerical optimization requires multiple calculations of the complete model, we reduce the computational load by reducing the resolution of the model. We first optimize with 3001 velocities, 312 detuning values, 301 fields and 150 iterations, for an initial estimate of the parameters, and then refine the results with the full resolution,



Note that in the first row, Ω_B^* depends on the density. We count the 12 different settings row-wise when referencing by index.

Figure 15.3: Comparison between fluorescence measured as a function of the Rydberg laser detuning and calculations. Each row shows the variation of only one experimental parameter: ground state atomic density (a), Ω_B^* (b), and Ω_R (c). The measurement is shown in orange dots (scan from red towards blue wavelengths) and purple diamonds (scan from blue towards red wavelengths). For the simulation we use orange solid and dashed purple lines, respectively. Experimental settings are used as input parameter for the simulation. The fluorescence signal amplitude is adjusted for each trace individually. The detuning was offset for all 12 traces with the same value, to compensate for the side-of-fringe lock of the Rydberg laser. Experimental settings are: (row a) $\Omega_B/2\pi = 4.8$ MHz, $\Omega_R/2\pi = 15.4$ MHz (b) $\Omega_R/2\pi = 15.4$ MHz, $\mathcal{N}_g = 1.3 \times 10^{12}$ cm $^{-3}$ (c) $\Omega_B^*/2\pi = 4.8$ MHz, $\mathcal{N}_g = 0.2 \times 10^{12}$ cm $^{-3}$.

cf. sec. 14.5.2. The final set of parameters that we obtain by the optimization routine are summarized in tab. 15.1.

Var.	Fit result	Expect. value	Ref.
Γ_d	$(3.21 \pm 1.55) \Gamma_t$	$2 \Gamma_t$	sec. 15.3.2
γ_S	$(1.69 \pm 1.00) \overline{\Delta_S}$	$1 \overline{\Delta_S}$	eq. (14.14)
σ_g	$(0.04 \pm 0.04) \sigma_{\text{geo}}$	$0.06 \sigma_{\text{geo}}$	[35, 177]
σ_e	$(1.10 \pm 0.55) \sigma_{\text{geo}}$	1 to 10 σ_{geo}	[101]

Table 15.1: Fitted parameters with 95% confidence intervals from the non-linear least-squares optimization, and expected values derived from other references. The large error estimation stems from the correlation between the parameters.

15.3.2 Plausibility of the obtained values

Comparing the measured spectra to the simulated detuning traces shows compelling resemblance. This partly comes at the price that the model is not a true *ab-initio* calculation of the underlying system, as it comprises of four fitted parameters. In the following, we discuss the plausibility of the obtained values for these parameters.

Ground state scattering ionization

The ionization cross-section of Rydberg atoms colliding against ground state atoms, measured as a fraction of the geometric cross section, comes out as

$$\sigma_g = (0.04 \pm 0.04) \sigma_{\text{geo}}, \quad (15.5)$$

in very good agreement with the expected figure of $0.06 \sigma_{\text{geo}}$ [35]. A coarse estimate for this value was also obtained in the first experimental part of the thesis, sec. 7.1.5. Without considering the electron impact ionization, we obtained $0.18 \sigma_{\text{geo}}$, which is on a similar order.

Electron scattering ionization

The ionization cross section of the electron-Rydberg collisions also yields a reasonable value, with $\sigma_e = (1.10 \pm 0.55) \sigma_{\text{geo}}$. Since we did not find suitable reference values for cesium, experimental reference is taken from [101]. Here, the measurements predict cross-sections of up to $20 \sigma_{\text{geo}}$ near threshold, but with a strong dependence on the kinetic energy of the electron impact. Our value being only slightly larger than the geometric cross

section is attributed to the fact that we only see the integrated ionization probability: the average over the thermal ensemble also encloses contributions from higher energy impacts with a smaller cross section.

Dephasing

We attribute the additional dephasing to rapid changes in the electric field distribution. The dephasing rate was assumed to be proportional to the weighted mean of the Stark shift distribution, eq. (14.14). Note that for a purely quadratic Stark shift, this integral does not converge, due to the asymptotic behavior of the Holtsmark distribution, eq. (3.35). Even for the effective mapping, $\Delta_S(E)$, convergence is poor. The actual numerical value of the dephasing rate, $\gamma_S = (1.69 \pm 1.00) \overline{\Delta_S}$, depends on the electric field range that is considered for the calculation. This leads to a systematic error for the determination of γ_S . Nevertheless, the fit error margin is larger than the deviation from the assumed model.

Recombination

Given the range of experimental settings, cf. fig. 15.3, the photon flux emitted due to plasma recombination can be estimated and compared to the simulated situation. For this quantitative analysis, we assume a monochromatic fluorescence spectrum at 600 nm. On the experimental side, the PMT at this wavelength has a sensitivity of 1.89 V nW^{-1} and provides signal heights between 0.1 and 0.7 V. Given the collection efficiency of the lens system capturing the fluorescence, cf. sec. 10.2, this corresponds to an emitted power of approximately 70 to 360 nW, or a photon flux of

$$\Phi_{\text{exp}} = 0.2 \text{ to } 1.1 \times 10^{12} / \text{s}. \quad (15.6)$$

For the simulation side, we calculate the number of ions in a sphere with a diameter of 1.5 mm, which is approximately the volume we collect photons from. The maximum ion densities $\mathcal{N}_g \cdot \rho_{\text{ion}}$ for each simulated detuning trace are between 0.25 and $2.75 \times 10^9 / \text{cm}^3$. The fluorescence is then obtained by multiplying this number with the de-ionization rate reduced by the transit time losses. We end up with a simulated photon flux of

$$\begin{aligned} \Phi_{\text{sim}} &= \frac{4\pi}{3} (0.75 \text{ mm})^3 \mathcal{N}_{\text{ion}} \cdot (\Gamma_d - \Gamma_t) \\ &= 0.2 \text{ to } 2.1 \times 10^{12} / \text{s}. \end{aligned} \quad (15.7)$$

These two ranges are in agreement, making the obtained value for Γ_d perfectly plausible. Values for all 12 simulated configurations (fig. 15.3) are displayed in fig. 15.4.

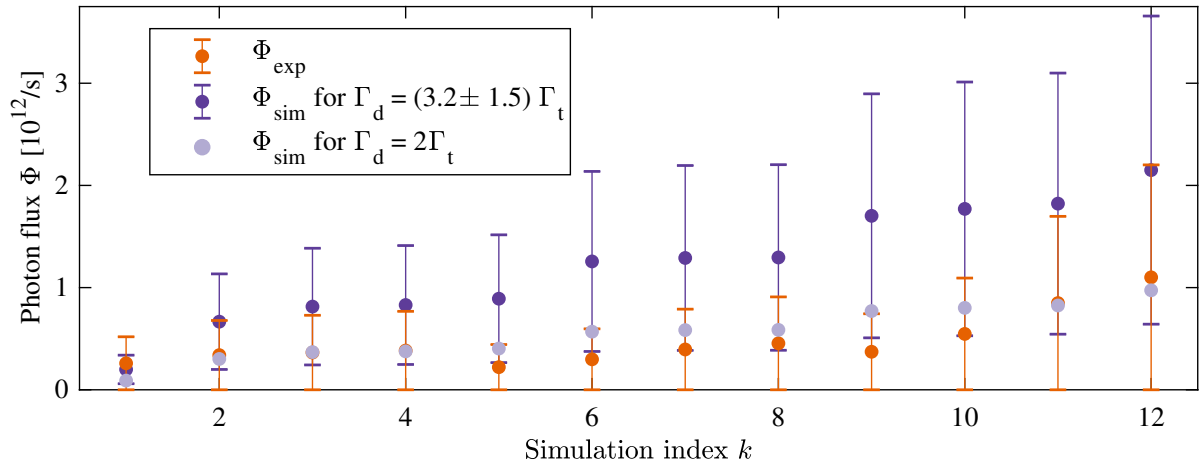


Figure 15.4: Comparison between peak photon fluxes derived from measured and simulated data. With our final value for the parameter, the results are within the expected order of magnitude. $\Gamma_d = 2\Gamma_t$ would improve the matching. Error estimate for Φ_{exp} is dominated by the uncertainty of the photon collection efficiency of the setup, which is assumed to be $(0.1 \pm 0.1)\%$ of the emitted photons.

15.4 Further discussion

15.4.1 Scaling behavior

We now apply the same analysis as performed in sec. 11.4.3 to the simulated data. Again, the two scaling parameters, S_{\downarrow}^* and S_{\uparrow} , are computed with the fitting method previously described. The resulting exponents are summarized in tab. 15.2. For S_{\downarrow}^* , all three expo-

	(Scan)	a (\mathcal{N}_g)	b ($\Omega_B^{(*)}$)	c (Ω_R)
Simulation				
S_{\downarrow}^*	(\rightarrow)	0.56 ± 0.04	0.59 ± 0.04	0.91 ± 0.06
S_{\uparrow}	(\leftarrow)	0.47 ± 0.04	0.44 ± 0.03	0.67 ± 0.07
Measurement				
S_{\downarrow}^*	(\rightarrow)	0.54 ± 0.01	0.56 ± 0.01	0.97 ± 0.02
S_{\uparrow}	(\leftarrow)	0.81 ± 0.01	0.95 ± 0.02	1.08 ± 0.02

Table 15.2: Scaling exponents for the simulated edge positions. For S_{\uparrow} , we recalculated the spectra with Ω_B instead of Ω_B^* . Given errors are 95% confidence intervals from the fit.

nents are in agreement with the ones obtained from measurements, cf. tab. 11.1. This was expected, because the overall line-shape of the measurements is well reproduced in all 12 simulated configurations. For S_{\uparrow} , we obtain different exponents. An indication for this is that the rising edge positions are not reliably predicted by the simulation, cf. fig. 15.3:

For the scans of density and blue Rabi frequency (row a and b) the simulated edge happens *too late* in the detuning sweep. One possible explanation is the linearization of the quadratic ionization rate, cf. sec. 14.2.2. All three exponents $(a, b, c)_\dagger$ are—very roughly—off by a factor of 2. The simulation apparently does not reproduce the assumptions in this aspect, and further research is required.

Another possible, yet unlikely, explanation is as follows. As discussed in sec. 11.1, the condition for the phase transition needs to be fulfilled anywhere within the cell; the plasma will then quickly spread across the full length of the beams in the vapor. Other influences, such as electrons coming from the surfaces of the cell due to the photo-electric effect, could trigger the plasma formation *earlier* in the detuning sweep. This is not covered by the simulation.

15.4.2 Hysteresis on both sides

For an interaction that only shifts the energy levels, one could argue that one expects an effect for laser frequencies on that side of the resonance that is towards the direction of this shift. In fig. 4.2, where a negative interaction potential was assumed, the two curves on the opposite, positively detuned side are, indeed, identical. For certain experimental configurations of laser intensities and ground state density, however, a second, but weaker hysteresis feature on the seemingly *wrong* side of the spectrum appears. This effect has previously been observed [138, 146], but was only mentioned with a pending explanation. This missing explanation turns out to be straight forward, as the measurements shown in fig. 15.3 are—also this detail—reproduced by our model. Additionally to the shift, the feedback mechanism involves an increase in dephasing of the excited state. Hence, the resonance line suddenly becomes wider once a certain threshold density is reached. Obviously, such threshold can be reached on both sides of the resonance, which leads to the abrupt jumps in the spectra. Nonetheless, the Stark map of the $42D_{5/2}$ state, fig. 14.2, features a red shifting branch as well, and the $42D_{3/2}$ state is also in close proximity. However, both these aspects are disregarded in the modeled traces, but the feature is still reproduced correctly.

15.4.3 Quantitative assessment of the simulated system

As a final discussion of the results obtained with the model, we want to inspect other important properties of the simulated system. In analogy to the ion population ρ_{ion} , also the remaining entries of the density matrix can be calculated. Figure 15.5 shows simulated Rydberg and ion density traces for three exemplary parameter configurations. The graphs for the dephasing γ , and the ionization rate Γ_i (not shown here) follow almost the exact same shape as the ion density.

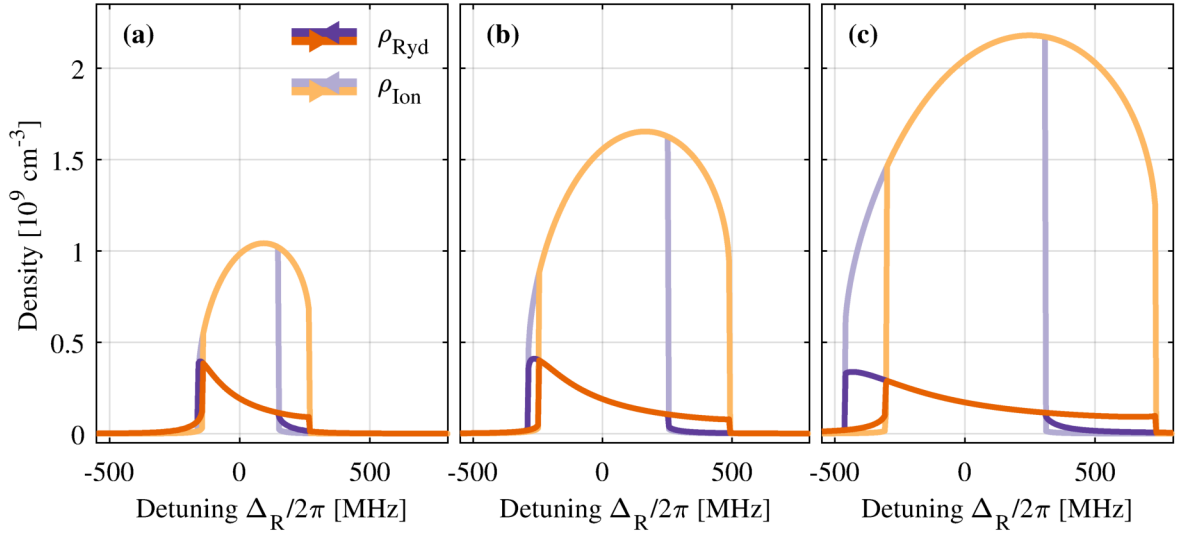


Figure 15.5: Simulated densities ($\mathcal{N}_g \cdot \rho$) according to the model. Settings, given in the order for (a / b / c): $\Omega_B/2\pi = (2.6 / 3 / 5.3)$ MHz, $\Omega_R/2\pi = (15.4 / 15.4 / 48.8)$ MHz, $\mathcal{N}_g = (0.4 / 1.3 / 0.2) \times 10^{12}/\text{cm}^3$, corresponding to $k = 2, 6$ and 12 in fig. 15.3. The dephasing and ionization rate follow the same shape as ρ_{ion} , with their maxima at $\gamma/2\pi = (0.4 / 0.7 / 1)$ GHz, and $\Gamma_i/2\pi = (2.8 / 4.8 / 5.8)$ MHz. Due to the feedback behavior of the system, Rydberg densities seem to be limited by an upper boundary, while the ion density further increases with increasing excitation rate. At large detunings, the Rydberg population is *increased* due to the presence of charges. On resonance, the Rydberg population is *suppressed*.

Ion density

Simulated ion densities follow the spectra as shown in fig. 15.5, with the squared ion density closely matching the shape of the measured fluorescence signals in fig. 15.3. The peak values for all simulated configurations are given in tab. 15.3.

Property	Unit	1	2	3	4	5	6	7	8	9	10	11	12
$\max \rho_{\text{ion}} \mathcal{N}_g$	$[10^9 \text{cm}^{-3}]$	0.3	1.0	1.6	2.3	1.1	1.7	2.3	2.8	0.9	1.1	1.7	2.2
$\max \rho_{\text{Ryd}} \mathcal{N}_g$	$[10^8 \text{cm}^{-3}]$	3.0	4.0	4.3	4.4	3.4	4.1	4.6	4.9	3.8	3.7	3.5	3.4
$\max \rho_{\text{Ryd,ref}} \mathcal{N}_g$	$[10^9 \text{cm}^{-3}]$	0.4	2.5	5.7	12.2	2.8	6.3	11.0	14.9	1.7	1.8	1.9	1.9

Table 15.3: Densities of ions and Rydberg atoms for the different simulated experimental configurations. $\rho_{\text{Ryd,ref}}$ is calculated for the simple three-level system without ionization and electric fields.

Quantitatively, the ion density can be compared to the estimates based on the plasma frequency measurements, shown in fig. 11.6. Since these measurements were taken with the Rydberg state $30D_{5/2}$ and the laser locked on resonance, the mapping between Stark map and effective shift, sec. 14.4, needs to be recalculated. The geometric cross-section is re-scaled with the principle quantum number. The remaining parameters, especially the

four model parameters from tab. 15.1, were not changed. For the experimental configurations shown in fig. 11.6, we calculate a range of ion densities $\rho_{\text{ion}} = 0.13$ to $2.2 \times 10^{10}/\text{cm}^3$, but measure a range of electron densities $\rho_{\text{ion}} = 0.47$ to $7.5 \times 10^8/\text{cm}^3$. This is off by a factor of approximately 30. One possible explanation could be that in the experiments, the RF related measurements do not probe the electron density within the cross section of the laser beams only, but in the whole cell volume instead. Ions and electrons certainly diffuse outwards, which is not captured by the simulation. The ratio between the area of the beams and the cell is 65, which would correspond to the number of electrons within the beam profile expanded to the whole cell. Another explanation could be that the model parameters can not simply be applied to other experimental configurations. Note that the set of parameters was obtained for the $42D_{5/2}$ Rydberg state, here we compare to $30D_{5/2}$. Further development of the model for reliable density estimates is necessary.

Rydberg density

The Rydberg density is qualitatively very different from the ion density. Its maximum values lie close to the edges on the red detuned side, with a decrease of population all the way towards the edge on the blue detuned side. As the ionization rate due to electron collisions and the additional broadening is proportional to the ion/electron density, the equilibrium Rydberg population is suppressed for higher ρ_{ion} values. Apparently, a larger portion of atoms ends up in the plasma phase instead of the Rydberg state.

When driving the atomic ensemble at detunings Δ_R larger than the power broadened linewidth of the transition, the additional dephasing due to the plasma has the opposite effect: the charges lead to an increase of the excited state population, because now the Lorentzian wings of line profile extend further towards the laser frequency. Excitation thereby becomes possible where it would be highly unlikely without the broadening. Thus, the presence of charges acts as a facilitating feedback.

The peak value of the Rydberg density for all 12 simulated configurations (cf. fig. 15.3), ranges from 3 to $4.9 \times 10^8/\text{cm}^3$, as listed in tab. 15.3. Without the ionization mechanism (calculating the regular, Doppler averaged three-level system) the estimated peak Rydberg density amounts to values in the range from 0.4 to $15 \times 10^9/\text{cm}^3$ for the given experimental parameters. We now want to bring these numbers into line with literature reference: In the related cesium beam, pulsed laser experiment reported in [35], the authors provide a threshold value of $\approx 1 \times 10^{11} \text{ cm}^{-3}$ at which the onset of an ionized fraction of the vapor was detected. This value is by three orders of magnitude larger than our equilibrium result. Note that this experiment was conducted with pulsed lasers, and ionization was measured at a fixed delay *after* the Rydberg excitation. Most importantly, there is no atom light interaction anymore by the time when charges are present in the vapor. This crucial aspect fundamentally differs for continuous laser excitation experiments, where

atoms are continually excited with perturbing charges in close proximity. The atom light interaction in continuous laser beam experiments (after a short initialization time) takes place in an environment that is altered by the plasma. In steady state, this apparently leads to a significantly decreased upper boundary of the maximally achievable Rydberg density.

Simulation boundaries

In order for the simulation to provide meaningful results, the internal parameters need to stay within the defined boundaries. As listed in tab. 15.4, no excessive values occurred: The maximal Stark shift is below the maximum of the defined mapping of $2\pi \times 8.5$ GHz, cf. sec. 14.4, and the ionization rate $\Gamma_i/2\pi$ is below 8 MHz, which seems also plausible. The maximum dephasing, $\gamma_S/2\pi = 1.3$ GHz, is comparable to the width of the Doppler profile of the 455-nm laser, cf. eq. (1.69), which is $\delta_{D,455}/2\pi \approx 0.8$ GHz. The normalizing field $\mathcal{Q}_{\mathcal{H}}$, eq. (3.32), which gives the order of the field strength at the mean distance to the next ion divided by three, is only about 1 V cm^{-1} . Compared to the electric stray fields that are usually compensated for in cold atom experiments [178], these fields are only 10 times larger.

Property	Unit	1	2	3	4	5	6	7	8	9	10	11	12
$\max \gamma_S/2\pi$	[GHz]	0.1	0.4	0.7	1.1	0.4	0.7	1.0	1.3	0.3	0.4	0.7	1.0
$\max \Delta_S/2\pi$	[GHz]	0.7	3.9	5.7	7.5	3.9	5.8	7.4	8.2	3.2	4.2	5.8	7.2
$\max \Gamma_i/2\pi$	[MHz]	0.7	2.8	4.5	6.9	3.2	4.8	6.5	7.8	2.3	3.0	4.4	5.8
$\max \mathcal{Q}_{\mathcal{H}}(\rho_{\text{ion}}\mathcal{N}_g)$	[V cm ⁻¹]	0.2	0.4	0.5	0.7	0.4	0.5	0.6	0.7	0.3	0.4	0.5	0.6

Table 15.4: Occurring parameter maxima in the simulation. All values are within a reasonable range. The maximum value in each row is for $k = 8$.

16 Part IV: Conclusion

In this part of the thesis, we implement a numerical model based on the new insights into the mechanisms causing optical bistability in thermal Rydberg vapors. We model the atom-light interaction using the density matrix formalism, and consider the plasma as an additional, incoherently coupled addendum to a regular three level ladder system. The ionization mechanisms incorporated into the simulation are ground state and electron scattering. The latter depends on the charge density itself, which makes the non-linearity of this contribution obvious. With charges present in the vapor, the associated electric field distribution provides a feedback onto the detuning between the addressed Rydberg level and laser frequency. In analogy to Doppler averaging for the thermal distribution of velocities, we calculate the ensemble properties of the Stark shift distribution by integrating over the Holtsmark distribution of electric field strengths. While the ions in the plasma provide this electric field distribution, the faster electrons perturb the atom-light interaction on a much shorter timescale. This is implemented as an additional dephasing term.

The two stable states that the bistable system realizes for the two different detuning sweep directions are obtained by solving the Lindblad master equation for the steady-state solution, and iteratively approaching the equilibria. The plasma density of the previous step is used to calculate the Stark-shift distribution, ionization rate and dephasing for the current iteration step. By starting from two different initial conditions and the peak value of this equilibrium as the initial ion density for the second solution) the hysteresis in the measured fluorescence signal is reproduced. The simulation unveils even minute details of the system: Close to the critical detuning at which the system splits into two stable solution convergence slows down. This resembles critical slowing down related to a first order phase transition. Furthermore, also the second hysteresis that appears in the measurements is reproduced by the simulation.

The model is parameterized by four control variables, i.e., two cross sections for ground state and electron collisions, effective charge loss rate and the dephasing rate. With non-linear least square optimization, we adjust these four parameters to improve on the matching between simulated ion density and the measured fluorescence. The resulting values are plausible, and compare nicely to literature values and previous measurements. We thus achieve excellent agreement between the model and experiment, and confirm that the creation of a plasma is at the heart of optical bistability in thermal Rydberg vapor.

Summary

In the course of this thesis, we closely investigate on intrinsic optical bistability in thermal Rydberg vapors. The excitation of a gas of alkali atoms in a thermal vapor cell to a high lying state leads to the interesting effect: depending on the scan direction of the laser detuning, the spectrum one records can be significantly different. This is due to a feedback mechanism, that, depending on the density of either ions or Rydberg atoms, affects an energy shift and a broadening on the Rydberg state that is addressed. As a consequence, two stable states for otherwise identical configurations emerge: the system shows bistable behavior. Two competing interpretations of the phenomenon are available that both, in principle, are suitable to provide an explanation of the underlying mechanisms that lead to the bistability. On the one hand, Rydberg-Rydberg interactions could provide the necessary non-linearity and feedback mechanism. On the other hand, we suggest that ionized Rydberg atoms create an electric field distribution in the vapor, that is responsible for the bistability via the Stark shift. The driving ambition for this thesis was to resolve the ambiguity of explanations.

In the first experimental part of the thesis, we have established a strong link between the phenomenon of optical bistability in thermal Rydberg vapors and the presence of charged particles in the gas. At the same time, we are able to deter Rydberg-Rydberg interactions as the dominant mechanism responsible for the interaction shift that causes the non-linear behavior. This is possible with the two complementary experiments that we realized. In the first experiment, we have applied two independent EIT schemes simultaneously, each addressing one of the naturally abundant isotopes of rubidium. The first scheme strongly drives the transition in ^{85}Rb , enabling the atoms to enter the bistable regime. At the same time, we monitor the effect on the ^{87}Rb atoms by the second EIT scheme. The observations we make are incompatible with Rydberg-Rydberg interactions, but instead agree also quantitatively with a Stark effect caused by electric fields originating from ionizing collisions of the Rydberg atoms. The estimated ion densities and the required ionization cross sections are within a sensible range. With the second experiment based on cesium vapor we are able to confirm our explanation: the bistable region in the spectrum follows the sign of the polarizability when addressing two different Rydberg states, one with positive and one with negative α . Also, applying weak electric field significantly alters the observed spectrum.

In part III, we have further developed on the awareness that charged particles are present under the experimental conditions at which one can observe optical bistability. We were able to confirm the natural supposition that the vapor of ionized Rydberg atoms indeed shows the characteristics of a plasma by directly measuring the plasma frequency.

Analyzing the fluorescence that is radiated sideways from the laser beam axis, literally enables a new perspective onto the subject. We propose that avalanche ionization due to Rydberg-electron collisions significantly contributes to the observed phenomena. We demonstrate that a single scaling parameter—which includes all our experimental parameters—describes the point of plasma formation. This scaling behavior agrees very well with an empirical rate model for the charge density.

Part IV concludes the experimental observations with a comprehensive model of the *atom-plasma-laser* system. We model the atom-light interaction using the density matrix formalism, and consider the plasma as an additional, incoherently coupled addendum to a regular three level ladder system. The ionization mechanisms incorporated into the simulation are ground state scattering and electron scattering. With charges present in the vapor, the associated electric field distribution provides a feedback onto the detuning between the addressed Rydberg level and laser frequency. In analogy to Doppler averaging for the thermal distribution of velocities, we calculate the ensemble properties of the Stark shift distribution by integrating over the Holtsmark distribution of electric field strengths. The model is parameterized by four control variables, i.e., two cross sections for ground state and electron collisions, effective charge loss rate and the dephasing rate. We adjust these four parameters to improve on the matching between simulated charge density and the measured fluorescence. The overlap between simulated and measured spectra is persuasive, the resulting values are plausible and compare nicely to literature and previous measurements. We thus demonstrate excellent agreement between the model and experiment, and confirm that the creation of a plasma is at the heart of optical bistability in thermal Rydberg vapor.

Conclusion and Outlook

By thorough investigation into ionization in thermal Rydberg spectroscopy, we have demonstrated an essential interplay between optical bistability and plasma formation. Our hypothesis, which is in contradiction to previous suppositions, was thereby reliably sustained by a series of experimental studies as well as a comprehensive numerical simulation. We established, that the threshold behavior as observed in the intrinsic optical bistability in thermal Rydberg vapor, is based on avalanche ionization. The ensuing vapor of charged particles shows the characteristics of a plasma, associated by a recombination spectrum that phenomenologically resembles the signature of a superradiant cascade.

Ionization of the Rydberg state population could potentially have an impact in many thermal vapor based experiments. Our findings emphasize that careful measures are required to operate in a regime where unwanted ionization can be unequivocally excluded. This is especially true for microwave and terahertz measurement schemes with an objective of traceability to SI-units. If not accounted for in a proper way, charged particles could pose a threat to reliable results or mislead to false conclusions. Accurate treatments and thorough consideration of the effects that ions and electrons have in the system are apparently inevitable. This is a very topical subject, now that Rydberg atom experiments in thermal vapor cells have become more and more fashionable over the past few years. A growing number of research groups all over the world is engaged in the exploration of quantum sensing protocols and cooperative effects based on Rydberg atoms.

Experiments with continuous excitation to Rydberg states are particularly compromised by ionization, because (after some initial time) the excitation dynamics thereby happens in the presence of electric fields. But also pulsed experiments are subject to stricter limitations, e.g., with respect to the pulse repetition rate. Remnant ions from previous pulses could still be present both in the vapor phase or on vapor cell surfaces, when the next pulse arrives. Ions acting as *seeds* can, in principle, facilitate the subsequent excitation dynamics [15, 179].

In light of the new perspective gained with this thesis, it might be worthwhile to re-evaluate measured data and conclusions from already published manuscripts. In references [15, 138, 180–184], the described experimental conditions—in terms of atom densities and laser powers—lie within the range that was investigated here. This suggests that ionization and thus an electric field distribution could potentially play a role. A closer look should reveal more insight, and help to eradicate any remaining concerns.

Preventive action to minimize the influence of ionization on Rydberg atoms—besides the obvious of reducing the laser powers to the necessary minimum—could be to extract the

appearing charges from the vapor, e.g., by means of electrically contacted field plates inside the vapor cell or pulsed electric fields. Being far off-resonant to the Rydberg state and pulsed laser excitation on timescales faster than the ionization collision dynamics are also available options. Exploiting transitions between Rydberg states with long wavelengths as a source for microwave radiation, e.g., in a pulsed six-wave mixing scheme [185], can thus still be a viable concept.

In this thesis, we provide a numerical model for the steady state situation. Future research could help to also simulate and understand the avalanche dynamics and the formation of the plasma. Also the recombination process and subsequent fluorescence is worth further inspection. Available methods from plasma physics could be beneficial tools for this [186]. Although many aspects of the simulated physical systems are already reproduced or included in our simulation, further development is necessary in order to provide more valuable insight. For example, the influence of the geometry of the vapor cell or the diameter of the laser beams are interesting questions waiting to be answered. Extending the simulation to different Rydberg states (S , P , \dots), different principal quantum numbers and different elements (Rb, Na, Li, \dots) would further increase the applicability of the model to other experimental scenarios.

Bibliography

[Citing pages are listed after each reference.]

- [1] Saffman, M. and Walker, T.G., Analysis of a quantum logic device based on dipole-dipole interactions of optically trapped Rydberg atoms, *Phys. Rev. A* **72**, 022347 (2005). [Pages 1 and 5]
- [2] Jones, M.P.A., Beugnon, J., Gaëtan, A., Zhang, J., Messin, G., Browaeys, A., and Grangier, P., Fast quantum state control of a single trapped neutral atom, *Phys. Rev. A* **75**, 040301(R) (2007). [Pages 1 and 5]
- [3] Löw, R., Weimer, H., Krohn, U., Heidemann, R., Bendkowsky, V., Butscher, B., Büchler, H.P., and Pfau, T., Universal scaling in a strongly interacting Rydberg gas, *Phys. Rev. A* **80**, 033422 (2009). [Pages 1 and 5]
- [4] Schauß, P., Zeiher, J., Fukuhara, T., Hild, S., Cheneau, M., Macrì, T., Pohl, T., Bloch, I., and Groß, C., Crystallization in Ising quantum magnets, *Science* **347**, 1455–1458 (2015). [Pages 1 and 5]
- [5] Dudin, Y. and Kuzmich, A., Strongly interacting Rydberg excitations of a cold atomic gas, *Science* **336**, 887–889 (2012). [Pages 1 and 5]
- [6] Peyronel, T., Firstenberg, O., Liang, Q.Y., Hofferberth, S., Gorshkov, A.V., Pohl, T., Lukin, M.D., and Vuletić, V., Quantum nonlinear optics with single photons enabled by strongly interacting atoms, *Nature* **488**, 57–60 (2012).
- [7] Maxwell, D., Szwer, D.J., Paredes-Barato, D., Busche, H., Pritchard, J.D., Gauguier, A., Weatherill, K.J., Jones, M.P.A., and Adams, C.S., Storage and control of optical photons using Rydberg polaritons, *Phys. Rev. Lett.* **110**, 103001 (2013).
- [8] Tiarks, D., Baur, S., Schneider, K., Dürr, S., and Rempe, G., Single-photon transistor using a Förster resonance, *Phys. Rev. Lett.* **113**, 053602 (2014).
- [9] Gorniaczyk, H., Tresp, C., Schmidt, J., Fedder, H., and Hofferberth, S., Single-photon transistor mediated by interstate Rydberg interactions, *Phys. Rev. Lett.* **113**, 053601 (2014). [Pages 1 and 5]
- [10] Faoro, R., Pelle, B., Zuliani, A., Cheinet, P., Arimondo, E., and Pillet, P., Borromean three-body FRET in frozen Rydberg gases, *Nat. Commun.* **6** (2015). [Pages 1 and 5]

- [11] Günter, G., Schempp, H., Robertde SaintVincent, M., Gavryusev, V., Helmrich, S., Hofmann, C., Whitlock, S., and Weidemüller, M., Observing the dynamics of dipole-mediated energy transport by interaction-enhanced imaging, *Science* **342**, 954–956 (2013). [Pages 1 and 5]
- [12] Barredo, D., Labuhn, H., Ravets, S., Lahaye, T., Browaeys, A., and Adams, C.S., Coherent excitation transfer in a spin chain of three Rydberg atoms, *Phys. Rev. Lett.* **114**, 113002 (2015). [Pages 1 and 5]
- [13] Schempp, H., Günter, G., Robertde SaintVincent, M., Hofmann, C.S., Breyel, D., Komnik, A., Schönleber, D.W., Gärttner, M., Evers, J., Whitlock, S., and Weidemüller, M., Full Counting Statistics of Laser Excited Rydberg Aggregates in a One-Dimensional Geometry, *Phys. Rev. Lett.* **112**, 013002 (2014). [Pages 1 and 5]
- [14] Malossi, N., Valado, M.M., Scotto, S., Huillery, P., Pillet, P., Ciampini, D., Arimondo, E., and Morsch, O., Full Counting Statistics and Phase Diagram of a Dissipative Rydberg Gas, *Phys. Rev. Lett.* **113**, 023006 (2014).
- [15] Urvoy, A., Ripka, F., Lesanovsky, I., Booth, D., Shaffer, J., Pfau, T., and Löw, R., Strongly correlated growth of Rydberg aggregates in a vapor cell, *Phys. Rev. Lett.* **114**, 203002 (2015). [Pages 1, 5, 22, 72, 73, and 137]
- [16] Bendkowsky, V., Butscher, B., Nipper, J., Shaffer, J.P., Löw, R., and Pfau, T., Observation of ultralong-range Rydberg molecules, *Nature* **458**, 1005 (2009). [Pages 1, 5, and 33]
- [17] Overstreet, K.R., Schwettmann, A., Tallant, J., Booth, D., and Shaffer, J.P., Observation of electric-field-induced Cs Rydberg atom macrodimers, *Nat. Phys.* **5**, 581 – 585 (2009). [Pages 1 and 5]
- [18] Sedlacek, J.A., Schwettmann, A., Kübler, H., and Shaffer, J.P., Atom-based vector microwave electrometry using rubidium rydberg atoms in a vapor cell, *Phys. Rev. Lett.* **111**, 063001 (2013). [Pages 1 and 5]
- [19] Wade, C.G., Marcuzzi, M., Levi, E., Kondo, J.M., Lesanovsky, I., Adams, C.S., and Weatherill, K.J., A terahertz-driven non-equilibrium phase transition in a room temperature atomic vapour, *Nat. Commun.* **9**, 3567 (2018). [Pages 1 and 5]
- [20] Ripka, F., Kübler, H., Löw, R., and Pfau, T., A room-temperature single-photon source based on strongly interacting Rydberg atoms, *Science* **362**, 446–449 (2018). [Pages 1, 5, 22, and 33]
- [21] Dehmelt, H., Slow spin relaxation of optically polarized sodium atoms, *Physical Review* **105**, 1487 (1957). [Pages 1 and 5]

- [22] Knappe, S., Shah, V., Schwindt, P.D., Hollberg, L., Kitching, J., Liew, L.A., and Moreland, J., A microfabricated atomic clock, *Applied Physics Letters* **85**, 1460–1462 (2004). [Pages 1 and 5]
- [23] Dicke, R.H., Coherence in spontaneous radiation processes, *Physical review* **93**, 99 (1954). [Pages 1 and 5]
- [24] Madjar, A. and Berceci, T., *Microwave generation by optical techniques-A review*, in *2006 European Microwave Conference*, 1099–1102. IEEE. [Pages 2 and 5]
- [25] Dhillon, S., Vitiello, M., Linfield, E., Davies, A., Hoffmann, M.C., Booske, J., Paoloni, C., Gensch, M., Weightman, P., Williams, G., et al., The 2017 terahertz science and technology roadmap, *Journal of Physics D: Applied Physics* **50**, 043001 (2017). [Pages 2 and 5]
- [26] Kimble, H.J., The quantum internet, *Nature* **453**, 1023 (2008). [Pages 2 and 5]
- [27] Saffman, M., Walker, T.G., and Mølmer, K., Quantum information with Rydberg atoms, *Reviews of Modern Physics* **82**, 2313 (2010). [Pages 2, 5, and 31]
- [28] Gross, M. and Haroche, S., Superradiance: An essay on the theory of collective spontaneous emission, *Physics reports* **93**, 301–396 (1982). [Pages 2 and 6]
- [29] Gross, M., Goy, P., Fabre, C., Haroche, S., and Raimond, J., Maser oscillation and microwave superradiance in small systems of Rydberg atoms, *Physical Review Letters* **43**, 343 (1979). [Pages 2 and 6]
- [30] Moi, L., Fabre, C., Goy, P., Gross, M., Haroche, S., Encrenaz, P., Beaudin, G., and Lazareff, B., Heterodyne detection of Rydberg atom maser emission, *Optics Communications* **33**, 47–50 (1980). [Pages 2 and 6]
- [31] Wang, T., Yelin, S., Côté, R., Eyler, E., Farooqi, S., Gould, P., Koštrun, M., Tong, D., and Vranceanu, D., Superradiance in ultracold Rydberg gases, *Physical Review A* **75**, 033802 (2007). [Pages 2 and 6]
- [32] Carr, C., Ritter, R., Wade, C., Adams, C.S., and Weatherill, K.J., Nonequilibrium phase transition in a dilute Rydberg ensemble, *Phys. Rev. Lett.* **111**, 113901 (2013). [Pages 2, 6, 50, 55, 57, 63, 73, 75, 87, 88, 90, 122, and 123]
- [33] Gounand, F., Hugon, M., Fournier, P., and Berlande, J., Superradiant cascading effects in rubidium Rydberg levels, *Journal of Physics B: Atomic and Molecular Physics* **12**, 547 (1979). [Pages 2, 6, and 67]
- [34] Baluktsian, M. Superradiance of Rydberg atoms in thermal vapour cells. Master’s thesis, University of Stuttgart, 2014. [Pages 2 and 6]

- [35] Vitrant, G., Raimond, J., Gross, M., and Haroche, S., Rydberg to plasma evolution in a dense gas of very excited atoms, *J. Phys. B* **15**, L49 (1982). [Pages 3, 6, 37, 38, 68, 71, 89, 126, and 131]
- [36] Kölle, A., Epple, G., Kübler, H., Löw, R., and Pfau, T., Four-wave mixing involving Rydberg states in thermal vapor, *Physical Review A* **85**, 063821 (2012). [Pages 3 and 6]
- [37] Mohapatra, A., Jackson, T., and Adams, C., Coherent optical detection of highly excited Rydberg states using electromagnetically induced transparency, *Phys. Rev. Lett.* **98**, 113003 (2007). [Pages 3, 57, 58, and 68]
- [38] Barredo, D., Kübler, H., Daschner, R., Löw, R., and Pfau, T., Electrical read-out for coherent phenomena involving Rydberg atoms in thermal vapor cells, *Phys. Rev. Lett.* **110**, 123002 (2013). [Pages 3, 6, 68, and 110]
- [39] Schmidt, J., Fiedler, M., Albrecht, R., Djekic, D., Schalberger, P., Baur, H., Löw, R., Fruehauf, N., Pfau, T., Anders, J., et al., Proof of concept for an optogalvanic gas sensor for NO based on Rydberg excitations, *Applied Physics Letters* **113**, 011113 (2018). [Pages 3 and 6]
- [40] Schmidt, J., Fiedler, M., Albrecht, R., Djekic, D., Schalberger, P., Baur, H., Löw, R., Fruehauf, N., Pfau, T., Anders, J., et al., An optogalvanic gas sensor for nitric oxide based on Rydberg excitations, *Atomic Physics* (2018). [Pages 3 and 6]
- [41] Scully, M.O. and Zubairy, M.S., Quantum Optics, *Cambridge Press, London* (1997). [Page 11]
- [42] Cohen-Tannoudji, C., Dupont-Roc, J., and Grynberg, G., Atom-photon interactions: basic processes and applications, *Atom-Photon Interactions: Basic Processes and Applications*, by Claude Cohen-Tannoudji, Jacques Dupont-Roc, Gilbert Grynberg, pp. 678. ISBN 0-471-29336-9. Wiley-VCH, March 1998., 678 (1998).
- [43] Mandel, L. and Wolf, E., *Optical coherence and quantum optics*, Cambridge university press.
- [44] Loudon, R., *The quantum theory of light*, OUP Oxford. [Pages 11 and 17]
- [45] Schrödinger, E., An undulatory theory of the mechanics of atoms and molecules, *Physical review* **28**, 1049 (1926). [Page 13]
- [46] Sobelman, I.I., *Atomic spectra and radiative transitions*, volume 12, Springer Science & Business Media. [Page 16]

-
- [47] Šibalić, N., Pritchard, J.D., Adams, C.S., and Weatherill, K.J., ARC: An open-source library for calculating properties of alkali Rydberg atoms, *Computer Physics Communications* **220**, 319–331 (2017). [Pages 17, 31, 32, 66, and 117]
- [48] Dupont-Roc, J., Cohen-Tannoudji, C., and Grynberg, G., Atom-Photon Interactions, *Basic Processes and Appli* (1992). [Page 19]
- [49] Siddons, P., Light propagation through atomic vapours, *J. Phys. B* **47**, 093001 (2014). [Pages 21 and 98]
- [50] Fleischhauer, M., Imamoglu, A., and Marangos, J.P., Electromagnetically induced transparency: Optics in coherent media, *Reviews of modern physics* **77**, 633 (2005). [Pages 24, 70, and 82]
- [51] Sedlacek, J.A., Schwettmann, A., Kübler, H., Löw, R., Pfau, T., and Shaffer, J.P., Microwave electrometry with Rydberg atoms in a vapour cell using bright atomic resonances, *Nature Physics* **8**, 819 (2012). [Pages 24 and 33]
- [52] Autler, S.H. and Townes, C.H., Stark effect in rapidly varying fields, *Physical Review* **100**, 703 (1955). [Page 24]
- [53] Raimond, J., Vitrant, G., and Haroche, S., Spectral line broadening due to the interaction between very excited atoms: 'the dense Rydberg gas', *Journal of Physics B: Atomic and Molecular Physics* **14**, L655 (1981). [Pages 25 and 37]
- [54] Mourachko, I., Comparat, D., De Tomasi, F., Fioretti, A., Nosbaum, P., Akulin, V., and Pillet, P., Many-body effects in a frozen Rydberg gas, *Phys. Rev. Lett.* **80**, 253 (1998).
- [55] Huber, B., Baluktsian, T., Schlagmüller, M., Kölle, A., Kübler, H., Löw, R., and Pfau, T., GHz Rabi flopping to Rydberg states in hot atomic vapor cells, *Phys. Rev. Lett.* **107**, 243001 (2011). [Page 25]
- [56] Whiting, E.E., An empirical approximation to the Voigt profile, *Journal of Quantitative Spectroscopy and Radiative Transfer* **8**, 1379–1384 (1968). [Page 26]
- [57] Javan, A., Kocharovskaya, O., Lee, H., and Scully, M.O., Narrowing of electromagnetically induced transparency resonance in a Doppler-broadened medium, *Phys. Rev. A* **66**, 013805 (2002). [Page 26]
- [58] Ryabtsev, I., Beterov, I., Tretyakov, D., Entin, V., and Yakshina, E., Doppler- and recoil-free laser excitation of Rydberg states via three-photon transitions, *Phys. Rev. A* **84**, 053409 (2011). [Page 26]

- [59] Salomaa, R. and Stenholm, S., Two-photon spectroscopy. II. Effects of residual Doppler broadening, *Journal of Physics B: Atomic and Molecular Physics* **9**, 1221 (1976). [Page 26]
- [60] Urvoy, A., Carr, C., Ritter, R., Adams, C., Weatherill, K., and Löw, R., Optical coherences and wavelength mismatch in ladder systems, *J. Phys. B* **46**, 245001 (2013). [Pages 26, 58, 60, and 82]
- [61] Sagle, J., Namiotka, R., and Huennekens, J., Measurement and modelling of intensity dependent absorption and transit relaxation on the cesium line, *Journal of Physics B: Atomic, Molecular and Optical Physics* **29**, 2629 (1996). [Page 27]
- [62] Frey, M., Ling, X., Lindsay, B., Smith, K., and Dunning, F., Use of the Stark effect to minimize residual electric fields in an experimental volume, *Review of scientific instruments* **64**, 3649–3650 (1993). [Page 29]
- [63] Schramm, A., Weber, J., Kreil, J., Klar, D., Ruf, M.W., and Hotop, H., Laser Photoelectron Attachment to Molecules in a Skimmed Supersonic Beam: Diagnostics of Weak Electric Fields and Attachment Cross Sections Down to 20 μ eV, *Phys. Rev. Lett.* **81**, 778 (1998).
- [64] Osterwalder, A. and Merkt, F., Using high Rydberg states as electric field sensors, *Phys. Rev. Lett.* **82**, 1831 (1999). [Page 29]
- [65] Rydberg, J., XXXIV. On the structure of the line-spectra of the chemical elements, *The London, Edinburgh, and Dublin Philosophical Magazine and Journal of Science* **29**, 331–337 (1890). [Page 29]
- [66] Balmer, J., Notiz ueber die Spektrallinien des Wasserstoffs, *Annalen der Physik.* [Page 29]
- [67] Gallagher, T.F., *Rydberg atoms*, volume 51 of *Cambridge Monographs on Atomic, Molecular and Chemical Physics*, Cambridge University Press (1999). [Pages 30, 40, and 68]
- [68] Weber, K.H. and Sansonetti, C.J., Accurate energies of nS, nP, nD, nF, and nG levels of neutral cesium, *Phys. Rev. A* **35**, 4650 (1987). [Page 30]
- [69] Lorenzen, C.J. and Niemax, K., Precise quantum defects of nS, nP and nD Levels in Cs I, *Zeitschrift für Physik A Atoms and Nuclei* **315**, 127–133 (1984).
- [70] Li, W., Mourachko, I., Noel, M., and Gallagher, T., Millimeter-wave spectroscopy of cold Rb Rydberg atoms in a magneto-optical trap: Quantum defects of the ns, np, and nd series, *Phys. Rev. A* **67**, 052502 (2003). [Page 30]

-
- [71] Gallagher, T., Rydberg atoms, *Reports on Progress in Physics* **51**, 143 (1988). [Page 31]
- [72] Zeeman, P., *Ueber einen Einfluss der Magnetisirung auf die Natur des von einer Substanz emittirten Lichtes*. [Page 31]
- [73] Jenkins, F. and Segre, E., The quadratic Zeeman effect, *Physical Review* **55**, 52 (1939). [Page 31]
- [74] Stark, J., Beobachtungen über den Effekt des elektrischen Feldes auf Spektrallinien. I. Quereffekt, *Annalen der Physik* **348**, 965–982 (1914). [Page 31]
- [75] Gaebasso, A., Sopra il fenomeno di stark-lo surdo, *Il Nuovo Cimento (1911-1923)* **7**, 338–343 (1914). [Page 31]
- [76] Hunter, L., Krause Jr, D., Miller, K., Berkeland, D., and Boshier, M., Precise measurement of the Stark shift of the cesium D1 line, *Optics communications* **94**, 210–214 (1992). [Page 31]
- [77] Schmieder, R.W., Lurio, A., and Happer, W., Quadratic Stark Effect in the P 3 2 2 States of the Alkali Atoms, *Phys. Rev. A* **3**, 1209 (1971). [Page 32]
- [78] Khadjavi, A., Lurio, A., and Happer, W., Stark effect in the excited states of Rb, Cs, Cd, and Hg, *Physical Review* **167**, 128 (1968). [Page 32]
- [79] O’sullivan, M. and Stoicheff, B., Scalar polarizabilities and avoided crossings of high Rydberg states in Rb, *Phys. Rev. A* **31**, 2718 (1985). [Page 32]
- [80] Weber, S., Tresp, C., Menke, H., Urvoy, A., Firstenberg, O., Büchler, H.P., and Hofferberth, S., Calculation of Rydberg interaction potentials, *J. Phys. B* **50**, 133001 (2017). [Pages 32 and 33]
- [81] Margenau, H., Van der Waals forces, *Reviews of Modern Physics* **11**, 1 (1939). [Page 33]
- [82] Haroche, S. and Raimond, J. Radiative properties of Rydberg states in resonant cavities. in *Advances in atomic and molecular physics*, volume 20, pages 347–411. Elsevier, 1985.
- [83] Robinson, M.P., Laburthe Tolra, B., Noel, M.W., Gallagher, T.F., and Pillet, P., Spontaneous evolution of Rydberg atoms into an ultracold plasma, *Phys. Rev. Lett.* **85**, 4466 (2000). [Pages 33 and 89]
- [84] Born, M. and Oppenheimer, R., Zur quantentheorie der molekeln, *Annalen der physik* **389**, 457–484 (1927). [Page 33]

- [85] Le Roy, R.J., Long-Range Potential Coefficients From RKR Turning Points: C 6 and C 8 for B (3Π_{0u}⁺)-State Cl₂, Br₂, and I₂, *Canadian Journal of Physics* **52**, 246–256 (1974). [Page 34]
- [86] Flannery, M., Vranceanu, D., and Ostrovsky, V., Long-range interaction between polar Rydberg atoms, *Journal of Physics B: Atomic, Molecular and Optical Physics* **38**, S279 (2005). [Page 35]
- [87] Reinhard, A., Liebisch, T.C., Knuffman, B., and Raithel, G., Level shifts of rubidium Rydberg states due to binary interactions, *Phys. Rev. A* **75**, 032712 (2007). [Pages 35 and 37]
- [88] Comparat, D. and Pillet, P., Dipole blockade in a cold Rydberg atomic sample, *JOSA B* **27**, A208–A232 (2010). [Page 35]
- [89] Berendsen, H., Grigera, J., and Straatsma, T., The missing term in effective pair potentials, *Journal of Physical Chemistry* **91**, 6269–6271 (1987). [Page 37]
- [90] Förster, T., Zwischenmolekulare energiewanderung und fluoreszenz, *Annalen der physik* **437**, 55–75 (1948). [Page 37]
- [91] Singer, K., Stanojevic, J., Weidemüller, M., and Côté, R., Long-range interactions between alkali Rydberg atom pairs correlated to the ns–ns, np–np and nd–nd asymptotes, *J. Phys. B* **38**, S295 (2005). [Pages 37, 72, and 73]
- [92] Butt, H.J., Kappl, M., et al., *Surface and interfacial forces*, Wiley Online Library. [Page 37]
- [93] Vogt, T., Viteau, M., Chotia, A., Zhao, J., Comparat, D., and Pillet, P., Electric-field induced dipole blockade with Rydberg atoms, *Phys. Rev. Lett.* **99**, 073002 (2007). [Page 37]
- [94] Ryabtsev, I., Tretyakov, D., Beterov, I., Bezuglov, N., Miculis, K., and Ekers, A., Collisional and thermal ionization of sodium Rydberg atoms: I. Experiment for nS and nD atoms with n= 8–20, *Journal of Physics B: Atomic, Molecular and Optical Physics* **38**, S17 (2005). [Page 38]
- [95] Miculis, K., Beterov, I., Bezuglov, N., Ryabtsev, I., Tretyakov, D., Ekers, A., and Klucharev, A., Collisional and thermal ionization of sodium Rydberg atoms: II. Theory for nS, nP and nD states with n= 5–25, *Journal of Physics B: Atomic, Molecular and Optical Physics* **38**, 1811 (2005).
- [96] Beterov, I., Tretyakov, D., Ryabtsev, I., Bezuglov, N., Miculis, K., Ekers, A., and Klucharev, A., Collisional and thermal ionization of sodium Rydberg atoms III. Experiment and theory for nS and nD states with n= 8–20 in crossed atomic beams,

-
- Journal of Physics B: Atomic, Molecular and Optical Physics* **38**, 4349 (2005). [Page 38]
- [97] Beigman, I.L. and Lebedev, V.S., Collision theory of Rydberg atoms with neutral and charged particles, *Physics Reports* **250**, 95–328 (1995). [Page 38]
- [98] Olson, R., Ion-Rydberg atom collision cross sections, *Journal of Physics B: Atomic and Molecular Physics* **13**, 483 (1980). [Page 38]
- [99] Foltz, G., Beiting, E., Jeys, T., Smith, K., Dunning, F., and Stebbings, R., State changing in Na (nd)-electron collisions, *Phys. Rev. A* **25**, 187 (1982). [Page 38]
- [100] MacAdam, K., Martin, N., Smith, D., Rolfes, R., and Richards, D., Electron loss from Na Rydberg atoms by ion impact, *Phys. Rev. A* **34**, 4661 (1986). [Page 38]
- [101] Nagesha, K. and MacAdam, K.B., Electron impact ionization of sodium Rydberg atoms below 2 eV, *Phys. Rev. Lett.* **91**, 113202 (2003). [Pages 38 and 126]
- [102] Vranceanu, D., Electron impact ionization of Rydberg atoms, *Phys. Rev. A* **72**, 022722 (2005). [Pages 39 and 113]
- [103] Glukhov, I., Nekipelov, E., and Ovsiannikov, V., Blackbody-induced decay, excitation and ionization rates for Rydberg states in hydrogen and helium atoms, *Journal of Physics B: Atomic, Molecular and Optical Physics* **43**, 125002 (2010). [Page 39]
- [104] Ovsiannikov, V., Glukhov, I., and Nekipelov, E., Radiative lifetime and photoionization cross-section for Rydberg states in alkali-metal atoms, *Optics and Spectroscopy* **111**, 25 (2011). [Page 39]
- [105] Deng, Z. and Eberly, J.H., Multiphoton absorption above ionization threshold by atoms in strong laser fields, *JOSA B* **2**, 486–493 (1985). [Page 39]
- [106] Beterov, I., Tretyakov, D., Ryabtsev, I., Entin, V., Ekers, A., and Bezuglov, N., Ionization of Rydberg atoms by blackbody radiation, *New Journal of Physics* **11**, 013052 (2009). [Page 40]
- [107] Pohl, T., Pattard, T., and Rost, J.M., Plasma formation from ultracold Rydberg gases, *Phys. Rev. A* **68**, 010703 (2003). [Page 40]
- [108] Ludlow, A.D., Boyd, M.M., Ye, J., Peik, E., and Schmidt, P.O., Optical atomic clocks, *Reviews of Modern Physics* **87**, 637 (2015). [Page 40]
- [109] Biondi, M.A., Studies of the mechanism of electron-ion recombination. I, *Physical Review* **129**, 1181 (1963). [Page 40]
- [110] Rogers, W.A. and Biondi, M.A., Studies of the mechanism of electron-ion recombination. II, *Physical Review* **134**, A1215 (1964). [Page 40]

- [111] Schwartz, S.J., Owen, C.J., and Burgess, D., Astrophysical plasmas, *Astronomy Unit, Queen Mary), University of London, UK* (2004). [Page 41]
- [112] Chen, F.F., *Introduction to plasma physics and controlled fusion*, volume 1, Springer.
- [113] Fitzpatrick, R., *Plasma physics: an introduction*, Crc Press.
- [114] Stroth, U., *Plasmaphysik, Auflage. Vieweg+ Teubner* (2011).
- [115] Kaufmann, M., *Plasmaphysik und Fusionsforschung*, Springer. [Page 41]
- [116] Saha, M.N., LIII. Ionization in the solar chromosphere, *The London, Edinburgh, and Dublin Philosophical Magazine and Journal of Science* **40**, 472–488 (1920). [Page 41]
- [117] Eriksson, K. and Pettersson, J., New measurements in the spectrum of the neutral nitrogen atom, *Physica Scripta* **3**, 211 (1971). [Page 41]
- [118] Lloyd, S., Computational capacity of the universe, *Phys. Rev. Lett.* **88**, 237901 (2002). [Page 41]
- [119] Debye, P. and Hückel, E., Zur Theorie der Elektrolyte I Physik, *Z* **24**, 185–206 (1923). [Pages 42 and 43]
- [120] Rayfield, G., Rayfield, GWF Reif, and F. Reif, 1965, Phys. Rev. 136, 1194, *Phys. Rev.* **136**, 1194 (1965). [Page 42]
- [121] Taylor, B., *Methodus incrementorum directa & inversa. Auctore Brook Taylor, LL. D. & Regiae Societatis Secretario*, typis Pearsonianis: prostant apud Gul. Innys ad Insignia Principis in [Page 42]
- [122] Salpeter, E., Electron screening and thermonuclear reactions, *Australian Journal of Physics* **7**, 373–388 (1954). [Page 44]
- [123] Salpeter, E. and Van Horn, H., Nuclear reaction rates at high densities, *The Astrophysical Journal* **155**, 183 (1969). [Page 44]
- [124] Landau, L.D. and Lifshitz, E.M., *Course of theoretical physics*, Elsevier. [Page 45]
- [125] Mozer, B. and Baranger, M., Electric field distributions in an ionized gas. II, *Physical Review* **118**, 626 (1960). [Page 46]
- [126] Hooper Jr, C., Electric microfield distributions in plasmas, *Physical Review* **149**, 77 (1966).
- [127] Potekhin, A.Y., Chabrier, G., and Gilles, D., Electric microfield distributions in electron-ion plasmas, *Physical Review E* **65**, 036412 (2002).

-
- [128] Stambulchik, E. and Maron, Y., Plasma line broadening and computer simulations: A mini-review, *High Energy Density Physics* **6**, 9–14 (2010). [Pages 46 and 90]
- [129] Holtsmark, J., Über die verbreiterung von spektrallinien, *Ann. Phys.* **363**, 577–630 (1919). [Page 46]
- [130] Hummer, D., Rational approximations for the holtsmark distribution, its cumulative and derivative, *J. Quant. Spec. Rad. Trans.* **36**, 1–5 (1986). [Page 47]
- [131] Gibbs Hyatt, M., *Optical Bistability: Controlling Light with Light*, Academic Press. [Page 49]
- [132] Letscher, F., Thomas, O., Niederprüm, T., Fleischhauer, M., and Ott, H., Bistability versus metastability in driven dissipative Rydberg gases, *Physical Review X* **7**, 021020 (2017). [Page 49]
- [133] Gibbs, H., McCall, S., and Venkatesan, T., Differential gain and bistability using a sodium-filled Fabry-Perot interferometer, *Phys. Rev. Lett.* **36**, 1135 (1976). [Page 50]
- [134] Gibbs, H., McCall, S., Venkatesan, T., Gossard, A., Passner, A., and Wiegmann, W., Optical bistability in semiconductors, *Applied Physics Letters* **35**, 451–453 (1979). [Page 50]
- [135] Stegeman, G., Assanto, G., Zanoni, R., Seaton, C., Garmire, E., Maradudin, A., Reinisch, R., and Vitrant, G., Bistability and switching in nonlinear prism coupling, *Applied physics letters* **52**, 869–871 (1988). [Page 50]
- [136] Wang, F., Li, G., Tam, H., Cheah, K., and Zhu, S., Optical bistability and multistability in one-dimensional periodic metal-dielectric photonic crystal, *Applied Physics Letters* **92**, 211109 (2008). [Page 50]
- [137] Hehlen, M., Güdel, H., Shu, Q., Rai, J., Rai, S., and Rand, S., Cooperative bistability in dense, excited atomic systems, *Phys. Rev. Lett.* **73**, 1103 (1994). [Page 50]
- [138] Ding, D., Adams, C., Shi, B., and Guo, G., Non-equilibrium phase-transitions in multi-component Rydberg gases, *arXiv preprint arXiv:1606.08791v1* (2016). [Pages 50, 58, 75, 129, and 137]
- [139] de Melo, N.R., Wade, C.G., Šibalić, N., Kondo, J.M., Adams, C.S., and Weatherill, K.J., Intrinsic optical bistability in a strongly driven Rydberg ensemble, *Phys. Rev. A* **93**, 063863 (2016). [Pages 50, 73, 75, 87, and 99]
- [140] Bowden, C. and Sung, C., First-and second-order phase transitions in the Dicke model: Relation to optical bistability, *Phys. Rev. A* **19**, 2392 (1979). [Page 50]

- [141] Guillot-Noël, O., Goldner, P., and Gourier, D., Dynamics of intrinsic optical bistability in two weakly interacting quantum systems, *Phys. Rev. A* **66**, 063813 (2002). [Page 50]
- [142] Carr, C. *Cooperative non-equilibrium dynamics in a thermal rydberg ensemble*. PhD thesis. [Pages 50 and 90]
- [143] Lee, T.E., Haeffner, H., and Cross, M., Collective quantum jumps of Rydberg atoms, *Phys. Rev. Lett.* **108**, 023602 (2012). [Page 50]
- [144] Qian, J., Zhou, L., and Zhang, W., Quantum phases of strongly interacting Rydberg atoms in triangular lattices, *Phys. Rev. A* **87**, 063421 (2013). [Page 50]
- [145] Šibalić, N., Wade, C.G., Adams, C.S., Weatherill, K.J., and Pohl, T., Driven-dissipative many-body systems with mixed power-law interactions: Bistabilities and temperature-driven nonequilibrium phase transitions, *Phys. Rev. A* **94**, 011401 (2016). [Page 51]
- [146] Weller, D., Urvoy, A., Rico, A., Löw, R., and Kübler, H., Charge-induced optical bistability in thermal Rydberg vapor, *Phys. Rev. A* **94**, 063820 (2016). [Pages 55 and 129]
- [147] Urvoy, A. *Large bandwidth excitation of Rydberg atoms in thermal vapor: Fast dynamics and strong interaction effects*. PhD thesis. [Pages 55 and 61]
- [148] Siddons, P., Adams, C.S., Ge, C., and Hughes, I.G., Absolute absorption on rubidium D lines: comparison between theory and experiment, *Journal of Physics B: Atomic, Molecular and Optical Physics* **41**, 155004 (2008). [Pages 57 and 81]
- [149] Thoumany, P., Hänsch, T., Stania, G., Urbonas, L., and Becker, T., Optical spectroscopy of rubidium Rydberg atoms with a 297 nm frequency-doubled dye laser, *Opt. Lett.* **34**, 1621–1623 (2009). [Page 58]
- [150] Shepherd, S., Fulton, D.J., and Dunn, M.H., Wavelength dependence of coherently induced transparency in a Doppler-broadened cascade medium, *Phys. Rev. A* **54**, 5394–5399 (1996). [Page 58]
- [151] Ding, D., Busche, H., Shi, B., Guo, G., and Adams, C., Phase diagram of non-equilibrium phase transition in a strongly-interacting Rydberg atom vapour, *arXiv preprint arXiv:1606.08791v2*, 93 (2019). [Page 58]
- [152] Schwettmann, A., Crawford, J., Overstreet, K.R., and Shaffer, J.P., Cold cs Rydberg-gas interactions, *Phys. Rev. A* **74**, 020701 (2006). [Page 66]
- [153] Chandrasekhar, S., Stochastic problems in physics and astronomy, *Reviews of modern physics* **15**, 1 (1943). [Page 67]

- [154] Goldschmidt, E.A., Boulier, T., Brown, R.C., Koller, S.B., Young, J.T., Gorshkov, A.V., Rolston, S.L., and Porto, J.V., Anomalous Broadening in Driven Dissipative Rydberg Systems, *Phys. Rev. Lett.* **116**, 113001 (2016). [Page 67]
- [155] Hagen, N., Kupinski, M., and Dereniak, E.L., Gaussian profile estimation in one dimension, *Applied optics* **46**, 5374–5383 (2007). [Page 70]
- [156] Demtröder, W., *Linienbreiten und Profile von Spektrallinien*, pages 43–68, Springer Berlin Heidelberg, Berlin, Heidelberg. [Page 71]
- [157] Weller, D., Shaffer, J.P., Pfau, T., Löw, R., and Kübler, H., Interplay between thermal Rydberg gases and plasmas, *Phys. Rev. A* **99**, 043418 (2019). [Page 79]
- [158] Corwin, K.L., Lu, Z.T., Hand, C.F., Epstein, R.J., and Wieman, C.E., Frequency-stabilized diode laser with the Zeeman shift in an atomic vapor, *Applied Optics* **37**, 3295–3298 (1998). [Page 82]
- [159] Fritschel, P., Jeffries, A., and Kane, T.J., Frequency fluctuations of a diode-pumped Nd: YAG ring laser, *Opt. Lett.* **14**, 993–995 (1989). [Page 82]
- [160] Šibalić, N., Wade, C.G., Adams, C.S., Weatherill, K.J., and Pohl, T., Driven-dissipative many-body systems with mixed power-law interactions: Bistabilities and temperature-driven nonequilibrium phase transitions, *Phys. Rev. A* **94**, 011401 (2016). [Page 87]
- [161] Bowden, P.R., It’s all about energy, *Physics World* **29**, 64 (2016). [Pages 87 and 88]
- [162] Killian, T.C., Kulin, S., Bergeson, S.D., Orozco, L.A., Orzel, C., and Rolston, S.L., Creation of an ultracold neutral plasma, *Phys. Rev. Lett.* **83**, 4776 (1999). [Page 89]
- [163] Lin, C., Gocke, C., Röpke, G., and Reinholz, H., Transition rates for a Rydberg atom surrounded by a plasma, *Phys. Rev. A* **93**, 042711 (2016). [Pages 90 and 115]
- [164] Agnew, L. and Reichelt, W., Identification of the ionic species in a cesium plasma diode, *Journal of Applied Physics* **39**, 3149–3155 (1968). [Page 90]
- [165] Wade, C.G. *Terahertz Wave Detection and Imaging with a Hot Rydberg Vapour*. PhD thesis. [Pages 90, 91, and 122]
- [166] Kim, J.H., Seong, D.J., Lim, J.Y., and Chung, K.H., Plasma frequency measurements for absolute plasma density by means of wave cutoff method, *Applied physics letters* **83**, 4725–4727 (2003). [Page 91]
- [167] Schunk, R. and Nagy, A., *Ionospheres: physics, plasma physics, and chemistry*, Cambridge university press. [Page 94]

- [168] Maxwell, J.C., V. Illustrations of the dynamical theory of gases.—Part I. On the motions and collisions of perfectly elastic spheres, *The London, Edinburgh, and Dublin Philosophical Magazine and Journal of Science* **19**, 19–32 (1860). [Page 111]
- [169] Schmieder, R.W., Lurio, A., Happer, W., and Khadjavi, A., Level-Crossing Measurement of Lifetime and hfs Constants of the P 3 2 2 States of the Stable Alkali Atoms, *Phys. Rev. A* **2**, 1216 (1970). [Page 112]
- [170] Bonifacio, R. and Meystre, P., Critical slowing down in optical bistability, *Optics Communications* **29**, 131–134 (1979). [Page 122]
- [171] Scheffer, M., Bascompte, J., Brock, W.A., Brovkin, V., Carpenter, S.R., Dakos, V., Held, H., Van Nes, E.H., Rietkerk, M., and Sugihara, G., Early-warning signals for critical transitions, *Nature* **461**, 53 (2009). [Page 122]
- [172] Marcuzzi, M., Levi, E., Diehl, S., Garrahan, J.P., and Lesanovsky, I., Universal nonequilibrium properties of dissipative Rydberg gases, *Phys. Rev. Lett.* **113**, 210401 (2014). [Page 122]
- [173] Grynberg, G. and Cribier, S., Critical exponents in dispersive optical bistability, *Journal de Physique Lettres* **44**, 449–453 (1983). [Page 122]
- [174] Hohenberg, P.C. and Halperin, B.I., Theory of dynamic critical phenomena, *Reviews of Modern Physics* **49**, 435 (1977). [Page 122]
- [175] Levenberg, K., A method for the solution of certain non-linear problems in least squares, *Q. Appl. Math.* **2**, 164–168 (1944). [Page 124]
- [176] Marquardt, D.W., An algorithm for least-squares estimation of nonlinear parameters, *J. Soc. Ind. App. Math.* **11**, 431–441 (1963). [Page 124]
- [177] Kumar, S., Fan, H., Kübler, H., Sheng, J., and Shaffer, J.P., Atom-based sensing of weak radio frequency electric fields using homodyne readout, *Scientific reports* **7**, 42981 (2017). [Page 126]
- [178] Saßmannshausen, H., Merkt, F., and Deiglmayr, J., High-resolution spectroscopy of Rydberg states in an ultracold cesium gas, *Physical Review A* **87**, 032519 (2013). [Page 132]
- [179] Bounds, A., Jackson, N., Hanley, R., Bridge, E., Huillery, P., and Jones, M., Coulomb anti-blockade in a Rydberg dressed gas, *arXiv preprint arXiv:1901.05391* (2019). [Page 137]
- [180] Bhowmick, A., Sahoo, S.S., and Mohapatra, A.K., Optical nonlinearity of rydberg electromagnetically induced transparency in thermal vapor using the optical-heterodyne-detection technique, *Physical Review A* **94**, 023839 (2016). [Page 137]

- [181] Wade, C.G., Šibalić, N., de Melo, N.R., Kondo, J.M., Adams, C.S., and Weatherill, K.J., Real-time near-field terahertz imaging with atomic optical fluorescence, *Nature Photonics* **11**, 40 (2017).
- [182] Kara, D., Bhowmick, A., and Mohapatra, A.K., Rydberg interaction induced enhanced excitation in thermal atomic vapor, *Scientific reports* **8**, 5256 (2018).
- [183] Bhowmick, A., Kara, D., and Mohapatra, A.K., Study of Rydberg blockade in thermal vapor, *arXiv preprint arXiv:1802.06599* (2018).
- [184] Downes, L.A., MacKellar, A.R., Whiting, D.J., Bourgenot, C., Adams, C.S., and Weatherill, K.J., Ultra-high-speed Terahertz Imaging Using Atomic Vapour, *arXiv preprint arXiv:1903.01308* (2019). [Page 137]
- [185] Han, J., Vogt, T., Gross, C., Jaksch, D., Kiffner, M., and Li, W., Coherent microwave-to-optical conversion via six-wave mixing in Rydberg atoms, *Physical review letters* **120**, 093201 (2018). [Page 138]
- [186] Fantz, U., Basics of plasma spectroscopy, *Plasma sources science and technology* **15**, S137 (2006). [Page 138]